Coupled thermo-hydro-chemical-mechanical models for the bentonite barrier in a radioactive waste repository

Author: Alba Mon López

Doctoral Thesis UDC 2017

Advisor: Francisco Javier Samper Calvete

Civil Engineering Ph.D. Program

Civil Engineering School

UNIVERSIDADE DA CORUÑA

Modelos acoplados termo-hidro-químico-mecánicos de la barrera de bentonita de un almacenamiento de residuos radiactivos

Autora: Alba Mon López

Tesis Doctoral UDC 2017

Director: Francisco Javier Samper Calvete

Programa de doctorado de Ingeniería Civil

E.T.S. Ingenieros de Caminos, Canales y Puertos

UNIVERSIDADE DA CORUÑA

Dr. Francisco Javier Samper Calvete, Ph.D. from University of Arizona (USA) and the Polytechnical University of Madrid (Spain), Full Professor, certifies that this doctoral thesis, entitled **Coupled thermo-hydro-chemical-mechanical models for the bentonite barrier in a radioactive waste repository**, has been performed by Alba Mon López under his supervision in order to obtain the Doctor of Philosophy degree with the International Mention by the University of A Coruña

Dr. Francisco Javier Samper Calvete, Doctor por la Universidad de Arizona (EEUU) y por la Universidad Politécnica de Madrid (España), Catedrático de Universidad, certifica que la tesis doctoral con título, ***Coupled thermo-hydro-chemical-mechanical models for the bentonite barrier in a radioactive waste repository****, ha sido desarrollada por Alba Mon López bajo su supervisión para obtener el grado de Doctor y con Mención Internacional por la Universidad de A Coruña.*

A Coruña, April 2017

A Coruña, Abril 2017

Alba Mon López	Dr. F. Javier Samper Calvete
PhD. Student	Advisor
Doctorando	*Director*

Acknowledgements

I would like to thank Professor Javier Samper for the opportunity to join his research group and performing this dissertation under his supervision. It would have been impossible to complete this dissertation without his inspiration, encouragement, patience and support throughout my graduate research.

Most of the research presented in this dissertation has been performed within the framework of the PEBS Project funded by the European Atomic Energy Community's Seventh Framework Programme (FP7/2007-2011) under grant agreement #232598; the CEBAMA Project funded by the European Atomic Energy Community's (Euratom) Horizon 2020 Programme (NFRP-2014/2015) under grant agreement #662147; and the FEBEX-DP Project (Grimsel Phase VI) funded by the FEBEX-DP Consortium. This work has been also supported by ENRESA (Spain), the Spanish Ministry of Economy and Competitiveness (Projects CGL2012-36560 and CGL2016-78281), FEDER funds and the Galician Regional Government (Project 10MDS118028PR and Fund 2012/181 from “Consolidación e estruturación de unidades de investigación competitivas”, Grupos de referencia competitiva). I have also enjoyed a research pre-doctoral contract from the University of A Coruña.

I would like to recognize Peter Eriksson from SKB (Sweden) and Georg Kosakowski from PSI (Switzerland) who gave me the opportunity to spend 1 and 3 months, respectively, and brought me the chance to enjoy their research institutions and had very enriching experiences. The stay at SKB was funded by a training scholarship from the LUCOEX project. The research stay at PSI was funded by an INDITEX-UDC scholarship.

The models that I performed in my dissertation have relied on measured data from the FEEBX *in situ* test and the experiments carried out by CIEMAT and UAM. I would like to thank Pedro Luis Martín, Mariví Villar, Ana María Fernández, María Jesús Turrero and Elena Torres from CIEMAT and Jaime Cuevas from UAM for providing these data.

I would like to thank also all my colleagues of the research group *Agua y Suelo,* especially to Luis Montenegro who encouraged and supported me during my research work, Bruno Pisani, Jesús Fernández, Acacia Naves and Yanmei Li.

Finally, I would like to dedicate this dissertation to my friends, to my parents and to my husband, Abel, without his confidence and support it would not have been possible to achieve it.

Agradecimientos

Me gustaría agradecer a Javier Samper la oportunidad de trabajar en su grupo de investigación y poder realizar la tesis doctoral bajo su supervisión. Habría sido imposible realizarla sin su inspiración, paciencia y apoyo durante la etapa de realización de la tesis.

La mayor parte de este trabajo ha sido desarrollado dentro del marco de proyecto europeo PEBS Project financiado por el “European Atomic Energy Community's Seventh Framework Programme” (FP7/2007-2011) bajo el contrato Nº 232598; el proyecto CEBAMA financiado por “European Atomic Energy Community's (Euratom) Horizon 2020 Programme (NFRP-2014/2015)” bajo el contrato Nº 662147; y el proyecto FEBEX-DP (Grimsel Fase VI) financiado por el Consorcio del Proyecto FEBEX-DP. Este trabajo también ha sido apoyado por ENRESA (España), Ministerio de Economía y Competencia (Proyecto CGL2012-36560 y CGL2016-78281), fondeos FEDER y fondos de la Xunta de Galicia (Proyecto 10MDS118028PR y fondos: 2012/181 de “Consolidación e estructuración de unidades de investigación competitivas”, Grupos de referencia competitiva). También he disfrutado de una un contrato pre-doctoral financiado por la Universidad de A Coruña.

Me gustaría agradecerle a Peter Eriksson de SKB (Suecia) y a Georg Kosakowski de PSI (Suiza) la oportunidad de pasar 1 y 3 meses con ellos respectivamente, de participar en sus centros de investigación y llevarme experiencias enriquecedoras. La estancia en SKB fue financiada por una beca del Proyecto LUCOEX, y la estancia en PSI fue financiada por la beca INDITEX-UDC.

Los modelos llevados a cabo durante esta tesis han dependido de los datos medidos en el ensayo *in situ* del proyecto FEBEX y de experimentos de laboratorio de CIEMAT y UAM. Me gustaría agradecerles la aportación de los datos que he necesitado a Pedro Luis Martín, Mariví Villar, Ana María Fernández, María Jesús Turrero, Elena Torres de CIEMAT y a Jaime Cuevas de la UAM.

Me gustaría también agradecer la colaboración de mis compañeros del grupo de *Agua y Suelo*, especialmente a Luis Montenegro quien me ha alentado y apoyado durante el trabajo de investigación, Bruno Pisani, Jesús Fernández, Acacia Naves y Yanmei Li.

Finalmente, me gustaría dedicar la tesis a mis amigas, mi padres y a mi marido, Abel, sin su confianza y su apoyo esto no habría sido posible.

Coupled thermo-hydro-chemical-mechanical models for the bentonite barrier in a radioactive waste repository

Abstract

Compacted bentonite is foreseen in several countries as a backfill and sealing material for high-level radioactive waste (HLW) disposal. The long-term performance assessment and the evaluation of the safety of a HLW repository requires the use of numerical models dealing with the thermal (T), hydrodynamic (H), chemical (C) and mechanical (M) processes and their interplays. This dissertation presents coupled THCM models of the bentonite barrier of HLW repositories in clay and granite. The models account for the geochemical processes taking place within the bentonite as well as the interactions of the bentonite with the concrete liner and the corrosion products of the metallic canister. The THCM code INVERSE-FADES-CORE has been updated, extended to deal with reactive gaseous phases, verified and benchmarked against other codes. Coupled THCM numerical models have been applied to: 1) Small-scale heating and hydration laboratory tests performed by CIEMAT on compacted FEBEX (Full-scale Engineer Barrier Experiment) bentonite and its interactions with corrosion products and concrete; 2) FEBEX *mock-up* and *in situ* tests; 3) Long-term reactive transport model predictions of HLW repositories in granite and clay rocks. The results of the numerical models of the lab and in situ tests show a good agreement with the measured data.

.

Modelos acoplados termo-hidro-químico-mecánicos de la barrera de bentonita de un almacenamiento de residuos radiactivos

Resumen

La bentonita compactada es el material previsto para el relleno y sellado de los residuos radioactivos de alta actividad (RAA) en un almacenamiento geológico profundo (AGP). La evaluación del comportamiento y de la seguridad de un AGP requiere utilizar modelos numéricos acoplados térmicos (T), hidrodinámicos (H), químicos (Q) y mecánicos (M). En esta tesis se han desarrollado modelos acoplados THQM de la barrera de bentonita para el AGP en granito y en arcilla. Los modelos tienen en cuenta los procesos geoquímicos que tienen lugar en la bentonita y sus interacciones con el hormigón y con los productos de corrosión del contenedor metálico. Los modelos se han realizado con una versión del código THQM INVERSE-FADES-CORE que se ha mejorado para tener en cuenta el transporte reactivo de gases en la fase gaseosa y se ha verificado y comparado con otros códigos. Se han realizado modelos numéricos THQM de: 1) Ensayos de laboratorio; 2) Ensayos FEBEX (Full-scale Engineer Barrier Experiment) en *maqueta* e *in situ*; 3) Predicciones de la evolución geoquímica a largo plazo de la barrera de bentonita en un AGP en granito y en arcilla. Los resultados de los modelos numéricos muestran un buen ajuste a los datos medidos.

Modelos acoplados termo-hidro-químico-mecánicos da barreira de bentonita dun almacenamento de residuos radioactivos

Resumo

A bentonita compactada é o material previsto para o recheo e selado dos residuos radioactivos de alta actividade (RAA) nun almacenamento xeolóxico profundo (AXP). A avaliación do comportamento e da seguridade dun AXP precisa de modelos numéricos acoplados térmicos (T), hidrodinámicos (H), químicos (Q) e mecánicos (M). Nesta tese desenroláronse modelos acoplados THQM da barreira de bentonita para o AXP en granito e arxila. Os modelos teñen en conta os procesos xeoquímicos que teñen lugar na bentonita e a súas interaccións co formigón e cos produtos de corrosión do contenedor metálico. Os modelos fixéronse con unha versión do código THQM INVERSE-FADES-CORE que se mellorou para ter en conta o transporte reactivo de gases na fase gaseosa e que se verificou e comparou con outros códigos. Fixéronse modelos numéricos THQM de: 1) Ensaios de laboratorio de hidratación e quecemento de mostras de bentonita FEBEX (Full-scale Engineer Barrier Experiment) compactada e a súas interaccións con produtos de corrosión e formigón; 2) Ensaios FEBEX en *maqueta* e *in situ*; 3) Predicións da evolución xeoquímica a longo prazo da barreira de bentonita nun AXP en granito e arxila. Os resultados dos modelos numéricos amosan un bo axuste aos datos medidos.

Preface

The storage of high-level radioactive waste (HLW) in deep geological repositories (DGR) is based on a multibarrier concept, which includes natural and engineered barriers. The natural barrier is the host rock while the engineered barriers include the waste form, the canister, and the bentonite buffer. Significant research has been performed during the last decades to improve the knowledge, characterize the key parameters and constitutive equations and develop numerical models for the HLW repository barriers. FEBEX (Full-scale Engineered Barrier Experiment) is a demonstration and research project for the engineered bentonite barrier of a HLW repository. FEBEX is based on the Spanish reference concept for radioactive waste disposal in crystalline rock, which consists on the disposal of spent fuel in carbon steel canisters in long horizontal disposal drifts excavated in granite. The main physical, thermal, hydrodynamic, mechanical and geochemical properties of the bentonite were extensively studied during the project. This research has been tackled within the framework of projects funded by the EURATOM Program of the European Commission. Significant parts of this dissertation have been developed within the PEBS (Long-term Performance of Engineered Barrier Systems), CEBAMA (Cement-based materials, properties, evolution, barrier functions) and FEBEX-DP Projects (Full-scale Engineered Barrier Experiment Dismantling Project).

The main objective of this dissertation is the updating and the testing of coupled thermal, hydrodynamic, chemical and mechanical (THCM) models for the compacted bentonite barrier in a high-level radioactive waste repository including the following activities: 1) Updating and improving the conceptual and numerical THCM model ; 2) Improving the THCM code INVERSE-FADES-CORE; 3) Modeling laboratory tests; 4) Testing THCM models with data from the FEBEX *mock-up* and *in situ* tests; and 5) Evaluation of the long-term geochemical evolution of HLW repositories in granite and clay with reactive transport models.

Contents

List of Figures

List of Tables

List of terms and abbreviations

Greek Terms

α	bentonite compressibility
α_T	thermal Cauchy coefficient (W/ºC)
$\emptyset$	porosity
θ^g	volumetric gas content (m^3/m^3)
θ	volumetric water content (m^3/m^3)
ρ_d	dry density (kg/m^3)
ρ^g	gas density (kg/m^3)
ρ^l	water density (kg/m^3)
ρ_s	solid density (kg/m^3)
σ'	mean effective stress (Pa)
Ψ	suction (kPa)
τ	solute tortuosity in water phase
τ^g	solute tortuosity in gas phase
τ^v	vapor tortuosity
μ^l	liquid viscosity (kg/m·s)
μ^g	gas viscosity (kg/m·s)
Ω_m	ratio between the ion activity product and the equilibrium constant
θ, η	parameters of the kinetic law
γ_i	activity coefficient of the i-th dissolved primary species
ν_{fi}	stoichiometric coefficient of the fith gas on the iith dissolved species
Λ	bulk thermal conductivity (W/mºC)
$\Lambda^w, \Lambda^v, \Lambda^a, \Lambda^s$	thermal conductivities of water, vapor, air and solid particles
π_h	osmotic pressure (Pa)
ε	strain

Latin Terms

A, B, C, D	empirical constants for the state-surface for the FEBEX compacted bentonite
b_1, b_2, b_3, b_4, b_5	coefficients derived by fitting the equation of logK values at 0, 25, 60, 100 and 300ºC
c	concentration of dissolved chemical species
c_{ae}	concentration of aqueous extract

c_b	solute concentrations of the boundary water
c_D	dimensionless concentration of dissolved chemical species
c_i	concentration of conservative species in the clay pore water
C_f^0	concentration of the f-th gas species (mol/L) in the sink term
C_j^0	total dissolved concentration of the j-th species (mol/L) in the sink term
C_f	total concentration of the f-th gas species (mol/kg) in the gaseous phase
C_j'	total concentration of the f-th gas species (mol/L) in the gaseous phase
C_j	total dissolved concentration of the j-th species (mol/L)
C_T^s	coefficient of the thermal expansion of the solid particles (1/ºC)
d	molecular diameter of the f-th gas species (m)
D^f	dispersion coefficient in gaseous phase (m^2/s)
D_g^f	diffusion coefficient of the f-th gas species (m^2/s) in a pure and ideal gaseous phase
D^j	dispersion coefficient in the liquid phase (m^2/s)
D_o	molecular diffusion in water (m^2/s)
D^v	dispersion coefficient for the vapor (m^2/s)
D_e^v	effective molecular diffusion for the vapor (m^2/s)
e	void ratio
Ea	apparent activation energy of the reaction (kJ/mol)
F_A, F_D, F_H	advection, molecular and dispersion mass flux vector ($kg/m^2/s$)
F	dilution factor
F_f	activity coefficient of the f-th gas species
h	average specific enthalpy of the soil (J/kg)
h^w, h^v, h^a, h^s	specific enthalpies of free water, vapor, air and solid particles
j^v	dispersive mass flux of the vapor
$K_{Na\text{-}cation}$	selectivity coefficient for cation exchange with respect to Na^+
K	thermodynamic equilibrium constant
k^{il}	intrinsic permeability of the liquid (m^2)
k_{rl}	relative permeability of the liquid
k^{ig}	intrinsic permeability of the gas (m^2)
k_{rl}	relative permeability of the gas
k_m	kinetic rate constant at 25ºC ($mol/m^2/s$)
k_T	thermo-osmotic permeability ($m^2/K/s$)
L	length of the experiment
M	molecular weight of the f-th gaseous species (g/mol)
m_g	mass of gas per unit volume of medium (kg/m^3)
m_l^w	mass of liquid water per unit volume of medium (kg/m^3)
M_s	mass of powdered clay sample in the aqueous extract method

M_w	molecular weight (g/mol)
N_{avog}	Avogadro's number
N_C	number of primary species
N_g	number of gaseous species
P	gas phase pressure (kPa)
p^a	atmospheric pressure (Pa)
P_f	partial pressure of the f-th gas species
P_j	total precipitated/dissolved mineral (mol/L)
P_l	liquid pressure (kPa)
P_g	gas pressure (kPa)
q^g	volumetric gas flux
q^l	volumetric liquid flux
Q_c	heat flux
r	radial distance for radial-flow
R	gas constant
r_c	corrosion rate (μm/year)
r_c	condensation rate (kg/m^2/s)
r_D	dimensionless radial distance for radial-flow
R_e	external radio
r_e	evaporation rate (kg/m^2/s)
r_f^i	sink term in the gas transport equation (kg/m^3/s)
R_f	chemical reaction source/sink the gas transport equation (mol/m^3/s)
RH	relative humidity
R_i	internal radio
r_i	sink term in the transport equation (kg/m^2/s)
r_m	dissolution/precipitation rate (mol/m^2/s)
S_g	gas saturation degree
S_l	liquid saturation degree
t	time
T	temperature (ºC)
T*	external temperature (ºC)
T_b	boundary temperature
t_D	dimensionless time
T_D	dimensionless temperature
T_h	heater temperature
T_{ref}	reference temperature (ºC)
V	cumulative water intake
V_D	dimensionless cumulative volume intake

V_P	bentonite pore volume
v^s	velocity of the particles (m/s)
w	gravimetric water content
w_{ae}	gravimetric water content of the aqueous extract
w_D	dimensionless water content
w_i	gravimetric water content of the clay sample
W_j	total cation exchanged concentration (mol/L)
x	distance from the hydration boundary for parallel flow
x_D	dimensionless distance from the hydration boundary for parallel flow
X_l^w	mass fraction of water in the liquid phase
X_g^a	mass fraction of air in the gas phase
X_g^v	mass fraction of vapor in the gas phase
Y_j	total sorbed concentration (mol/L)
z	advance of the saturation front in the Green-Ampt equation

Abbreviations

AET	Aqueous extract test
AGP	Almacenamiento geológico profundo
AXP	Almacenamento xeolóxico profundo
CEBAMA	Cement-based materials, properties, evolution, barrier functions Project
CEC	Cation exchanged capacity
CG	Hydrating and heating 60 cm-long bentonite test (*"Celdas Grandes"*)
CIEMAT	Centro de Investigaciones Energéticas, Medioambientales y Tecnológicas
CSH	Calcium silicate hydrate mineral phase
CT	Thermohydraulic cell of compacted bentonite test ("*Celdas Termohidrualicas"*)
DGR	Deep geological repository
EBS	Engineered barrier system
ENRESA	Empresa Nacional de Residuos Radiactivos S.A.
FB	Medium-size corrosion experiment
FEBEX	Full-scale Engineered Barrier Experiment
FEBEX-DP	Full-scale Engineered Barrier Experiment Dismantling Project
GMFV	Geochemical model reported by Fernández and Villar (2010)
HB	Concrete and bentonite interactions experiments (*"Hormigón bentonita"*)
HLW	High-level radioactive waste
NFPRO	Near Field Processes Project
OPC	Ordinary Portland Cement
PEBS	Long-term Performance of Engineered Barrier Systems Project

TDR	Time Domain Reflectometry
THCM	Thermo-hydro-chemical-mechanical
THQM	Termo-hidro-químico-mecánico
RAA	Residuos de alta actividad
SC	Small corrosion (experiment)
URL	Underground research laboratory
2I	Double interface mortar-bentonite-magnetite interaction experiment

Chapter 1. Introduction

1.1. Motivation and objectives

The storage of high-level radioactive waste (HLW) in a deep geological repository (DGR) is based on a multibarrier concept, which includes natural and engineered barriers. The natural barrier is the host rock while the engineered barriers include the waste form, the canister, and the bentonite buffer.

Significant research has been performed during the last decades to improve the knowledge, characterize the key parameters and the constitutive equations and develop numerical models for the HLW repository barriers. This research has been tackled within the framework of projects funded by the EURATOM Program of the European Commission. Significant parts of this dissertation have been developed within the PEBS (Long-term Performance of Engineered Barrier Systems), CEBAMA (Cement-based materials, properties, evolution, barrier functions) and FEBEX-DP Projects (Full-scale Engineered Barrier Experiment Dismantling Project).

The main objective of this dissertation is the updating and the testing of coupled thermal, hydrodynamic, chemical and mechanical (THCM) models for the compacted bentonite barrier in a high-level radioactive waste repository. To achieve this objective, the following activities were carried out:

- Updating and improving the conceptual and numerical coupled thermo-hydro-chemical and mechanical models (THCM) of the bentonite barrier of a HLW repository.
- Implementing the improvements in the THCM code INVERSE-FADES-CORE and producing an updated version (INVERSE-FADES-CORE V2).
- Modeling laboratory tests.
- Testing THCM models with data from the FEBEX (Full-scale Engineered Barrier Experiment) *mock-up* and *in situ* tests.
- Modelling the long-term geochemical evolution of HLW repositories in granite and clay.

The following methodology has been used:

- Perform a survey and review of the scientific literature.
- Review the conceptual and numerical model.
- Update and improve the code INVERSE-FADES-CORE.
- Model the laboratory experiments.
- Test THCM models with data from the FEBEX *mock-up* and *in situ* tests.
- Perform long-term geochemical simulations for repositories in granite and clay.

1.2. State-of-the-art

1.2.1. Bentonite barrier in a radioactive waste repository

The storage of high-level radioactive waste (HLW) in a deep geological repository (DGR) is based on a multibarrier concept, which includes natural and engineered barriers. The natural barrier is the host rock while the engineered barriers include the waste form, the canister, and the bentonite buffer. FEBEX (Full-scale Engineered Barrier Experiment) is a demonstration and research project for the engineered bentonite barrier of a HLW repository. FEBEX is based on the Spanish reference concept for radioactive waste disposal in crystalline rock, which consists on the disposal of spent fuel in carbon steel canisters in long horizontal disposal drifts excavated in granite. The main physical, thermal, hydrodynamic, mechanical and geochemical properties of the bentonite were extensively studied during the project (ENRESA, 2000, 2006a). The FEBEX project includes the following two main large-scale experiments which started in February of 1997: 1) The *in situ* full-scale test performed at the Grimsel underground research laboratory (URL) in Switzerland; and 2) The *mock-up* test operated at the CIEMAT facilities in Spain (ENRESA, 2006a; 2006b; 2006c; Martín et al., 2006). These tests replicate a HLW repository in which the canisters with the spent fuel were replaced by heaters. Laboratory tests were carried out with different sizes, durations, heating, and wetting conditions (Villar et al., 2012). Some of them were performed in the so-called thermohydraulic cells (CT), which are 13 cm-long, during 1 to 6 months (Fernández et al., 1999; Cuevas et al., 1997; ENRESA, 2006a; 2006b; 2006c). Other heating and hydration (HH) tests were performed in 60 cm-long cells (CG tests) with durations ranging from 0.5 to 7.6 years (Villar et al., 2008a).

Villar et al. (2012) presented a summary of the information gathered during 15 years on the saturation of compacted FEBEX bentonite obtained from heating and hydration

laboratory tests, the *mock-up* test, and the *in situ* test. They analyzed the hydration rate, the temperature and the water content data and their relevance for the rate of saturation and vapor migration through the bentonite buffer.

Villar el at. (2008b) presented a coupled THM model of the CG cells performed with CODE_BRIGHT (Olivella et al., 1996) by using a 1-D axis-symmetric finite element mesh. The model reproduces the general trends observed THM data in the tests. Fernández and Villar (2010) reported the geochemical data and presented a geochemical model of the CG7.6 test (GMFV) to interpret and derive the pore water composition. The geochemical model was performed with PHREEQC2 (Parkhust and Appelo, 1999).

Some geochemical reactions such as smectite dissolution are often ignored in short to medium-term geochemical models because they can be disregarded in the short term. Savage et al. (2010c) studied the potential contribution of the smectite hydrolysis to the long-term geochemical processes in a KBS-3 bentonite buffer. They concluded that smectite dissolution could be significant for the future geochemical state of a buffer, but the time scale of this process is too long for experimental verification. Smectite dissolution has the beneficial effect of leading to a slight decrease (1 cm) of the thickness of the altered bentonite zone (Johnson et al., 2014; Samper et al., 2016).

1.2.2. Bentonite and iron interactions

Iron-bentonite interactions and the effects of corrosion products on the bentonite were first identified by NAGRA in the mid 1980's (Savage, 2012). Extensive experimental studies and numerical models of the iron-bentonite interactions and the effects of corrosion products on the bentonite have been performed in recent years (ENRESA, 2004; Montes-H et al., 2005; Bildstein et al., 2006; De Wint and Torres, 2009; Wersin et al., 2007; Samper et al., 2008; Savage et al., 2010a; Marty et al., 2010a, 2010b; Lu et al., 2011, Turrero et al., 2011; Torres el al., 2013; Ngo et al., 2014, Samper et al., 2016). Corrosion tests were performed to ascertain the effects of the corrosion products in the bentonite during the NFPRO project (ENRESA, 2005, Torres et al., 2008).

Some numerical models predict that magnetite will be the main corrosion product (Samper et al., 2008; Lu et al., 2011, Samper et al., 2016) while others predict also the formation of Fe-bearing aluminosilicates (Wersin et al., 2007; Savage et al., 2010a; Marty et al., 2010a; Ngo et al., 2014) and ferrous hydroxide (De Windt and Torres, 2009). Bildstein et al. (2006) modelled the interactions of a carbon-steel canister with the MX-80 bentonite and the clay formation in the French reference system at 50 ºC over 10.000 years. They considered

the following corrosion products: iron oxides and hydroxides, iron carbonates, and iron-rich smectite and Fe-phyllosilicates. Wersin et al. (2007) studied the impact of iron components released from the canister corrosion on the bentonite buffer (MX-80) within the KBS-3H concept using the Olkiluoto site in Finland. They accounted for iron corrosion, cation exchange, protonation/deprotonation, Fe(II) surface complexation and thermodynamic and kinetic mineral dissolution/precipitation. Samper et al. (2008) presented 1-D and 2-D multicomponent reactive transport models to simulate the interactions of corrosion products with bentonite in the near field of a repository in granite. Numerical simulations were performed at a constant temperature of 25 ºC for 0.3 Ma. They found that magnetite is the main corrosion product. Magnetite precipitation reduces the bentonite porosity. Lu et al. (2011) presented an updated version of the model of Samper et al. (2008) which considers 3 types of sorption sites in the bentonite, kinetically-controlled canister corrosion and magnetite precipitation, and the competition of Ni^{2+} for sorbing sites. Savage et al. (2010a) reported a model of the iron-bentonite interactions based on natural analogues. They claim that the sequence of the alteration of the clay by Fe-rich fluids may proceed via an Ostwald step sequence. They modelled iron corrosion and the alteration of the MX-80 bentonite. Savage et al. (2010b) found that smectite dissolution may be significant for the future geochemical state of a buffer, but the time scale of this process is too long for experimental verification. Marty et al. (2010a) modelled the long-term alteration of the engineered bentonite barrier in an underground radioactive waste repository. Their study focused on the feedback effects of geochemical reactions on the transport properties of compacted MX-80 bentonite. Their calculations were performed at 100 ºC to estimate the maximum thermal effect on the mineralogy of the engineered barrier. The model was run for 10^5 years. Ngo et al. (2014) presented a coupled transport-reaction model for the long-term interactions of iron, bentonite and Callovo-Oxfordian (COX) claystone which extended the work of Marty et al. (2010a) by investigating the influence of the reactive surface area of the primary minerals on the bentonite and the COX claystone and the diffusion coefficient on the evolution of the iron-bentonite system.

1.2.3. Bentonite and concrete interactions

The interactions of cement-claystone barriers have been studied by laboratory experiments and industrial and natural analogues (Savage et al., 1992; Bauer and Berger, 1998; Steefel and Lichtner, 1998; Huertas el al., 2000; De Windt et al., 2004; Melkior et al., 2004; Soler et al., 2004; Tinseau et al., 2006; Gaucher and Blanc, 2006; Yang et al., 2008; Fernández et al., 2009b; Savage, 2011; Savage et al., 2011; Berner et al., 2013; Kosakowski and Berner, 2013; Shao et al., 2013; Watson et al., 2013; 2016; Lalan at al., 2016; Cuevas at

al., 2016; Lothenbach et al., 2017). Cuevas et al. (2016) performed test on double interface cells with mortar, bentonite and magnetite powder. Several sets of tests of concrete-bentonite columns tests were performed to study the interactions of concrete and bentonite (Turrero et al., 2011; Torres et al., 2013).Recently, Alonso et al. (2017) and Fernández at al. (2017) presented the interactions of the concrete and bentonite interface of the concrete plug in the FEBEX *in situ* test.

Extensive reactive transport modelling studies of the long-term cement-bentonite interactions and the effects of the hyperalkaline plume have been performed during the last 25 years (Fritz and Madé, 1991; Savage et al., 2002; 2010b; Watson et al., 2007; 2009a; 2009b; Ueda et al., 2007; Yamaguchi et al., 2007; Fernández et al., 2009a; Marty et al., 2009, 2010a; Lehikoinen, 2009; Savage, 2012). Shao et al. (2013) performed reactive transport simulations of the Maqarin marl rock natural analogue for 500 years with a 1-D model by using the OpenGeoSys-GEM code. Their results show pore clogging with the precipitation of ettringite and CSH phases in the marl rock exposed to the hyperalkaline plume in a band of 0.5 to 1 cm. According to the numerical model, the pores of the clay rock formation become clogged after $2 \cdot 10^4$ years. Watson et al. (2016) presented reactive transport simulations of the mineral-fluid interactions along the fractures of the Maqarin analogue and concluded that the fracture sealing is likely to occur when hyperalkaline fluids derived from cement degradation come into contact with rocks saturated with neutral pH and bicarbonate-rich groundwaters. Kosakowski and Berner (2013) presented numerical reactive transport calculations to evaluate the geochemical evolution at cement-clay interfaces for different transport scenarios through several Opalinus clay rocks for a time span of $2 \cdot 10^3$ years. High pH, mineralogical and porosity changes are restricted to narrow zones for all host rocks. The clogging of the pore space leads to a strong reduction of diffusive fluxes across the interface, which stops the geochemical alteration processes and significantly slows down mass transport across the interface. Berner et al. (2013) presented the simulations of the interactions of a MX-bentonite buffer with a low-pH concrete and the Opalinus Clay. Calculations were performed for $3 \cdot 10^4$ years with the OpenGeoSys-GEM code. Their results show that the thickness of the zone containing significant mineralogical alterations is at most a few cents of mm in both the bentonite and the Opalinus Clay adjacent to the liner. The precipitation of minerals reduces the porosity near the bentonite-concrete and concrete-Opalinus Clay interfaces. The effect is more pronounced and faster at the concrete liner-Opalinus Clay interface. The simulations reveal that significant pH changes (i.e. pH > 9) in the bentonite and the Opalinus Clay are limited to zones less than 10 cm thick after $3 \cdot 10^4$ years. Watson et al. (2013) performed a reactive transport modelling of a cement-clay interface at the industrial analogue of Tournemire (France) by using QPAC, the Quintessa's general-purpose modelling software. The sample overcoring and extraction in

boreholes filled with concrete and cement, which have had remained in contact with the natural mudstone for 15-20 years, allowed the mineralogical characterization of the alterations observed around the concrete-mudstone interface. In the concrete and in the mudstone there is a general increase in porosity while there is a reduction in porosity at both sides of the concrete-mudstone interface. Watson et al. (2013) concluded that the inclusion of the cation exchange in the base model reduces the extent of the hyperalkaline plume in the mudstone. However, the pH profile is almost unaffected when protonation/deprotonation reactions on the montmorillonite surface are considered in the model. Yang et al. (2008) presented a numerical model of water flow, heat transfer and multicomponent reactive solute transport to evaluate the long-term geochemical evolution in the bentonite barrier, the concrete and the clay formation for a potential geological radioactive waste repository in a clay formation. Calculations were performed for 1 Ma by using the CORE^{2D} V4 code. They concluded that: 1) The dissolution of the CSH minerals in the concrete causes an increase in pH to 13; 2) The porosity of the bentonite buffer decreases from 0.4 to 0.3; and 3) The hyperalkaline plume from the concrete migrates 70 cm into the clay formation over the time range of 1 Ma.

1.2.4. Coupled THCM processes, codes and models

The geochemical evolution of the bentonite barrier during the initial stages of the hydration and heating of the repository depends on the thermal, hydrodynamic and mechanical processes. The mathematical formulation of the coupled thermo-hydro-mechanical processes has been reported by Cox and Pruess (1990), Olivella et al. (1996), Yu-Shu Wu and Pruess (1999), Navarro and Alonso (2000) and Yu-Shu Wu et al. (2004). Existing THC codes includes: TOUGHTREACT (Xu and Pruess, 2001); RETRASO (Saaltink et al., 2004); MULTIFLOW (Lichtner, 1996); CRUNCH (Steefel, 2001); FRACON (Nguyen et al., 2005); and OpenGeoSys (Kolditz et al., 2012). Heating and hydration experiments were interpreted using THM (Villar et al., 2008b; Gens et al., 2009) and THC numerical models (Zheng and Samper, 2005, 2008; Zheng et al., 2008, 2010 and 2011). Later, coupled THCM models were used to study the coupled THCM processes for the repository performance assessment (Guimaraes et al., 2007; Samper et al., 2008; Zheng et al., 2008; Zheng and Samper, 2008; Zheng et al., 2010; Zheng et al., 2011;).

1.3. Scope

This dissertation includes 13 chapters, which describe the main contents of the dissertation. The details of the contributions of the dissertation are described in 13 appendixes. One of them is the Spanish version of the Extended Summary.

Chapter 2 describes the mathematical formulation of the coupled thermo-hydro-chemical and mechanical processes which includes the formulation of the reactive gas transport implemented in this dissertation

Chapter 3 presents the main features of the THCM code INVERSE-FADES-CORE as well as the improvements, the updates, the verification and the benchmarking with other codes.

Chapter 4 deals with the integrated analysis of the available water intake, water content, temperature, pH and chloride concentration data for the FEBEX bentonite from laboratory tests and the *mock-up* and the *in situ* tests.

Chapter 5, 6, 7 and 8 are devoted to the THCM models of laboratory experiments. Chapter 5 presents the THCM models of the heating and hydration tests performed by CIEMAT on 60 cm long cells. The THCM models of the heating and hydration corrosion tests are presented in Chapter 6. Chapter 7 describes the THCM model of the heating and hydration test with concrete-bentonite interactions in the HB4 cell. Chapter 8 describes the THCM models of the mortar-bentonite interactions in the double interface cells.

The models of the large-scale FEBEX *mock-up* and *in situ* tests are presented in Chapter 9. This chapter includes the updating of the 1-D THCM model of the *in situ* test, the updated geochemical predictions of the bentonite barrier in hot and cold sections at the dismantling of the *in situ* test in 2015, the prediction of the tracer migration, and the prediction of the geochemical interactions of the bentonite with the concrete plug.

The reactive transport modelling of the long-term interactions of corrosion products and compacted bentonite in a HLW repository in granite is presented in Chapter 10. Chapter 11 presents the long-term non-isothermal reactive transport model of the compacted bentonite, concrete and corrosion products in a HLW repository in clay.

Chapter 12 summarizes the main conclusions of the dissertation and lists the recommendations for future work.

Chapter 2. Mathematical formulation of THCM models

2.1. Introduction

Modelling the geochemical evolution of the bentonite barrier during the early stages of a HLW repository requires the use of models which account for the thermal gradients caused by the heat released from the waste, the multiphase phase flow of air, vapor and liquid water, bentonite swelling and the geochemical reactions involving aqueous, exchanged, sorbed and mineral species. The mathematical formulation of the coupled thermo-hydro-mechanical processes are presented by Cox and Pruess (1990), Olivella et al. (1996), Yu-Shu Wu and Pruess (1999), Navarro and Alonso (2000), and Yu-Shu Wu et al. (2004). Zheng et al. (2010) presented thermo-hydro-chemical models of the FEBEX bentonite.

This chapter presents the mathematical formulation of the coupled THCM model of the bentonite barrier in a high-level radioactive waste repository. The formulation includes the description of the reactive gas transport which has been implemented in INVERSE-FADES-CORE V2 in this dissertation. The details of the reactive gas transport can be found in Appendix 1.

2.2. Coupled THCM processes in a bentonite barrier in a HLW repository

The Spanish reference concept of a high-level radioactive waste repository in granite (ENRESA, 2000) consists on the disposal of spent fuel elements in cylindrical carbon steel canisters placed in horizontal disposal drifts. The disposal drifts, having 500 m in length and 2.4 m in diameter, are located at a depth of 500 m in a granite formation. The distance between disposal drifts is 35 m. The canisters are spaced 2 m. The canisters are 4.54 m long, 0.10 m thick and have an external diameter of 0.90 m. The reference concept of a high-level radioactive waste repository in clay, on the other hand, includes additionally, a 0.3 m thick concrete sustainment located between the bentonite buffer and the clay formation. (ENRESA, 2004)

The bentonite buffer is the sealing material for the waste disposal. Bentonite has a very low permeability and is able to retain radionuclides without large alterations. The bentonite in the repository will be subject to high temperatures generated by the nuclear waste package and to the hydration from the host rock. The corrosion of the carbon steel of the canister and the concrete degradation may induce bentonite alterations, which could result in changes in bentonite parameters such as porosity, permeability, sorption and swelling.

The unsaturated bentonite is as porous medium with three phases: solid, liquid and gas. The main thermal and hydrodynamic processes include: 1) Advective flow in the liquid and gaseous phases; 2) Diffusive flow in the liquid and gaseous phases; 3) Advective heat transport in the liquid and gaseous phases; 4) Heat conduction through the three phase; and 5) Heat transfer between the phases.

The mechanical behaviour requires knowing the forces, strains, displacements and stresses. The hydration and heating of the bentonite affect the saturation degree and the suction pressure which in turn may induce changes in the strain and stress. The hydration and the drying of the bentonite may induce swelling and shrinkage, respectively.

Chemical reactions in the bentonite include: 1) Homogeneous reactions such as aqueous complexation, acid-base and redox reactions; and 2) Heterogeneous reactions such as cation exchange, surface complexation, mineral dissolution/precipitation, and gas dissolution/exsolution. Chemical reactions depend on temperature (T). In addition, the transport of reactive chemical species depend on flow and hydrodynamic (H) processes and mechanical (M) phenomena because the changes in porosity affect the dissolved concentrations and the transport processes.

This dissertation deals with coupled THCM numerical models which account for the interplays among thermal (T), hydrodynamic (H), chemical (C) and mechanical (M) processes (Figure 2.1). The numerical model accounts for most of the interactions between then THCM processes illustrated in Figure 2.1.

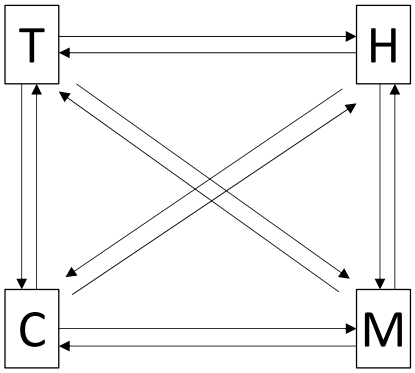

Figure 2.1. Scheme of the couplings between thermal (T), hydrodynamic (H), chemical (C) and mechanical (M) processes.

2.3. Mathematical formulation

Water mass balance is given by (Navarro and Alonso, 2000):

$$\frac{D_s m^w}{Dt} + m^w \nabla \cdot \boldsymbol{v}^s + \nabla \cdot \left(\rho^l X_l^w \boldsymbol{q}^l + \rho^g X_g^v \boldsymbol{q}^g + \boldsymbol{j}_v\right) = 0 \tag{2.1}$$

where $\frac{D_s()}{Dt}$ is the material derivative with respect to the solid particles which move with a velocity vector $\boldsymbol{v}^s$ (m/s), $\nabla \cdot ( )$ is the divergence operator, ρ^l and ρ^g are the bulk densities of the liquid and gaseous phases (kg/m^3), respectively, X_l^w is the mass fraction of water in the liquid phase, X_g^v the mass fraction of the vapor in the gas phase, $\boldsymbol{q^l}$ is the vector of volumetric liquid flux (m/s) which is given by Eq. (2.15), $\boldsymbol{q^g}$ is the vector of volumetric gas flux (m/s) which is given by Eq. (2.16), $\boldsymbol{j_v}$ is the dispersive mass flux of vapor with respect to the mean gas velocity (kg/m^2/s) which is given by Eq. (2.17), and m^w is the mass of water per unit volume of porous medium (kg/m^3) which is given by:

$$m^w = \emptyset\left[\rho^l X_l^w S_l + \rho^g X_g^v (1 - S_l)\right] \tag{2.2}$$

where ∅ is the porosity and S_l is the liquid saturation degree.

The air mass balance equation is given by (Navarro and Alonso, 2000):

$$\frac{D_s m^a}{Dt} + m^a \nabla \cdot \boldsymbol{v^s} + \nabla \cdot \left(\rho^g X_g^a \boldsymbol{q^g} + \rho^l X_l^a \boldsymbol{q^l}\right) = 0 \tag{2.3}$$

where X_g^a is the mass fraction of air in the gaseous phase, X_l^a is the mass fraction of air in the liquid phase, and m^a is the mass of air per unit volume of porous medium (kg/m^3) which is given by:

$$m^a = \emptyset\left[\rho^g X_g^a (1 - S_l) + \rho^l X_l^a S_l\right] \tag{2.4}$$

The solid mass balance is given by (Navarro and Alonso, 2000):

$$\frac{D_s \rho^d}{Dt} + \rho^d \nabla \cdot \boldsymbol{v^s} = 0 \tag{2.5}$$

where ρ^d is the dry density of the medium which is equal to $\rho^s(1 - \emptyset)$, where ρ^s is the density of the solid particles (kg/m^3). If the coefficient of the thermal expansion of the solid particles (1/ºC), C_T^s, is considered and the mechanical compressibility of the particles is disregarded, then Eq. (2.5) becomes:

$$\frac{D_s \emptyset}{Dt} = (1 - \emptyset)\left[\nabla \cdot \boldsymbol{v_s} - C_T^s \frac{D_s T}{Dt}\right] \tag{2.6}$$

where T is the temperature (ºC).

The formulation assumes that all phases are at local thermal equilibrium and therefore they are all at the same temperature. Hence, the energy balance is described in terms of an equation of internal energy which is defined by the following balance of enthalpy:

$$\frac{D_s h}{Dt} + h\nabla \cdot \boldsymbol{v^s} + \nabla \cdot (-\Lambda \cdot \nabla T + \boldsymbol{I^e}) = 0 \tag{2.7}$$

where h is the average specific enthalpy of the soil (J/kg) which in turn is given by:

$$\begin{aligned} h = {} & \rho^l X_l^w \emptyset S_l h^w + \rho^l X_l^a \emptyset S_l h^a + \rho^g X_g^v \emptyset (1 - S_l) h^v + \rho^g X_g^a \emptyset (1 - S_l) h^a \\ & + \rho^l X_l^a \emptyset S_l h^a + \rho^s (1 - \emptyset) h^s \end{aligned} \tag{2.8}$$

where h^w, h^v, h^a and h^s are the specific enthalpies of free water, vapor, air and solid particles respectively, which are assumed to depend linearly on temperature and specific heat (Navarro and Alonso, 2000) and $\boldsymbol{I^e}$ is the vector of convective energy flux which is given by:

$$\boldsymbol{I^e} = \rho^l X_l^w h^w \boldsymbol{q^l} + \rho^g X_g^v h^v \boldsymbol{q^v} + \rho^g X_g^a h^a \boldsymbol{q^g} \tag{2.9}$$

where $\boldsymbol{q^g}$ is the vector of volumetric vapor flux (m/s) which is given by the last terms of Eq. (2.1), that is, $\boldsymbol{q^v} = \rho^g X_g^v \boldsymbol{q^g} + \boldsymbol{j^v}$ and $\boldsymbol{\Lambda}$ is the bulk thermal conductivity tensor (W/mºC) which for unsaturated bentonite is computed as a volume-weighted average of the conductivities of the components according to:

$$\boldsymbol{\Lambda} = \emptyset S_l \boldsymbol{\Lambda^w} + X_l^a \emptyset S_l \boldsymbol{\Lambda^a} + \emptyset(1 - S_l)(\boldsymbol{\Lambda^v} + \boldsymbol{\Lambda^a}) + (1 - \emptyset)\boldsymbol{\Lambda^s} \tag{2.10}$$

where $\boldsymbol{\Lambda^w}$, $\boldsymbol{\Lambda^v}$, $\boldsymbol{\Lambda^a}$ and $\boldsymbol{\Lambda^s}$ are the thermal conductivities of water, vapor, air and solid, respectively. This equation is inspired in the formulation of De Vries's (1963) which according to Tang et al. (2008) provides the best fit to measured thermal conductivity data for several bentonites such as FEBEX bentonite. The formulation in Eq. (2.10), however, may not be the appropriate for courser porous materials.

According to Soler (2001), the Dufour effect is negligible compared to thermal conduction and therefore can be disregarded.

The following incremental formulation of the equilibrium equation of Navarro and Alonso (2000) is used:

$$\nabla \cdot (\Delta \boldsymbol{\sigma}' + \Delta P^g \boldsymbol{\delta}) + \Delta \rho g \boldsymbol{k} = 0 \tag{2.11}$$

where $\Delta\rho$ is the increment of the average soil density, g is the gravitational acceleration (m/s^2), $\boldsymbol{k}$ is the unit vector in the gravity direction, $\boldsymbol{\delta}$ is the vector expression of Kronecker's delta, ΔP^g is the increment in gas pressure (Pa) which for saturated conditions should be replaced by the increment in the liquid pressure (Pa), ΔP^l, and $\Delta\boldsymbol{\sigma}'$ is the vector of increments of effective stress (Pa) which is related to the vector of increments of total stress $\Delta\boldsymbol{\sigma}$ (Pa) in unsaturated conditions through:

$$\Delta \boldsymbol{\sigma}' = \Delta \boldsymbol{\sigma} - \Delta P^g \boldsymbol{\delta} \tag{2.12}$$

while for saturated conditions the previous equation is replaced by $\Delta \boldsymbol{\sigma}' = \Delta \boldsymbol{\sigma} - \Delta P^l \boldsymbol{\delta}$ (Fredlund and Rahardjo, 1993).

Solute transport processes include advection, molecular diffusion, and mechanical dispersion. Each of them produces a solute flux per unit surface and unit time. There are as many transport equations as primary chemical species in the system. The mass balance equation for the j-th primary species is given by (Zheng and Samper, 2008):

$$m_l^w \frac{\partial C_j}{\partial t} + \frac{\partial \left(m_l^w P_j\right)}{\partial t} + \frac{\partial \left(m_l^w W_j\right)}{\partial t} + \frac{\partial \left(m_l^w Y_j\right)}{\partial t} = L^*\left(C_j\right) + r_i\left(C_j^0 - C_j\right) \quad j = 1,2,\dots,N_c \tag{2.13}$$

where C_j is the total dissolved concentration of the of j-th species (mol/L), m_l^w is the mass of liquid water per unit volume of medium (kg/m^3) which is equal to $\rho^l X_l^w \theta$, where $\theta = S_l \emptyset$ is the volumetric watercontent (m^3/m^3), P_j, Y_j and W_j are the total precipitated, sorbed and exchanged concentrations (mol/L), respectively, of the j-th primary species, r_i is the sink term (kg/m^2/s), C_j^0 is the dissolved concentration of j-th species (mol/L) in the sink term r_i, N_c is the number of primary species. $L^*(\,)$ is the following transport operator:

$$L^*(\,) = \nabla \cdot \left[m_l^w \boldsymbol{D^j} \cdot \nabla(\,)\right] - m_l^w \boldsymbol{q^l} \cdot \nabla(\,) + (r_e - r_c)(\,) \tag{2.14}$$

where $\boldsymbol{D^j}$ is the dispersion coefficient (m^2/s), and r_c and r_e are the condensation and evaporation rates (kg/m^2/s), respectively.

Coupled transport phenomena such as thermal and chemical osmosis may be important for compacted bentonites (Keijzeret al., 1999; Keijzer and Loch, 2001; Soler, 2001). The volumetric liquid flux, $\boldsymbol{q^l}$, includes the classical Darcian term together with the chemical and thermal osmotic terms:

$$\boldsymbol{q^l} = -\frac{\boldsymbol{K^{il}} k^{rl}}{\mu^l}\left(\nabla p^l + \rho^l g \nabla z\right) - k_T \nabla T + \sigma \frac{\boldsymbol{K^{il}} k^{rl}}{\mu^l} \nabla \pi_h \tag{2.15}$$

where p^l is the liquid pressure (Pa), $\boldsymbol{K^{il}}$ is the intrinsic permeability tensor of the liquid (m^2), k^{rl} is the relative permeability of the liquid, μ^l is the viscosity of the liquid (kg/m/s), z is the elevation, k_T is the thermal-osmotic permeability (m^2/K/s), π_h is the osmotic pressure (Pa), and σ is a dimensionless reflection coefficient for chemical osmosis which measures the non-ideality of a membrane and is defined as the ratio of the applied osmotic pressure to the developed hydraulic pressure at equilibrium. An ideal membrane has a reflection coefficient of 1 whereas it varies between 0 and 1 for non-ideal membranes.

The volumetric gas flux, $\boldsymbol{q^g}$, is given by:

$$\boldsymbol{q^g} = -\frac{\boldsymbol{K^{ig}} k^{rg}}{\mu^g}\left(\nabla p^g + \rho^g g \nabla z\right) \tag{2.16}$$

where $\boldsymbol{K^{ig}}$ is the intrinsic permeability tensor of the gas (m^2), k^{rg} is the relative permeability of gas, μ^g and is the viscosity of the gas phase (kg/m/s).

The dispersive mass flux of vapor, $\boldsymbol{j^v}$, is calculated by the Fick's law:

$$\boldsymbol{j^v} = -\rho^g \boldsymbol{D^v} \nabla X_g^v \tag{2.17}$$

where $\boldsymbol{D^v}$ is the hydrodynamic dispersion tensor for vapor (m^2/s) which includes the effects of mechanical dispersion and molecular diffusion. The effective molecular diffusion coefficient for the vapor, D_e^v , (m^2/s) is calculated from (Pollock, 1986):

$$D_e^v = \frac{5.9 \cdot 10^{-6} \tau^v (T + 273.15)^{2.3}}{p^g} \tag{2.18}$$

where τ^v is the vapor tortuosity (dimensionless).

The mechanical law is given by:

$$d\boldsymbol{\varepsilon} = \boldsymbol{C} d\boldsymbol{\sigma'} + \boldsymbol{\beta} d\Psi + \boldsymbol{\alpha} dT \tag{2.19}$$

where $\boldsymbol{\varepsilon}$ is the strain vector, C is the elastic matrix (1/Pa), $\boldsymbol{\beta}$ is a vector of coefficients (1/Pa) which account for the deformation caused by changes in suction Ψ, $\Psi = (p^l - p^g)$, and $\boldsymbol{\alpha}$ is a vector of thermal expansion coefficients (1/ºC). The standard sign convention used in Soil Mechanics is adopted here according to which compressions are positive.

To overcome the difficulties of the different mechanical models, some researchers have resorted to simpler models such as the state-surface approach to simulate bentonite swelling. Nguyen et al. (2005) used successfully the state-surface approach to interpret a swelling pressure test. The following state-surface expression of Lloret and Alonso (1995) has been adopted in this dissertation to model bentonite swelling:

$$e = A + Bln\sigma' + Cln(\Psi + p^a) + Dln\sigma'\ln(\Psi + p^a) \quad (2.20)$$

where e is the void ratio which is equal to the volume of voids divided by the volume of the solids; p^a is the atmospheric pressure in Pa, σ' is the mean effective stress in Pa; Ψ is suction in Pa, and A, B, C and D are empirical constants which for FEBEX compacted bentonite are *A* = 0.76, *B* = -0.052446, *C* = -0.0406413 and *D* = 0.00479977 (Nguyen et al., 2005).

The chemical model for compacted bentonite accounts for the following reactions: aqueous complexation, acid/base, redox, cation exchange, surface complexation and mineral dissolution/precipitation. The chemical system is defined in terms of the concentrations of the primary species. The concentrations of the secondary species are computed from the concentrations of the primary species through appropriate mass action laws (Xu et al., 1999). The concentrations of the precipitated, exchanged and adsorbed species are computed using similar equations. A detailed description of the calculations of the chemical reactions can be found in Xu et al. (1999) and Zheng et al. (2011). The Gaines-Thomas convention is used for cation exchange. Surface complexation is modelled using three types of protonation/deprotonation sites, S^S-OH, S^{W1}-OH and S^{W2}-OH, as proposed by Bradbury and Baeyens (1997).

The equilibrium constants for aqueous complexes and minerals depend on temperature under non-isothermal conditions. They are calculated with the following expression which is valid for temperatures between 0 and 300 ºC:

$$logK(T) = \frac{b_1}{T^2} + \frac{b_2}{T} + b_3 lnT + b_4 + b_5 T \quad (2.21)$$

where b_1 to b_5 are coefficients which are derived by fitting Eq. (2.21) to measured $logK$ values at 0, 25, 60, 100 and 300ºC (Wolery, 1992).The thermodynamic database of EQ3/6 (Wolery, 1992) is used for aqueous complexes and minerals.

2.3.1. Reactive gas transport mathematical formulation

The reactive transport of gases could be relevant in the geochemical evolution of a HLW repository. H_2(g) can be generated and accumulated in the backfilling of the waste package by the corrosion of the steel canister (Xu et al., 2008), which may affect the long-term repository safety. On the other hand, the ambient CO_2(g) of the air can react with the calcium hydroxide of the concrete and cause concrete carbonation. The carbonation could affect the mechanical strength of the concrete and decrease the alkalinity of the bentonite in contact with the concrete. The high temperature in the bentonite buffer may cause water evaporation and CO_2(g) degassing which could decrease pH and lead to calcite precipitation. The revised

version of INVERSE-FADES-CORE, INVERSE-FADES-CORE V2, which accounts for the gas reactive transport in the gaseous phase, can deal with the previous gas-related chemical processes.

The reactive transport of the f-th gas species was implemented in this dissertation as an additional mass balance equation of the f-th gas species in the gaseous phase. The gas mass balance accounts for: a) Advection; b) Molecular diffusion; and c) Mechanical dispersion. Each one of these processes produces a gas flux per unit surface and per unit time. There are as many transport equations as gaseous species in the system. The gas transport equation for the f-th gas is given by:

$$\frac{\partial(\rho^g \theta^g C_f)}{\partial t} = -\nabla\left(\rho^g \boldsymbol{q_g} C_f - \rho^g \theta^g \boldsymbol{D^f} \nabla C_f\right) + r_f^i C_f^o - r_f^o C_f + R_f \qquad f = 1,2,\dots,N_g \tag{2.22}$$

where ρ^g is the gas density; C_f is the concentration of the of f-th gas species (mol/kg) in the gaseous phase; θ^g is the volumetric gas content ($\theta^g = S_g\emptyset$); $\boldsymbol{D^f}$ is the dispersion tensor of the f-th gas species; N_g is the number of gaseous species; r_f^i and r_f^o are the gas mass flux entering or leaving the system (kg/m^3/s), respectively; R_f is the gas chemical reactions term (mol/m^3/s); and C_f^o is the external concentration of the f-th gas species in the entering gas flux.

Reordering the Eq. (2.22) and applying the gas mass balance in the gas phase, the reactive gas transport equation is given by:

$$m_g \frac{\partial C_f}{\partial t} = -\rho^g \boldsymbol{q_g} \nabla C_f + \nabla\left(m_g \boldsymbol{D^f} \nabla C_f\right) + r_f^i\left(C_f^o - C_f\right) + R_f \qquad f = 1,2,\dots,N_g \tag{2.23}$$

where m_g is the mass of gas per unit volume of medium (kg/m^3) which is equal to $\rho^g \theta^g$. Similar to the solute transport equation (Eq. 2.13), the gas transport equation as:

$$m_g \frac{\partial C_f}{\partial t} = L^*\left(C_f\right) + r_f^i\left(C_f^0 - C_f\right) + R_f \qquad f = 1,2,\dots,N_g \tag{2.24}$$

where $L^*(\,)$ is the following transport operator:

$$L^*(\,) = \nabla \cdot \left[m_g \boldsymbol{D^f} \cdot \nabla(\,)\right] - \rho^g \boldsymbol{q^g} \cdot \nabla(\,) \tag{2.25}$$

The details of the reactive gas transport formulation are presented in Appendix 1.

Chapter 3. THCM code INVERSE-FADES-CORE

3.1. Introduction

The THCM models developed in this dissertation have been performed with INVERSE-FADES-CORE. INVERSE-FADES-CORE is a finite element code for non-isothermal multiphase flow and reactive transport in deformable media. The code is the result of integrating the capabilities of FADES (Navarro, 1997), CORE^{2D} (Samper et al., 2003), FADES-CORE (ENRESA, 2000; Juncosa, 2001) and INVERSE-CORE (Dai and Samper, 2004). The details of the formulation implemented in the code can be found in Navarro (1997), Juncosa (2001) and Zheng (2006).

This chapter presents the main features of INVERSE-FADES-CORE as well as the improvements, the updates, the verification and the benchmarking with other codes.

The details on code improvements, reactive gas transport, code verification and benchmarking can be found in Appendix 1.

3.2. Main features of INVERSE-FADES-CORE

INVERSE-FADES-CORE is a finite element code for modelling non-isothemal multiphase flow, heat transport and multicomponent reactive solute transport under both chemical equilibrium and kinetics conditions. The code takes into account the mass balance of water, air, solid and energy; the transport of solids; and mechanical equilibrium. The solute transport accounts for advection, molecular diffusion and mechanical dispersion. The code solves both forward and inverse multiphase flow and multicomponent reactive transport problems in 1-, 2- and 3-D axis-symmetric porous and fractured media (Zheng and Samper, 2004, 2005). State variables of the forward model include liquid and gas pressures and temperature, which are solved by a Newton–Raphson method. A sequential iteration method is used to solve the reactive transport equations. The concentrations of secondary species are computed from the concentrations of primary species through appropriate mass action laws

(Xu et al., 1999). A detailed description of the calculations of the chemical reactions can be found in Xu et al. (1999). The Gaines-Thomas convention is used for cation exchange. Surface complexation can be modelled by using up to three types of protonation/deprotonation sites, S^{S}-OH, S^{W1}-OH and S^{W2}-OH, as proposed by Bradbury and Baeyens (1997).

To overcome the difficulties of the different mechanical models, some researchers have resorted to simpler models such as the state-surface approach to simulate bentonite swelling. Nguyen et al. (2005) used successfully the state-surface approach to interpret a swelling pressure test.

3.3. Update of INVERSE-FADES-CORE

The numerical simulations performed in this dissertation have been performed with the updated version of INVERSE-FADES-CORE (INVERSE-FADES-CORE V2). The code has been updated and reviewed to debug programming errors, improve the input and output files and facilitate its use. The following corrections and improvements have been performed:

- Correction of a bug when reading and writing sorption data.
- Correction of the calculation of the kinetic rate of mineral dissolution/precipitation.
- Improvements in the following output files: *spx.out*, *int.out*, *mix.out*, *outiter*.
- Printing an output file with the calculated mineral volume fractions.
- Printing out the condition number of the Jacobian matrix for the solution of the chemical equations.
- Making operational the use of triangular elements.

INVERSE-FADES-CORE V2 accounts for gas reactive transport in the gaseous phase. The formulation of reactive gas transport implemented in INVERSE-FADES-CORE V2 includes additional mass balance equations for the reactive gaseous species in the gaseous phase. The mass balance equation for a given gas accounts for: a) Advection; b) Molecular diffusion; c) Mechanical dispersion; and d) Exchange with the liquid phase. The formulation of gas reactive transport in the gaseous phase is described in Appendix 1.

The formulation of the gas reactive transport implemented in INVERSE-FADES-CORE V2 was verified by comparing the numerical results of INVERSE-FADES-CORE V2 with the results computed with TOUGHREACT (Xu et al., 2008) for the following verification 1-D cases:

- Case 1. Prescribed gas partial pressures at the boundaries.
- Case 2. Prescribed gas partial pressure at the left boundary.
- Case 3. Prescribed partial pressure with a mineral.
- Case 4. No prescribed partial pressure with a mineral.

The numerical results of TOUGHREACT and INVERSE-FADES-CORE V2 coincide in most of the cases. However, there are some small differences especially near the boundaries. These differences could be due to differences in the numerical implementation of the boundary conditions and the numerical methods used by TOUGHREACT (integrated finite differences) and INVERSE-FADES-CORE V2 (finite elements). The results in Cases 1 and 2 tend to a constant value equal to the prescribed pressure at the boundaries (Figure 3.1). In Cases 3 and 4, calcite precipitates at x > 0.55 dm where the combination of the partial pressure of CO_2(g) (0.015 bar) and pH (7.1) leads to calcite precipitation (Figure 3.2). The calcite volume fraction computed with TOUGHREACT and INVERSE-FADES-CORE V2 are similar.

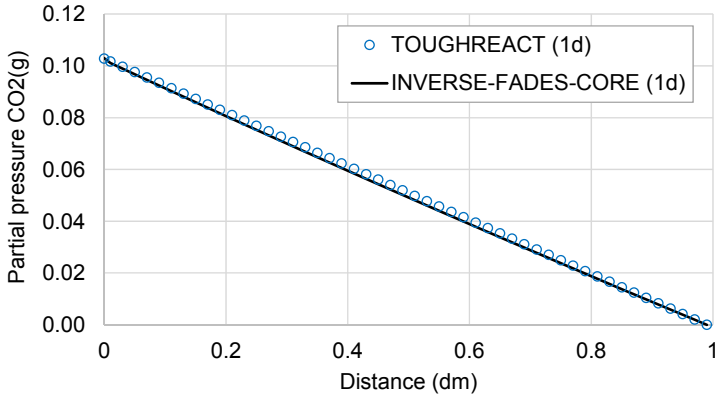

Figure 3.1. Computed partial pressure (bar) of CO_2(g) at 1 day with INVERSE-FADES-CORE (line) and TOUGHREACT (symbols) for the Case 1.

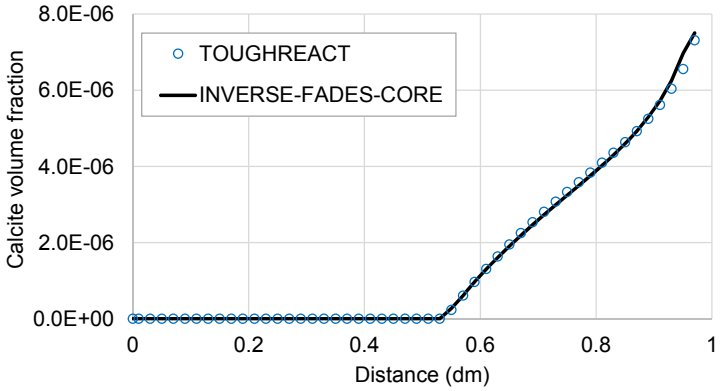

Figure 3.2. Calcite volume fractions computed with INVERSE-FADES-CORE (line) and TOUGHREACT (symbols) for the verification Case 4.

3.4. Benchmarking of INVERSE-FADES-CORE V2

Benchmark problems are indispensable to increase the confidence and the reliability of the simulation tools. The objectives of the benchmarks are achieved by comparing the numerical results of the same problem computed with different codes. INVERSE-FADES-CORE V2 has been benchmarked against others codes by means of two benchmarking problems which are presented in Appendix 1. The first benchmark deals with modeling the chemical interactions of a concrete liner with the compacted bentonite of the engineered barrier and the host clay rock under isothermal and non-isothermal conditions. The second bechmark is focused on the carbonation of concrete in unsaturated conditions during the repository operational stage. Benchmarking results are shown in Appendix 1.

Chapter 4. Integrated analysis of thermal, hydrodynamic and chemical data of compacted FEBEX bentonite

4.1. Introduction

A large number of hydrodynamic, geochemical and thermal data have been collected for compacted bentonites during the last 30 years to characterize their properties and evaluate their suitability for the Engineered Barrier System (EBS) of a high-level radioactive waste repository. Laboratory and *in situ* heating and hydration experiments on compacted bentonites have been performed within European Projects such as FEBEX I, FEBEX II, NFPRO and PEBS for various sizes (from 0.1 m to more than 10 m) and durations that range from a few months to more than 14 years. Villar et al. (2012) presented a summary of the information gathered during 15 years on the saturation of compacted FEBEX bentonite obtained from heating and hydration laboratory tests, the *mock-up* test and the *in situ* test. They analyzed the hydration rate, temperature and water content data and their relevance for the rate of saturation and vapor migration through the bentonite buffer. The analysis of Villar et al. (2012) has been extended and expanded in this dissertation by considering hydrochemical data and performing a dimensional analysis of the data. The dimensional analysis is a mathematical tool to establish relationships among physical quantities by using their dimensions. Dimensionless variables were defined for cumulative water intake, water content, temperature, pH and concentration of dissolved Cl^- in terms of dimensionless space and time. Analytical solutions based on the Green-Ampt method have been developed for bentonite hydration under parallel and radial flow conditions to facilitate the integration of cumulative water intake.

The FEBEX project includes two main large-scale experiments, the *in situ* full-scale (Figure 4.1a) test and the *mock-up* test (Figure 4.1b) operated by CIEMAT. Laboratory tests were carried out on thermohydraulic cells (CT) (Figure 4.1c), which are 13 cm-long, during 1 to 6 months; and on 60 cm-long cells (CG) (Figure 4.1d) with durations ranging from 0.5 to 7.6 years. These tests have different geometries and experimental conditions. Water hydration in CT and CG cells takes place at the bottom and the upper surfaces, respectively. Water flow in

these cells is one dimensional and parallel to the axis of the cells. Hydration in the *mock-up* and *in situ* tests occurs through the outer surface and exhibits axial symmetry.

Appendix 2 presents the main features of the FEBEX heating and hydration experiments and the available data. The appendix describes the Green-Ampt analytical solutions for bentonite hydration and presents the dimensionless expressions for the key variables and the integrated dimensional analysis of cumulative water intake, water content, temperature and chemical concentration data.

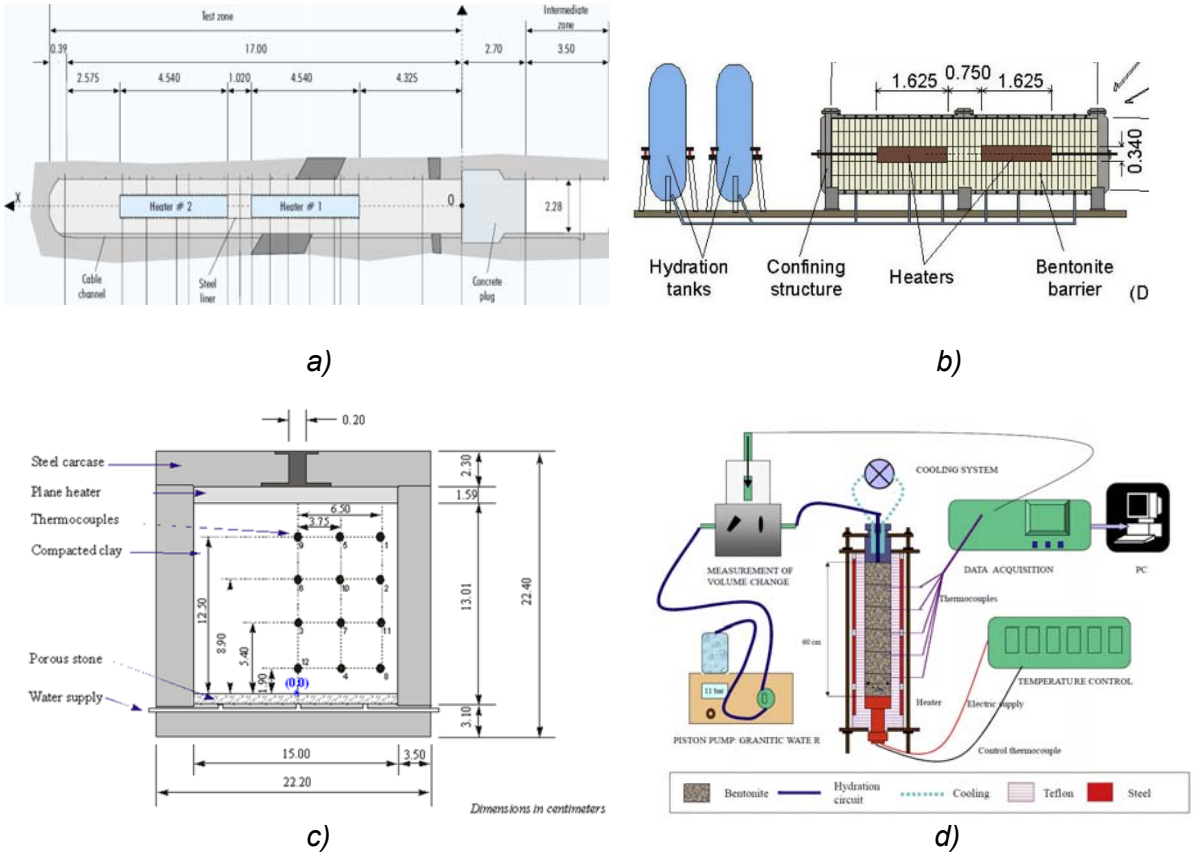

Figure 4.1. Schematic design of the *in situ* test (ENRESA, 2000) (top left), the *mock-up* test (Martín et al., 2006) (top right), the CT cells (Fernández et al., 1999) (bottom left), and the CG cells (Villar et al., 2008a) (bottom right).

4.2. Green-Ampt analytical solutions for water intake

The analytical solutions for parallel and radial flow show significant differences. The analysis of these differences was performed by comparing the equations of the depth of the hydration front, *z*, the infiltration rate, *q*, and the cumulative intake, *V*, for both cases. The most relevant parameters in these equations are the thickness of the sample, the volume of the bentonite and the hydration surface. The Green-Ampt equations for radial flow have been

compared with the solution for parallel flow for the following cases: 1) The same thickness and volume of the sample as radial conditions; 2) The same thickness and hydration surface of the bentonite as radial conditions; 3) The same volume and hydration surface as radial conditions; and 4) The optimized thickness, volume and hydration surface. The best fit to the radial flow solution is obtained for the parallel flow solution by using the optimized values of the thickness, the volume and the hydration surface of the bentonite. The second best approximation corresponds to using the same volume and thickness of the bentonite for radial and parallel flow. It can be concluded that the cumulative water intake for radial and parallel flow are comparable when the volume and hydration surface of the tests are appropriately selected.

4.3. Dimensionless variables

The following dimensionless variables were defined:

$$V_D = \frac{V}{V_P} \tag{4.1}$$

$$t_D = \frac{K}{\rho g \alpha L^2} t \tag{4.2}$$

$$\theta_D = \frac{(\theta - \theta_i)}{\Delta\theta} \tag{4.3}$$

$$T_D = \frac{(T - T_b)}{(T_h - T_b)} \tag{4.4}$$

$$c_D = \frac{(c - c_b)}{(c_i - c_b)} \tag{4.5}$$

$$x_D = \frac{x}{L} \tag{4.6}$$

$$r_D = \frac{r}{(R_e - R_i)} \tag{4.7}$$

where V_D, t_D, θ_D, T_D, c_D, r_D, x_D are the dimensionless cumulative water intake, time, volumetric water content, temperature, concentration of dissolved chemical species, and radial distance for radial-flow and distance from the hydration boundary for parallel flow; V is the cumulative water intake; D is the diameter of the cell; L is the length of the experiment; θ_{sat} and θ_i are the saturated and initial volumetric water contents, respectively; $\Delta\theta = \theta_{sat} - \theta_i$, K, ρ and α are the bentonite permeability, density and compressibility, respectively; T_b and T_h are the boundary and the heater temperatures, respectively; c_b and c_i are the solute concentrations of the boundary water and the initial pore water, respectively; r is the radial distance from the hydration boundary, R_e and R_i are the external and internal radii for a radial-flow system,

respectively. x is the distance from the hydration boundary and L is the length of the sample in a parallel-flow system.

V_p is the bentonite pore volume. For parallel flow, V_p is given by:

$$V_p = \frac{\pi D^2 L}{4}\Delta\theta \tag{4.8}$$

For radial flow, V_p is given by:

$$V_p = \pi(R_e^2 - R_i^2)b\Delta\theta \tag{4.9}$$

4.4. Integrated analysis of cumulative water intake data

Measured cumulative water intake may contain measurement errors which in the CG cells are equal to about 15%. There are differences in the initial water content of the tests. The cumulative intake of the m*ock-up* test is larger than the water intake of other tests because the block joins and gaps of the bentonite barrier were flooded at the beginning of the *mock-up* test. The dimensional analysis of the measured cumulative water intake data show that the cumulative water intake data of the CT and CG cells and the *mock-up* test cannot be scaled up. There are large differences at early times due to an electric shutdown and the filling of the block joints. Such differences, however, decrease with time and become negligible for dimensionless times, t_D, greater than 0.04 (see Figure 4.2).

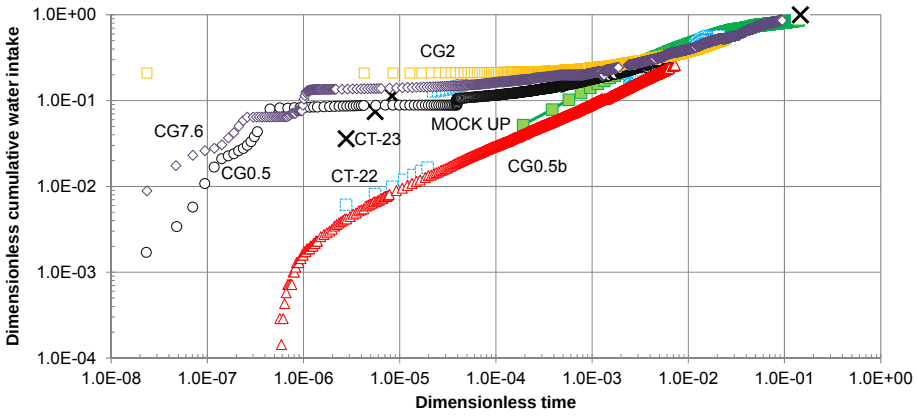

Figure 4.2. Time evolution of the dimensionless cumulative water intake versus dimensionless time for the CT (Fernández et al., 1999) and the CG cells (Fernández and Villar, 2010) and the *mock-up* test (ENRESA, 2006a).

4.5. Integrated analysis of water content data

The water content data for the *mock-up* test are larger than the water content data from other tests. This could be due to the fact that the water content is calculated from the relative humidity and the porosity is assumed to be constant. Water content data for the *mock-up* test for dimensionless times smaller than 0.04 are the largest for all the tests. The curves of the water content versus radial distance for the CG cells, the *mock-up* and *in situ* tests have similar slopes for t_D > 0.08. There are differences in water content data among the tests which could be due to differences in:

- The initial flooding. The joins and gaps of the *mock-up* test were flooded at the beginning of the test. This explains why the water content data for the *mock-up* test are always largest.
- The geometric configuration of the water flow and heat transfer.
- The thermal gradient. The temperatures at the boundaries are similar in most tests. However, the thickness of the bentonite ranges from 12 cm (CT cells) to 65 cm (*in situ* test). It should be taken into account that water evaporates near the heater. Vapor diffuses away from the heater and condenses later some distance away. This process retards the hydration of the bentonite buffer. This process is more relevant in the *in situ* test, where the water content is lower than the initial water content until t_D = 0.05.
- The internal boundary condition at the heater-bentonite interface. The bentonite is directly in contact with the heater in the CT and CG cells as well as in the *mock-up* test, whereas in the *in situ* test there is a metallic liner with a gap between the heater and the liner. The measured water content data in CT cells are smaller than those of the other tests because the CT cell was subjected to a higher thermal gradient.

4.6. Integrated analysis of temperature data

The analysis of temperature focused on the spatial distribution along the bentonite buffer. The temperature decreases from the heater to the hydration boundary. The curves of temperature versus distance from the heater show a large thermal gradient near the heater. The thermal gradient near the hydration boundary is smaller. The measured dimensionless temperature profiles show a slope of 0.8 which is similar for all the tests in the bentonite blocks near the heater and 0.35 in the half near to the hydration boundary. Boundary temperatures are similar in most of the tests (100ºC at the heater and about 20ºC at the hydration boundary).

Heat dissipation is especially relevant in the CG cells which show the smallest dimensionless temperatures, although the slopes are similar in all the tests. Heat dissipation through the top and the bottom boundaries is largest in the CT cells, due to the porous stone and the metallic heater plate.

4.7. Integrated analysis of chemical data

Chemical data were determined at the end of the heating and hydration tests. The chemical composition of the bentonite pore water was derived from aqueous extract tests which were interpreted numerically with inverse geochemical models. This added a difficulty to the integrated analysis of chemical data. In general, Cl^- concentrations are smallest near the hydration boundary and increase near the heater. The concentration of Cl^- in the central sections of the bentonite buffer is constant for early and intermediate times. The analysis of the dimensionless Cl^- concentrations from several tests shows that: 1) The Cl^- concentrations in the CT23 cell are much smaller than those of other tests; 2) There are significant differences in the Cl^- concentrations measured at several sections of the *in situ* test; and 3) The Cl^- concentrations decrease with time near the hydration boundary.

pH data from the CG cells and the *in situ* test are consistent. However, the pH data from the CT cells are markedly larger than the pH data for the CG cells and the *in situ* test. Possible reasons for the differences in chemical data among the tests include: 1) The method used to measure the chemical variables.; 2) The chemistry of the hydration water; 3) The geometric configuration of the flow (radial/parallel); 4) The thermal gradient; and 5) The differences in the experimental conditions such as heterogeneities in the barrier and the granitic rock in the *in situ* test.

4.8. Conclusions

Green-Ampt analytical solutions have been derived and used to compare radial and parallel flow through the bentonite. The comparison shows that the analytical solutions are markedly different. Such analysis shows that the best fit to compare radial and parallel flow is obtained by optimizing the parameters, especially the volume and the hydration surface. This should be taken into account when translating the results obtained in the tests, where the conditions are parallel, to radial flow conditions.

The integrated analysis of the cumulative water intake data shows an overall consistency. The largest differences occur at early times due to the differences in the experimental conditions, which decrease with time. Hydration data from most of the tests converge for dimensionless time larger than 0.04.

Water content data of the *mock-up* test are larger than those of the CT cells. The slope of the water content data are similar for the CG cell, and the *in situ* and *mock-up* tests for dimensionless times larger than 0.04.

The slope of the dimensionless temperature is about 0.8 in most of the tests. The integrated analysis of Cl^- shows that the general behavior is similar in most tests, except for the CT23 cell data. The pH data are consistent except for the CT cell.

The general THCM processes in the CT and CG cells, the *mock-up* and the *in situ* tests are similar. The general behavior of the cumulative water intake, water content, temperature and chemical concentration data are also similar in these tests. However, some differences have been found in the integrated analysis of the data which are caused by differences in the size, geometry and initial and boundary conditions in the tests.

The integrated analysis of measured THC data has shown that the data with different space-time scales from lab cell and column tests and the *mock-up* and *in situ* tests cannot be scaled up. The conclusions obtained from this integrated analysis are similar to those reported by Villar el at. (2012).

The dimensional analysis of hydrodynamic, thermal and chemical data assume that the density, the porosity and the hydraulic conductivity of the bentonite are constant. However, these parameters change during the tests (Villar et al., 2008b). The integrated analysis could be improved by: 1) Extending the Green-Ampt solution to account for water distribution, 2) Developing analytical solutions for temperature and concentration, and 3) Performing the integrated analysis of chemical data for reactive species.

The dimensional analysis has been useful to identify the role of experimental conditions, but it failed to provide a framework to integrate all the experimental data. Such integration is most likely to be achieved by means of coupled THCM numerical modelling. Coupled THCM numerical models constructed with data from lab tests and the *mock-up* and the *in situ* tests can be safely used for long-term predictions.

Chapter 5. Coupled THCM model of the heating and hydration tests on 60 cm long cells

5.1. Introduction

Laboratory experiments were performed within European Projects such as FEBEX I, FEBEX II, NFPRO and PEBS to characterize the thermal-hydrodynamic-chemical and mechanical properties of the compacted bentonite and evaluate the suitability of the bentonite barrier as a backfilling material for a HLW repository. Heating and hydration laboratory tests were performed on compacted bentonite, which mimic the conditions of the repository (ENRESA, 2000, 2006a).

This chapter presents a coupled THCM model of the heating and hydration tests performed on 60 cm long cells. This model extends the THM model of Villar et al. (2008b) and the geochemical model reported by Fernández and Villar (2010) (GMFV) because the THCM model accounts for geochemical reactions in addition to thermal, hydrodynamic and mechanical processes. The complex interplays among thermal, hydrodynamic, mechanical and geochemical processes can be represented appropriately with a coupled THCM model. In addition, this coupled THCM model provides a powerful tool for the analysis and understanding of the performance of the bentonite barrier of a HLW repository.

The details of the THCM model of the heating and hydration tests on 60 cm long cells are presented in Appendix 3.

5.2. Test description

CIEMAT performed a series of heating and hydration tests on cylindrical compacted bentonite samples 60 cm long and 7 cm in diameter (see Figure 5.1). These tests lasted from 0.5 to 7.6 years (Villar et al., 2008a). They include: the CG0.5 test (lasted 0.5 years), the CG1 test (lasted 1 years), the CG2 test (lasted 2 years) and the CG7.6 test (lasted 7.6 years). The

heating and hydration tests performed on 60 cm long cells (CG tests) provide a large amount of measured THCM data including:

- Temperature and water intake recorded during the tests.
- Water content, dry density and saturation degree measured at the end of the tests.
- Geochemical data such as dissolved species concentration, concentrations of exchanged cations and mineralogical observations at the end of the tests.

Some measured water intake data may contain errors caused by experimental artifacts. These errors were filtered and raw water intake data were corrected. The measured concentrations of the exchanged cations may also contain experimental errors. The concentrations of the exchanged cations were discarded whenever the total sum of the concentrations of the exchanged cations was smaller than 90% of the CEC of the natural FEBEX bentonite. The chemical composition of the bentonite pore water was estimated with the squeezing and the aqueous extract methods (Fernández and Villar, 2010). The dilution factor was calculated for each section by using the water content measured at the end of the test. The concentration of the conservative species Cl^- in the bentonite pore water samples was calculated for the CG0.5, CG1 and CG2 tests by multiplying the measured aqueous extract concentration by the dilution factor. The consistency between aqueous extract and squeezing Cl^- concentration data has been checked. Data showing large discrepancies were discarded.

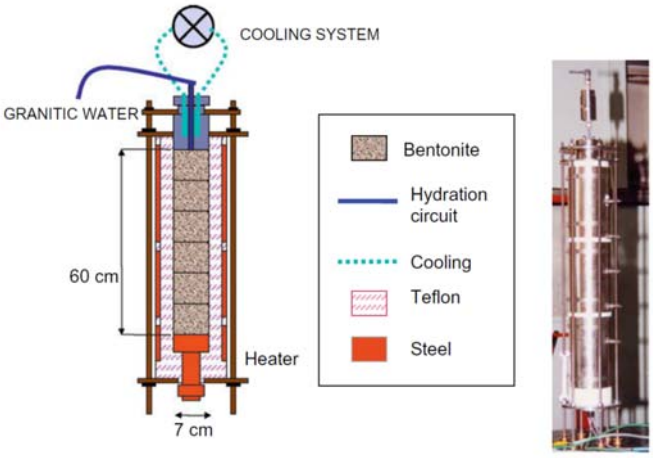

Figure 5.1. Experimental setup of the CG tests (Villar et al., 2008a).

5.3. Model calibration and results

The numerical model was performed with a 1-D finite element mesh with INVERSE-FADES-CORE V2. The model was performed in two stages. The results of the original (previous) model were compared to measured data in the testing stage. The comparison of the model results and the measured data revealed the following discrepancies: 1) The computed porosity is smaller than the measured data; 2) The computed water content and saturation degree near the heater are larger than the measured data; 3) The computed temperatures in the sensors are larger than the measured data; 4) The computed water intake overestimates the measurements; 5) The computed concentrations for the CG7.6 test are smaller than the concentrations of the geochemical model of Fernández and Villar (2010); and 6) The concentrations of the exchanged Ca^{2+} and Mg^{2+} do not fit the measured data.

The following improvements were performed in the revised model to overcome the previous discrepancies: 1) Adjusting the vapor tortuosity; 2) Considering lateral heat dissipation at the sensors; 3) Adjusting the selectivity coefficients; and 4) Updating the material properties of the elements located in the boundaries.

A slight increase in the vapor tortuosity from 0.3 to 0.4 leads to an increase in vapor diffusion, bentonite pore water evaporation near the heater and pore water concentrations. The numerical results with a vapor tortuosity of 0.4 reproduce the measured water content and Cl^- concentration data near the heater better than the previous model which has a vapor tortuosity of 0.3. This result confirms that the water content, relative humidity, water evaporation, solute concentration and mineral precipitation near the heater are very sensitive to small changes in the vapor tortuosity.

The blocks of compacted bentonite were installed inside Teflon cells, which had no thermal isolation. Therefore, a large amount of heat dissipation took place in these tests through the Teflon walls (Fernández and Villar, 2010). The revised or calibrated model accounts for the heat loss by means of a thermal Cauchy condition at the sensors. The computed temperatures with the revised model reproduce the measured temperatures at the sensors. The implementation of the Cauchy condition to simulate the lateral heat loss improves the representation of the temperatures. The thermal gradient decreases in the upper part of the cells (0.1 m < x < 0.5 m) and increases sharply near the heater (0.5 m < x < 0.6 m) to almost a value of 5ºC/cm. The large temperature gradient leads to an increase in the water evaporation and a decrease of the gravimetric water content near the heater.

The selectivity coefficients were calibrated in order to reproduce the initial concentration of the exchanged cations of the FEBEX bentonite. It should be taken into account that the numerical method used in INVERSE-FADES-CORE V2 initializes the concentrations of the dissolved species to achieve chemical equilibration with the minerals present in the system. The equilibration of the bentonite pore water with the mineral phases may change slightly the concentrations of some dissolved cations such as Ca^{2+}. Such change leads in turn to changes in the concentrations of the exchanged cations. The selectivity coefficients for cation exchange were adjusted to fit the measured concentrations of the exchanged cations. The concentrations of the exchanged cations computed with the revised model fit the measured exchanged cation data, but some discrepancies remain for exchanged Ca^{2+} and Mg^{2+}.

The definition of the material zone at the hydration interface has a strong impact in the numerical solution. There are significant differences in the water intake when the porous stone is considered. The differences in the treatment of the boundary condition increase with time. Similarly, the definition of the material zone at the bentonite-heater interface can affect the amount of water evaporation and the solute mass balance errors. It can be concluded that model results are very sensitive to changes in the boundary conditions at the heater interface and at the hydration boundary. Inappropriate conditions can lead to large changes in evaporation rates, solute concentrations, mineral precipitation near the heater and large mass balance errors.

The revised THCM model reproduces the general trends of the measured temperatures, porosities, gravimetric water contents, saturation degrees and water intake. Computed temperatures reach steady state in a few days. The computed temperatures in the bentonite are smaller than 50ºC, except in a 10 cm band near the heater where the temperature increases with a gradient of 5ºC/cm. The computed gravimetric water content near the hydration boundary increases due to bentonite hydration and swelling. The computed gravimetric water content near the heater, however, decreases from its initial value (0.14) to 0.05 in CG0.5, CG1 and CG2 tests and 0.085 in CG7.6 test due to pore water evaporation (see Figure 5.2). For the most part, the thermal, hydrodynamic and mechanical results of the THCM model agree with those reported by Villar et al. (2008b).

The concentration of dissolved Cl^- near the hydration boundary decreases due to the dilution caused by the hydration water. The concentration of Cl^- near the heater increases due to the water evaporation. In general, the computed Cl^- concentrations fit the measured data, but the computed results under predict the measured data near the hydration. The computed Cl^- concentrations of the CG2 test near the hydration boundary fit the measured data better

than those of the CG0.5 and CG1 tests. The computed Cl^- concentrations in the CG7.6 test are similar to those of the GMFV, except near the heater (see Figure 5.3).

Model results show that the calcite dissolves near the hydration boundary within the interval 0 < x < 0.1 m. Calcite shows a precipitation front, which moves through the bentonite with time from x = 0.05 m in t = 0.5 years to x = 0.3 m in t = 7.6 years. Calcite precipitates also near the heater.

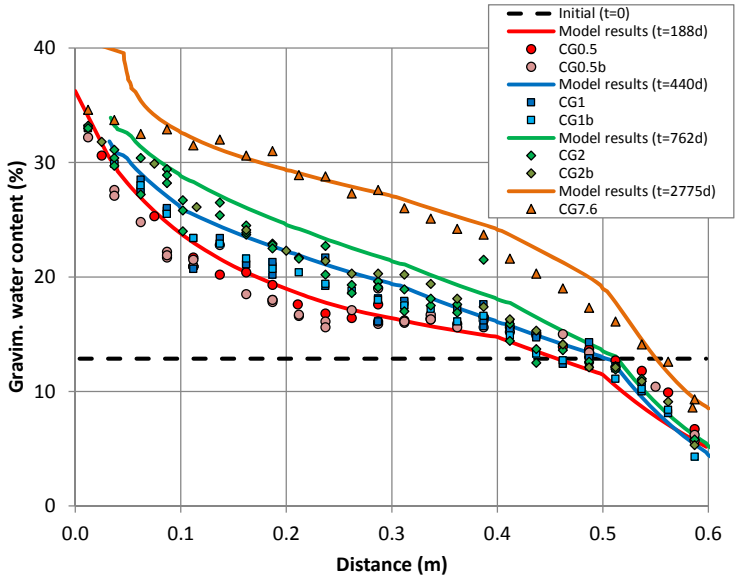

Figure 5.2. Spatial distribution of the measured (symbols) and computed (line) gravimetric water content at the end of the CG0.5, CG0.5b, CG1, CG1b, CG2, CG2b and CG7.6 tests.

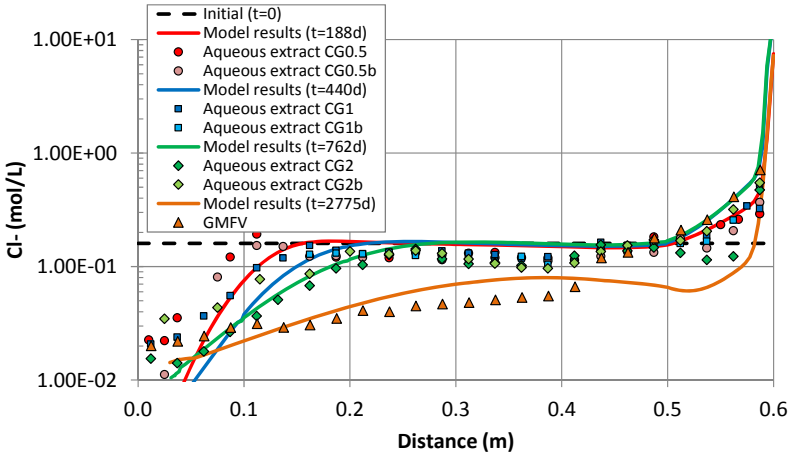

Figure 5.3. Spatial distribution of the measured aqueous extract (symbols) and the computed (lines) Cl^- concentrations at the end of the CG0.5, CG0.5b, CG1, CG1b, CG2 and CG2b tests. And comparison of the Cl^- concentrations reported by Fernández and Villar (2010) (symbols) and the computed (lines) Cl^- concentrations at the end of the CG7.6 test.

The concentration of dissolved bicarbonate and exchanged Ca^{2+} increase when calcite dissolves. On the other hand, the pH and the concentrations of dissolved Ca^{2+} and HCO_3^- and exchanged Ca^{2+} near the heater decrease when calcite precipitates. The pH decreases slightly in the CG7.6 test, except near the heater where the pH increases. The pH is about 7.5 throughout the bentonite and increases to 8.4 at the heater interface.

The computed concentration of gypsum shows a dissolution front which propagates from the hydration boundary into the bentonite column. Gypsum precipitates near the heater (0.5 m < x < 0.6 m) after the cooling stage in the CG7.6 test. Anhydrite shows an opposite behavior to that of gypsum. Anhydrite precipitates near the heater (0.45 m < x < 0.6 m) when the temperature is above 50ºC and dissolves after the cooling stage and precipitates as gypsum. The concentration of the dissolved sulphate is similar to the initial concentration, except near the heater where it increases sharply due to water evaporation.

The model predicts a small amount of chalcedony dissolution in the bentonite. The rate of dissolution is largest near the heater. The concentration of dissolved silica increases from its initial value due to chalcedony dissolution.

The computed concentrations of exchanged cations reproduce the general trend of the measured data for the CG0.5, CG1 and CG2 tests, except for exchanged Ca^{2+}. The model predicts an increase in the concentration of exchanged Na^+ and K^+ near the heater and a decrease of the concentration of the exchanged Ca^{2+} and Mg^{2+}. The changes in the concentration of exchanged Ca^{2+} are triggered by calcite precipitation/dissolution. The general trends of the computed concentrations of the exchanged cations in the CG7.6 test are similar to those of the CG0.5, CG1 and CG2 tests. However, the changes in the concentrations of exchanged cations are more pronounced.

The computed concentrations of the dissolved Ca^{2+}, Mg^{2+}, Na^+ and K^+ show trends similar to those of the GMFV. The THCM model reproduces the measured THM variables such as water intake, temperatures, water contents and porosities. The lack of a full set of chemical data has prevented a full calibration of the model with geochemical data. It should be taken into account that the geochemical data from the GMFV assume that the geochemical porosity is a very small part of the total porosity.

5.4. Conclusions

A coupled THCM model of the heating and hydration tests performed on 60 cm long cells has been presented. The model has been performed in two stages. Model results in the testing stage were compared to measured data. The comparison of the model results and the measured data shows the following discrepancies: 1) The computed porosity is smaller than the measured data; 2) The computed water content and saturation degree are larger than the measured data near the heater; 3) The computed temperatures are larger than the measured data in the sensors; 4) The computed water intake overestimates the measurements; 5) The computed concentrations for the CG7.6 test are smaller than the concentrations of the geochemical model of Fernández and Villar (2010); and 6) The concentration of the exchanged Ca^{2+} and Mg^{2+} do not fit the data. The following improvements were performed in the calibration stage: 1) Adjusting the vapor tortuosity; 2) Considering lateral heat dissipation at the sensors; 3) Adjusting the selectivity coefficients; and 4) Updating the material properties at the boundary elements. The revised THCM model reproduces the observed temperatures, saturation degrees, porosities. Moreover, model results fit the measured concentrations of the Cl^- and measured exchanged cations data for the CG0.5, CG1, CG2 tests. The computed concentrations of Cl^-, Na^+, Ca^{2+}, Mg^{2+}, K^+, HCO_3^-, SO_4^{2-} and pH reproduce the general trends of the results reported by Fernández and Villar (2010) for the CG7.6 test.

Chapter 6. Coupled THCM models of heating and hydration tests to study the interactions of Fe corrosion products and bentonite

6.1. Introduction

Corrosion tests are useful to ascertain the effects of the corrosion products in the bentonite. CIEMAT performed corrosion tests during the NFPRO (Near Field Processes) project to study the interactions of the bentonite and the corrosion products (ENRESA, 2005; Torres et al., 2008).

This chapter presents the THCM numerical models of two types of heating and hydration tests performed by CIEMAT to study the interactions of compacted bentonite and corrosion products under the conditions of a HLW repository. The experiments were performed at several temperatures on samples of different lengths. The 1-D THCM models performed include: 1) The corrosion tests on 25 mm long small cells (SC) at 25, 50 and 100ºC and with a duration of 180 days; and 2) The corrosion tests on 10 cm long medium-size cells (FB) at 100ºC and with a duration of 1593 days. The THCM models presented in this dissertation extend the model of the corrosion tests of De Windt and Torres (2009).

The details of the THCM numerical models of the heating and hydration corrosion tests can be found in Appendix 4.

6.2. Tests description

The corrosion tests on small cells, SC cells, were performed by CIEMAT. The cells contained 21 mm of compacted FEBEX bentonite and 4 mm of carbon-steel powder. The tests were performed at 25º, 50º and 100ºC. The durations of the tests were 6 and 12 months (Figure 6.1a). The corrosion tests performed on medium-size cells, FB cells, were carried out also at the CIEMAT facilities. They contain a 86.8 mm long sample of compacted FEBEX

bentonite and a layer of 13 mm of carbon-steel powder. The temperature was prescribed at 100ºC at the bottom of the cell (Figure 6.1b). The medium-size corrosion tests lasted from 6 months to 4.5 years.

The bentonite dry density, the water content and the saturation degree were measured at the end of the corrosion tests on small and medium-size cells. In addition, the temperature and the relative humidity were recorded at the sensors installed on the corrosion test on medium-size cells. The iron weight were measured at the end of the corrosion tests on small cells. Moreover, the concentration of the exchanged cations were measured at the end of the corrosion tests. Mineralogical observations indicate that $Fe(OH)_2(s)$ precipitates. These data were used to calibrate the kinetic parameters of the precipitation of the corrosion products.

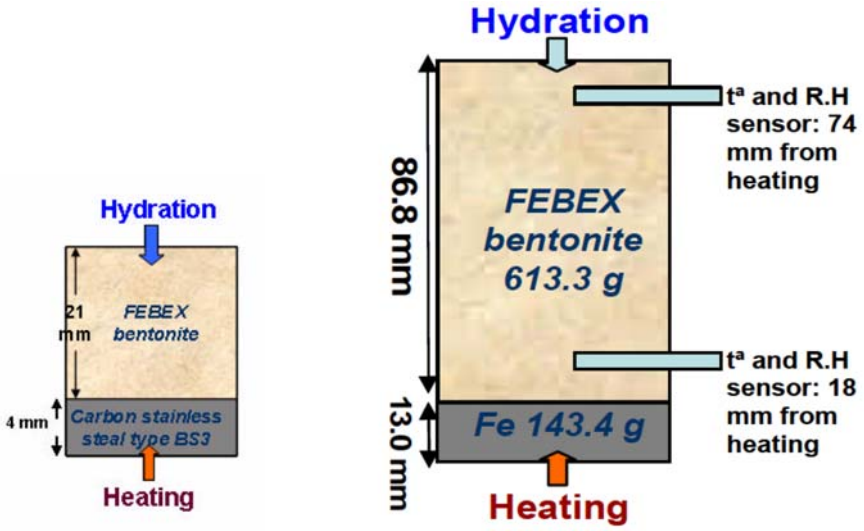

a) *b)*

Figure 6.1. Scheme of the corrosion tests on small cells (left) (Torres et al., 2008) and of the corrosion tests on medium-size cells (right) (Turrero et al., 2011).

6.3. Model results

The numerical models were performed with INVERSE-FADES-CORE V2 by using a 1-D finite element mesh. The THCM numerical models include the bentonite and the Fe powder. The models of the corrosion tests on small cells were performed for the tests at 25, 50 and 100ºC which lasted 6 months. The model of the corrosion test on the medium-size cell was performed for the FB3 test which lasted 1593 days.

Fe(s) corrosion was assumed to occur at a constant corrosion rate according to Lu et al. (2011) and Samper et al. (2016). The kinetic parameters of magnetite precipitation were taken from De Windt and Torres (2009).

The computed water content and the porosity increase near the hydration boundary to a value of 0.48 and decrease toward the Fe powder to values slightly larger than the initial values in the corrosion tests on small and medium-size cells. The models predict that the bentonite samples are almost saturated at the end of the tests, except near the Fe powder. The computed temperatures reach steady state in a few minutes. The temperature is uniform at 100ºC in the Fe powder because the specific heat and the thermal conductivity are larger than those of the bentonite. The computed water content, porosity and saturation degree fit the measured data at the end of the corrosion tests on small and medium-size cells. The computed temperature and relative humidity in the medium-size cell reproduce the measured data at the sensors, except the relative humidity near the heater where the measurements are affected by vapor leakage through the sensors.

The Cl^- concentration is affected by the hydration, the diffusion and the evaporation near the heater. The computed concentration of Cl^- near the hydration boundary decreases because the pore water concentration of the hydration water in smaller than that of the initial bentonite pore water. The computed Cl^- concentration at the Fe power increases due to water evaporation. Finally, Cl^- diffuses from the Fe powder into the bentonite during the cooling phase.

The computed concentrations of Na^+, K^+, Ca^{2+}, Mg^{2+} and SO_4^{2-} show trends similar to those of Cl^-. In addition, these species are subjected to mineral dissolution/precipitation and cation exchange reactions. The changes in the computed concentrations of Cl^-, Na^+, K^+, Ca^{2+}, Mg^{2+} and SO_4^{2-} in the corrosion test on medium-size cell are larger than those in the small corrosion tests because the test on the medium-size cell lasted longer than the tests on small cells.

Model results show that gypsum dissolves initially in the bentonite and then it remains constant. Anhydrite precipitates in the bentonite near the Fe power, but it dissolves soon after. The behaviors of the sulfate minerals are similar in both corrosion tests. The computed concentration of dissolved SO_4^{2-} is affected slightly by gypsum and anhydrite dissolution/precipitation.

The computed concentration of dissolved silica is controlled by quartz dissolution/ precipitation. The predicted dissolution of quartz in the bentonite, especially near the Fe powder leads to the increase of dissolved $SiO_2(aq)$ in the bentonite near the Fe powder.

The model predicts calcite dissolution in the bentonite near the hydration boundary and calcite precipitation near the Fe powder. A peak of calcite dissolution followed by calcite precipitation is computed in the corrosion test on medium-size cells near the Fe powder at large times. The computed concentration of HCO_3^- in the bentonite near the hydration boundary is smaller than that in the Fe powder. This pattern of dissolved HCO_3^- is related to calcite precipitation/dissolution.

The computed concentration of dissolved Fe^{2+} decreases in the bentonite and in the Fe powder, especially at the interface bentonite-Fe powder due to the precipitation of corrosion products and Fe^{2+} exchanged.

Magnetite and $Fe(OH)_2(s)$ precipitate in the Fe powder and at the bentonite-Fe powder interface is predicted in the corrosion test on small cells. Goethite precipitates at early stages and then it redissolves. Siderite does not precipitate. On the other hand, only magnetite precipitates in the Fe powder in the model of the corrosion test on the medium-size cells (see Figure 6.2). The predictions of the precipitation of corrosion products are consistent with the laboratory observations. The computed results reproduce the iron weight data (Figure 6.3) and the model results reported by De Windt and Torres (2009).

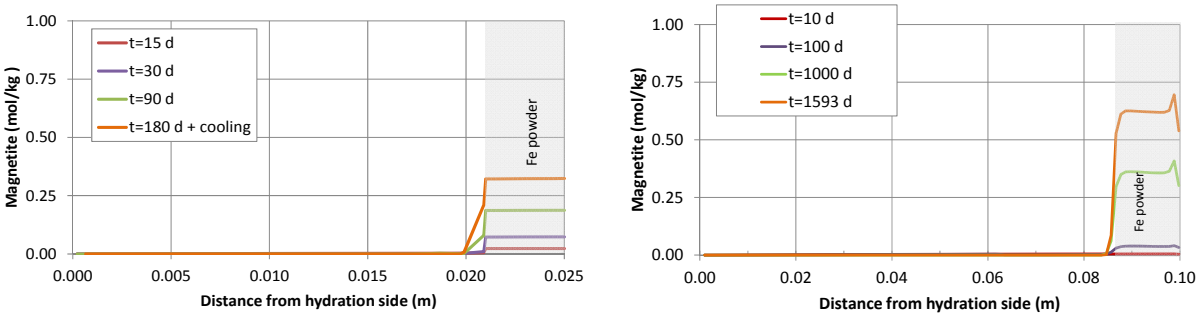

Figure 6.2. Spatial distribution of the computed cumulative magnetite precipitation at selected times in the corrosion test on small cell at 100ºC (left) and in the medium-size corrosion test on FB3 cell (right).

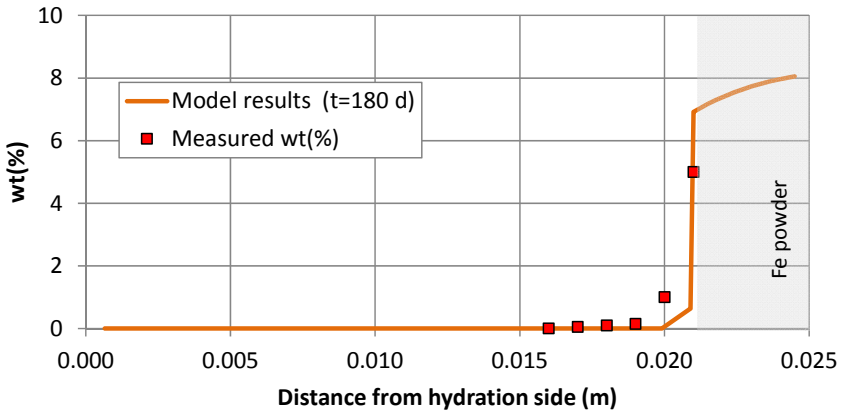

Figure 6.3. Measured (symbol) and computed (line) weight of precipitated iron hydroxide at the end of in the corrosion test on small cell at 100ºC (t = 180 days) and after cooling.

The concentration of exchanged Ca^{2+} decreases in the bentonite near the Fe powder where the calcite precipitates. The computed concentration of exchanged Mg^{2+} also increases near the Fe powder. On the other hand, the concentrations of exchanged Fe^{2+}, Na^{+} and K^{+} increase in bentonite near the Fe powder. Model results fit the measured cation exchange data, except for exchanged Na^{+}.

The computed pH in the bentonite decreases initially due to the thermal filed. The pH increases in the bentonite-Fe powder interface due to the precipitation of the corrosion products. The pH after the cooling phase is about 7.5 in the bentonite and 9 in the Fe powder. The computed Eh decreases with time to -0.6V due to corrosion. The models predict that S^{s}-OFe^{+} is the dominant sorbed species on the strong sites while S^{w2}-OH predominates on weak #2 sites and S^{w1}-OH and S^{w1}-OFe^{+} are the main sorbed species on the weak #1 sites in both corrosion tests.

6.4. Sensitivity analysis

The sensitivity analysis performed on the corrosion test on the small cells at 100ºC indicates that: 1) The precipitation of magnetite at equilibrium is larger than that computed with kinetically-controlled magnetite precipitation; 2) $Fe(OH)_2$(s) does not precipitate when magnetite precipitates at equilibrium; and 3) $Fe(OH)_2$(s) does not precipitate when the corrosion rate is decreased.

The general trends of the concentrations of the dissolved, exchanged and surface complexation complexes are similar in the corrosion tests performed on small cells at 25, 50 and 100ºC. Iron corrosion at 100ºC is larger than that at 25ºC and 50ºC because the corrosion rate increases with the temperature. The precipitation of magnetite is largest for the test at 100ºC and smallest for the test at 50ºC because the kinetic rate constant of magnetite is smallest for 50ºC. The numerical results fit the measured iron weight data for the tests at 50 ºC and 100ºC.

6.5. Conclusions

The corrosion tests carried out by CIEMAT have been modelled with coupled THCM models. The corrosion experiments include: 1) The small corrosion cells with a length of 25 mm and a duration of 180 days; and 2) The medium-size corrosion cells (10 cm long) with a

duration of 1593 days. The thermo-hydrodynamic model results fit the general trends of the measured data in the bentonite in both corrosion tests. There are some discrepancies in the computed time evolution of the temperature and relative humidity of the medium-size cells which could be attributed to problems in the water injection system during the tests and vapor leakage through the sensors.

The model results for the small corrosion cells indicate that: 1) Magnetite and $Fe(OH)_2(s)$ are the main corrosion products which compete for Fe^{2+} precipitation; 2) The corrosion products penetrate a few mm into the bentonite; 3) The numerical results fit the measured iron weight data; 4) Fe^{2+} sorbes by surface complexation; and 5) Fe^{2+} exchange is less relevant than Fe^{2+} sorption by surface complexation. Model results of the medium-size cells show that magnetite precipitates in the Fe powder. The experimental observations indicate that there is no magnetite precipitation in the bentonite. Some magnetite precipitation was observed at the interface, which is consistent with the small amount of magnetite precipitation computed at the interface.

The precipitation of magnetite at chemical equilibrium is larger than that computed with a kinetically-controlled precipitation. $Fe(OH)_2(s)$ does not precipitate when magnetite precipitates at equilibrium and when the corrosion rate is decreased.

Chapter 7. Coupled THCM model of the heating and hydration concrete-bentonite interactions in the HB4 cell

7.1. Introduction

The concrete barrier will be the support of the galleries in the Spanish conceptual reference for a HLW repository in clay rock (ENRESA, 2004). The concrete is a source of alkaline solutions. The precipitation of mineral phases at the interfaces might reduce drastically the porosity. Several laboratory experiments have been performed within NF-PRO (Near Field Processes) and PEBS (Long-term performance of Engineered Barrier System) projects to study this issue.

The concrete and bentonite tests (HB test) were carried out by CIEMAT on medium-size cells containing a 7.15 cm long bentonite sample in contact with a 3 cm long piece of concrete (see Figure 7.1). This chapter presents a 1-D coupled THCM model of the heating and hydration laboratory test performed on bentonite and concrete. The details of the model are presented in Appendix 5.

7.2. Test description

The concrete-bentonite column tests were performed at the CIEMAT facilities to study the interactions of concrete and bentonite (Turrero et al., 2011; Torres et al., 2013). The tests were carried out on medium-size cells containing a 7.15 cm thick bentonite sample in contact with a 3 cm thick piece of concrete (see Figure 7.1) which were hydrated and heated at 100ºC. The test duration ranged from 6 to 140 months.

Water content and dry density were measured along the cell at the end of the tests. The sensor installed in the bentonite columns recorded the relative humidity and temperature. The dissolved and exchanged concentrations were measured at the end of the tests. Mineral observations were also performed at the dismantling of the tests.

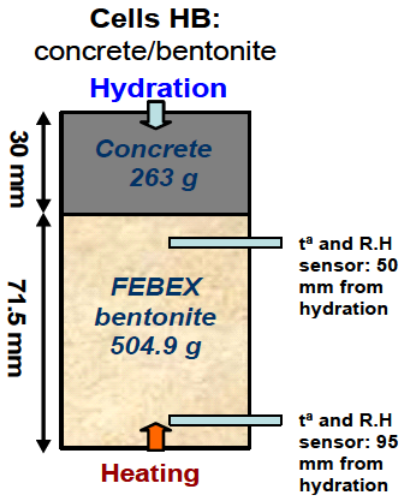

Figure 7.1. Scheme of the concrete-bentonite test on HB4 cell (Turrero et al., 2011).

7.3. Model results

The numerical model of the HB4 test was performed with INVERSE-FADES-CORE V2 by using a 1-D finite element mesh. The HB4 test lasted 54 months. The model includes the concrete (0 < x < 3 cm), and the bentonite (3 cm < x < 10.5 cm).

The bentonite hydrates through the concrete which gets fully saturated after 7 days. The computed water content in the bentonite near the concrete interface increases to 0.5 due to the hydration and decreases to 0.1 near the heater due to water evaporation. The computed porosity of the bentonite near the hydration boundary increases 25% due to the bentonite swelling and decreases 10% near the heater. The computed temperatures reach steady state in a few minutes. The computed relative humidities increase and reach steady state after 250 days with RH = 100% at the sensor located near the hydration boundary and RH = 40% near the heater. The computed relative humidity near the heater is smaller than that measured at the sensor.

The concentration of Cl^- in the bentonite decreases due to Cl^- diffusion from the bentonite into the concrete. The Cl^- concentration becomes uniform after 100 days. The concentrations of dissolved Na^+, Ca^{2+}, Mg^{2+} and SO_4^{2-} are also affected by the diffusion from the bentonite into the concrete. On the other hand, the concentration of the K^+ and pH in the bentonite increase due to the diffusion from the concrete into the bentonite. In addition, pH and the concentrations of the dissolved Na^+, Ca^{2+}, Mg^{2+}, K^+ and SO_4^2 are affected by cation exchange and mineral dissolution/precipitation.

Cristobalite dissolves in the bentonite near the heater due to the increase in temperature caused by the heater. The increase in temperature leads to an increase in the concentration of dissolved silica. Quartz dissolution in the concrete is not relevant. Calcite precipitates in the concrete near the hydration boundary and in the bentonite near the concrete interface. Calcite dissolves in the bentonite downwards the precipitation front.

The model predicts the dissolution of portlandite and CSH1.8 and a small precipitation of C0.8SH in the concrete. The concentration of dissolved calcium in the concrete increases initially due to the dissolution of portlandite and CSH1.8. Later, the concentration decreases due to calcite precipitation and the exchange of dissolved Ca^{2+} with exchanged magnesium. Therefore, the computed concentration of exchanged Ca^{2+} increases and that of exchanged Mg^{2+} decreases.

Similar to calcite, brucite precipitates in the concrete near the hydration boundary because the hydration water has a large concentration of magnesium. Brucite precipitates also at both sides of the concrete-bentonite interface. Sepiolite precipitates in the concrete near the bentonite interface.

Ettringite precipitates in the concrete near the hydration boundary and dissolves in the rest of the concrete. The dissolution rate is largest near the bentonite interface. Ettringite dissolution/precipitation affects the concentration of dissolved aluminum and SO_4^{2-}. The increase in the concentration of dissolved SO_4^{2-} in the bentonite is due to the large concentration of SO_4^{2-} in the hydration water, the dissolution of gypsum and anhydrite and the diffusion of SO_4^{2-} from the concrete into the bentonite.

The computed pH shows a sharp decrease at the concrete-bentonite interface which coincides with the precipitation of brucite in the concrete and the precipitation of calcite and sepiolite in the bentonite. The alkaline front penetrates and migrates through the bentonite. The pH front (pH > 8.5) reaches 1 cm into the bentonite after the cooling phase (Figure 7.2).

The most important changes in the porosity in the HB4 cell occur in: 1) The hydration boundary, 2) The concrete near the bentonite interface, and 3) The bentonite near the concrete interface. The porosity in the hydration boundary decreases when brucite precipitates. Calcite, ettringite, C1.8SH and C0.8SH precipitation also contribute to the decrease in the porosity. Their contributions, however, are much smaller than that of brucite. The porosity in the concrete near the bentonite interface reduces 51% due also to brucite precipitation. The porosity in the bentonite near the concrete interface decreases 14% when brucite, calcite and sepiolite precipitate. There is also a small decrease of the porosity (3%) near the heater due to the precipitation of gypsum and anhydrite after the cooling phase.

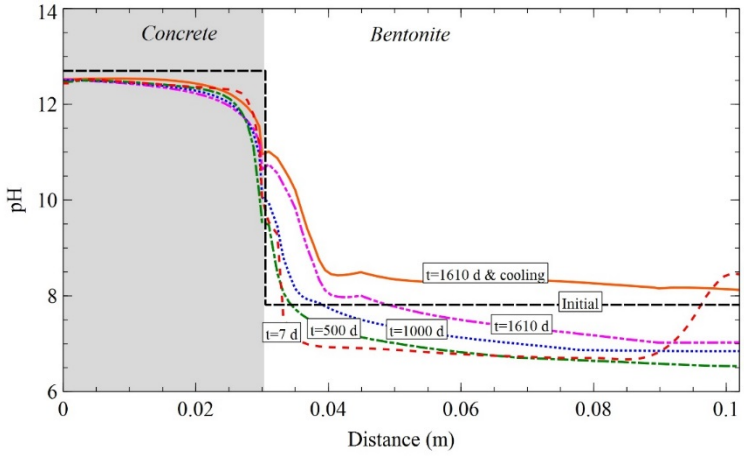

Figure 7.2. Spatial distribution of the computed pH in the HB4 cell at selected times.

For the most part, the numerical model reproduce the measured water content, porosity, temperature, relative humidity and captures the main trends of mineralogical laboratory observations. However, there are some discrepancies, especially for ettringite and CSH precipitation.

7.4. Conclusions

A coupled THCM model of the bentonite and the concrete test in the HB4 cell has been performed. The model reproduces the measured temperature, relative humidity, water content and porosity data. However, the model overestimates the relative humidity measured at the sensor near the heater. Model results show that advection is relevant during the first months of the test. Then, solute diffusion is the main transport process. The main mineralogical alterations are predicted to occur at the hydration boundary, the concrete near the bentonite interface, and the bentonite near the concrete interface.

Calcite and Mg phases precipitate at the hydration boundary due to the large concentrations of bicarbonate and magnesium in the hydration water. The largest amount of calcite and brucite precipitation take place at the bentonite and concrete near the interface. Sepiolite also precipitates in the concrete near the bentonite interface. The model predicts the dissolution of portlandite in the concrete and CSH1.8 and a small C0.8SH precipitation. Ettringite precipitates in the concrete near the hydration boundary and dissolves in the rest of the concrete. The porosity changes due to mineral precipitation/dissolution, especially at the hydration boundary and in the bentonite and concrete near the interface. The porosity reduces 51% in the concrete at the bentonite interface when brucite precipitate.

The pH front (pH > 8.5) diffuses into the bentonite 1 cm at the end of the test.

Model results capture the main trends of the mineralogical observations. The model, however, does not reproduce ettringite and CSH precipitation. The predicted precipitation for these phases is smaller than the observed values.

Chapter 8. Coupled THCM model of the mortar-bentonite interactions in the double interface cells

8.1. Introduction

The concrete barrier will be the support of the galleries in the Spanish reference concept for a geological repository in clay host rock (ENRESA, 2004). The mortar is a source of alkaline solutions resulting from the concrete degradation. The precipitation of mineral phases at the interfaces might reduce drastically the porosity of the bentonite and the clay host rock.

The so-called double interface tests were performed by CIEMAT during the PEBS Project to study the interactions of corrosion products, bentonite, and mortar at the ambient geochemical conditions of the repository expected to occur after 1,000 to 3,000 years. This chapter describes the THCM models of the mortar-bentonite interactions in the double interface cells. The details of the models are presented in Appendix 6.

8.2. Test description

The tests on double interface cells, 2I, were performed by CIEMAT on 25 mm long cells which contain: mortar, bentonite and magnetite powder (Cuevas et al., 2013; 2016) (see Figure 8.1). The temperature in the cells was maintained constant at 60ºC for 540 days. The inner 2.5 cm length of this cell includes 0.5 cm of mortar, 1.8 cm of pre-treated FEBEX bentonite and 0.2 cm of magnetite powder.

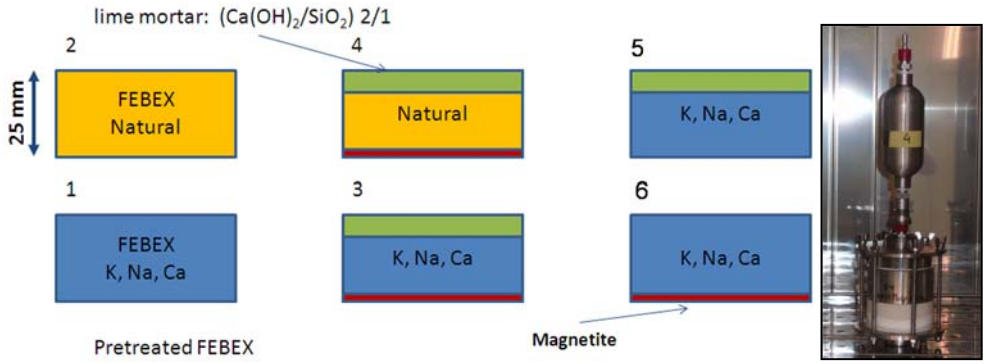

Figure 8.1. Scheme of the six double interface tests (Cuevas et al., 2016).

The available measured data include:

- The time evolution of the water intake.
- The water content and the dry density at the end of the tests.
- The concentrations of the aqueous species in the bentonite and the water of the tank, which were measured at the end of the tests.
- The mineralogical observations at the end of the tests.

8.3. Model description

The numerical model for the 2I3 cell was performed with a 1-D finite element mesh with INVERSE-FADES-CORE V2. The model accounts for the hydration system (the water tank, the water pipe and the filter), the lime mortar, the bentonite and the magnetite powder. The model considers the hydration system to reproduce the water leakage in the water tank and the backwards solution diffusion which occurred in some of the tests.

8.4. Model results

Model results show that the lime mortar, the bentonite and the magnetite powder are fully saturated at the end of the test. The final computed water contents are 0.3, 0.41 and 0.60 in the mortar, the bentonite and the magnetite, respectively. The computed water content corresponds to the total porosity because the system is saturated and the bentonite suffered a very small deformation. The computed water content, saturation degree and water intake reproduce the measured data at the end of the test.

The computed concentration of Cl^- increases in the mortar and decreases in the bentonite due to the diffusion from the bentonite into the mortar. The concentrations of Cl^- become uniform after a few days and equal to 0.058 mol/L. This concentration is ten times larger than that measured in the bentonite and smaller than the measured in the mortar. These discrepancies could be due to Cl^- sorption in the mortar or to the precipitation of chloride mineral phases.

The computed concentrations of dissolved Na^+, K^+, Ca^{2+} and Mg^{2+} show also the effect of diffusion. However, they are subjected also to cation exchange reactions. SO_4^{2-} and Al^{3+} diffuse from the mortar into the bentonite. These species are also subjected to mineral dissolution/precipitation.

The computed concentration of dissolved Ca^{2+} at the end of the test increases from the initial value. The dissolution of portlandite in the mortar and the diffusion of dissolved Ca^{2+} into the bentonite lead to the precipitation of calcite, CSH1.2 and CSH1.6 in the bentonite and mortar near the interface. The computed concentration of exchanged Ca^{2+} also increases in the bentonite at the end of the test.

The computed concentrations of dissolved and exchanged Mg^{2+} decrease from their initial values in the mortar near the hydration boundary and in the bentonite near the mortar interface due to the precipitation of brucite and sepiolite. In addition, sepiolite shows some precipitation peaks in the bentonite. Sepiolite, CSH1.6 and CSH1.2 precipitation lead to the decrease of the concentration of dissolved SiO_2(aq). The model predictions show a small amount of quartz precipitation and no crisbolatite precipitation.

The model predicts that anhydrite precipitates in the mortar and in the bentonite, but anhydrite is transformed into gypsum after the cooling phase. The computed dissolved concentration of SO_4^{2-} decreases when anhydrite and gypsum precipitate. The computed ettringite precipitation shows a peak in the bentonite near the mortar interface at early times. Later, it redissolves. Ettringite precipitation does not affect the concentrations of dissolved SO_4^{2-} and Al^{3+}.

For the most part, the numerical model captures the main trends of the mineralogical observations. However, there are some discrepancies, especially for ettringite precipitation in the mortar which is not computed with the model, and brucite precipitation in the bentonite that is not observed in the laboratory.

The porosity changes due to mineral dissolution/precipitation at the end of the test are small and limited to the mortar and a few mm in the bentonite. The porosity increases 8% in

the mortar near the bentonite interface due to portlandite dissolution. On the other hand, the porosity decreases 1.5% in the bentonite in a 0.2 mm thick zone near the mortar interface due to calcite and brucite precipitation.

The pH shows a diffusive front from the mortar into bentonite. The computed pH at the end of the test is about 10.5 in the mortar and the pH decreases from 10.5 at the interface to 8 in the first 10 mm of the bentonite (see Figure 8.2).

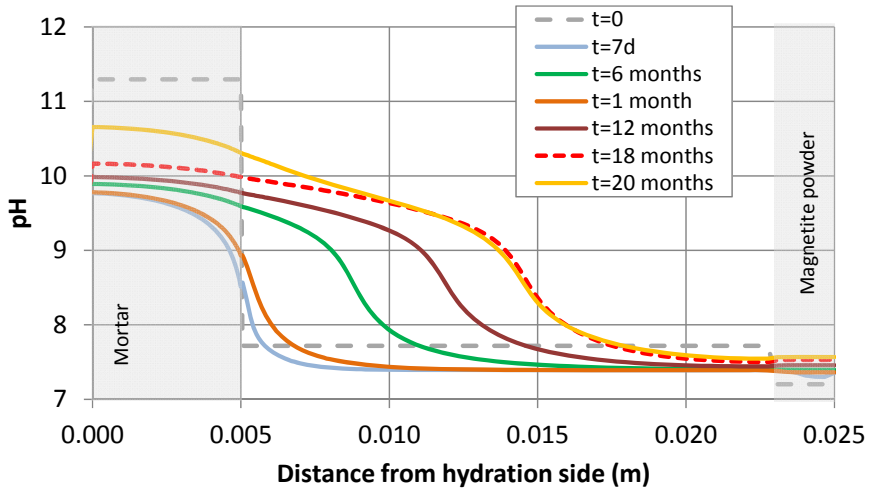

Figure 8.2. Spatial distribution the computed pH in the double interface 2I3 test at selected times.

8.5. Sensitivity analysis

The sensitivity analysis to the CEC and the initial composition of the exchange complex has been analyzed by modelling the double interface test on 2I 4 cell which was performed on a sample of natural FEBEX bentonite which has a CEC equal to 102 meq/100g. The computed exchanged concentrations at the end of the tests show similar patterns in the tests performed with natural and pre-treated FEBEX bentonite. The concentration of exchanged Ca^{2+} increases while the concentrations of the exchanged Mg^{2+} and Na^{+} decrease. Cation exchange reactions in the sample containing natural FEBEX bentonite are enhanced compared to the sample of pre-treated FEBEX bentonite. The concentrations of dissolved of Mg^{2+} and Na^{+} in the test containing natural FEBEX bentonite are larger than those of the pre-treated FEBEX bentonite test while the concentrations of dissolved of Ca^{2+} and K^{+} in the natural FEBEX bentonite test are smaller than in the test with pre-treated bentonite. Brucite and gypsum dissolution/precipitation is slightly sensitive to the change in the composition of the exchange complex.

8.6. Conclusions

A coupled THCM model of the mortar-bentonite interactions of the double interface tests has been presented.

The model reproduce the measured water intake, water content and the dry density at the end of the test. The mode predicts the portlandite dissolution in the mortar and calcite, brucite, CSH1.2 and CSH1.6 precipitation in the mortar and in the bentonite near the interface. Anhydrite precipitates in the mortar, but it is transformed into gypsum after the cooling phase. The model predicts a small precipitation of ettringite and quartz and no cristobalite dissolution. The porosity decreasing is maximum (1.5%) in the bentonite in a 0.2 mm thick zone near the mortar interface due to calcite and brucite precipitation. The pH front (pH>8) penetrates into bentonite 10 mm at the end of the test.

For the most part, the numerical model captures the main trends of the observed mineral dissolution/precipitation patterns. However, there are some discrepancies, especially for ettringite precipitation in the mortar which is not computed with the model, and brucite precipitation in the bentonite which was not observed in the laboratory. Some of these discrepancies could be due to the limitations of the model which does not account for CASH phases because there are no thermodynamic data for such CASH phases.

The results of the sensitivity run to the initial composition of the exchange complex show that: 1) Cation exchange reactions in the test containing natural FEBEX bentonite are enhanced compared to the test of pre-treated FEBEX bentonite; 2) The concentrations of dissolved of Mg^{2+} and Na^{+} in the test containing natural FEBEX bentonite are larger than those of the test with pre-treated FEBEX bentonite while the concentrations of dissolved of Ca^{2+} and K^{+} in the test with the natural FEBEX bentonite are smaller than in the test with pre-treated bentonite; and 3) Brucite and gypsum dissolution/precipitation is slightly sensitive to the change in the composition of the exchange complex.

Chapter 9. THCM models of the FEBEX *mock-up* and *in situ* test

9.1. Introduction

FEBEX (Full-scale Engineered Barrier Experiment) is a demonstration and research project for the engineered barrier of a high-level radioactive waste repository. FEBEX is based on the Spanish reference concept for radioactive waste disposal in crystalline rock. The canisters are emplaced in horizontal drifts and surrounded by a compacted bentonite clay barrier made of a Spanish bentonite from Cortijo de Archidona which is known as FEBEX bentonite. The project included two main large-scale tests: the FEBEX *in situ* full-scale test performed at Grimsel, Switzerland, and the FEBEX *mock-up* test operating at the CIEMAT facilities in Madrid, Spain (ENRESA, 2006a; 2006b). Both tests started in February 1997.

Coupled 1-D axisymmetric thermo-hydro-chemical and mechanical (THCM) models of the FEBEX tests were developed within the FEBEX Project based on laboratory tests, online data from the FEBEX *mock-up* test and on line and partial dismantling data from the FEBEX *in situ* test (Zheng et al., 2011).

This chapter presents the models of the FEBEX *mock-up* and *in situ* tests. The chapter starts with the testing of the previous 1-D THCM model of the *mock-up* test reported by Zheng and Samper (2008) with the most recent water intake and relative humidity data. Then, the models of the FEBEX *in situ* tests are presented, including:

- The testing and updating of the previous THCM model of the FEBEX *in situ* test reported by Zheng et al. (2011). The detailed account of the contributions in this task can be found in Appendix 7.
- The updated geochemical predictions of the bentonite barrier in hot and cold sections at the dismantling of heater 2 of the *in situ* test in 2015. The details of this contribution can be found in Appendix 8.
- The model predictions of the tracer migration. The details of these predictions are presented in Appendix 9.

- The predictions of the geochemical interactions of the bentonite with the concrete plug. The details of these predictions can be found in Appendix 10.

9.2. Model testing with data from the FEBEX *mock-up* test

The *mock-up* test replicates at almost full-scale the Spanish reference concept for radioactive waste disposal in granite (ENRESA, 2005). The components of the *mock-up* test include: two electric heaters, a 0.64 m-thick clay barrier, instrumentation, automatic control of heaters, and a data acquisition system. The bentonite buffer in the *mock-up* test is confined in a steel structure which ensures a uniform temperature and water pressure around the external surface of the buffer. Heating and hydration of the clay buffer started in February 1997 and has continued uninterruptedly at the CIEMAT facilities in Madrid (Martín and Barcala, 2005; Martín et al., 2006).

A THC model of the FEBEX *mock-up* test was performed within the FEBEX project (see Zheng and Samper, 2008). This model was constructed with data from t = 0 until t = 3,000 days. In this dissertation, this model has been tested with data collected from t = 3,000 days to t = 5,000 days. The computed cumulative water intake reproduces the measured water intake data (Figure 9.1). Some deviations are observed at t = 5,000 days. The computed volume is smaller than the measured volume. The computed relative humidities reproduce the measured data at 0.22 m (Figure 9.2) until 1,500 days. However, the computed relative humidities are smaller than the measured data after 1,500 days. Measured data at 5,000 days are 10% larger than computed humidities at the sensors located 0.37 m from the heater (Figure 9.3). The computed relative humidities fit well the measured data at a distance of 0.55 m (Figure 9.4). The computed relative humidities are slightly larger than the measured data at 0.70 m from the heater (Figure 9.5). In summary, the computed relative humidities reproduce the measured data at the external sensors, but underestimate the measured data after 1,500 days at the internal sensors. A double porosity model could overcome these discrepancies.

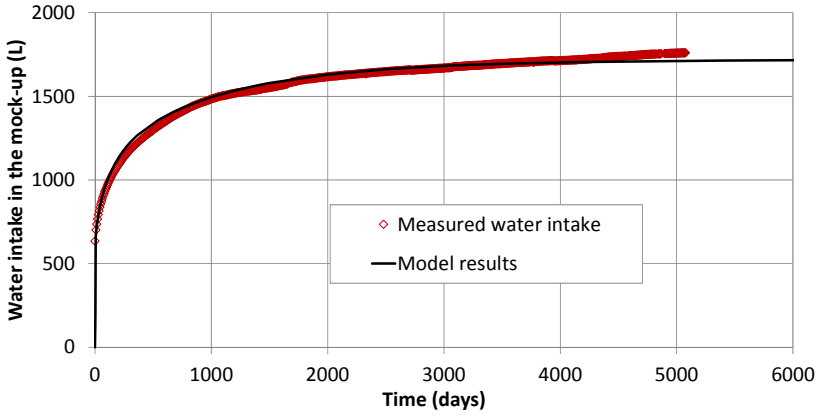

Figure 9.1. Computed (line) and measured (symbols) water intake for the FEBEX *mock-up* test.

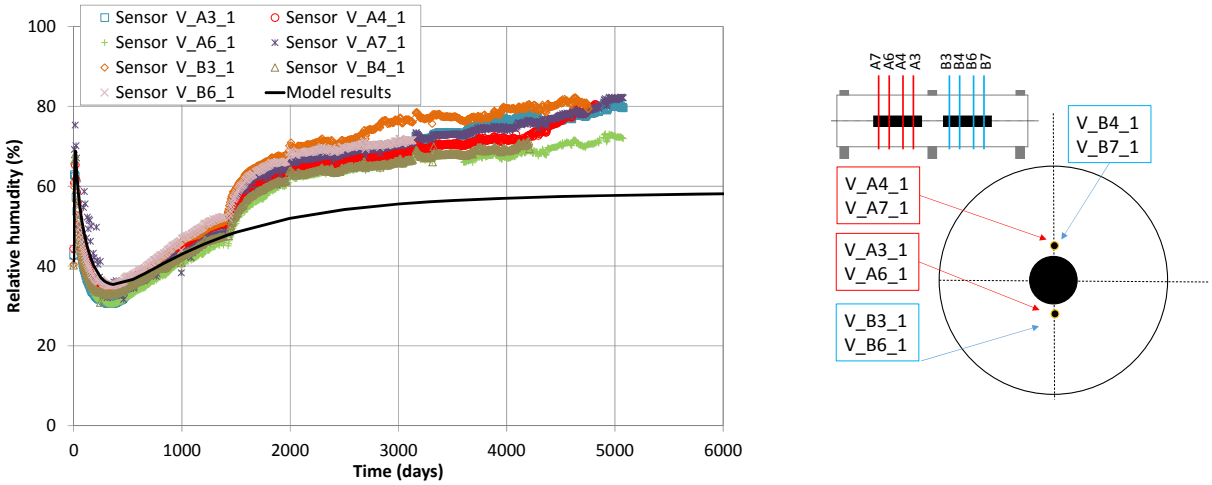

Figure 9.2. Computed (line) and measured (symbols) relative humidity in the sensors located at 0.22 m from the heater for the FEBEX *mock-up* test.

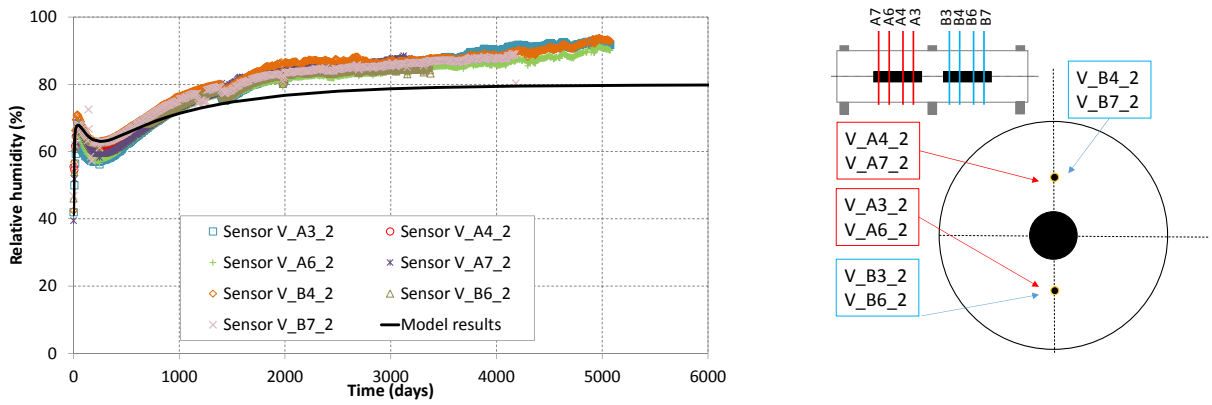

Figure 9.3. Computed (lines) and measured (symbols) relative humidity in the sensors located at 0.37 m from the heater for the FEBEX *mock-up* test.

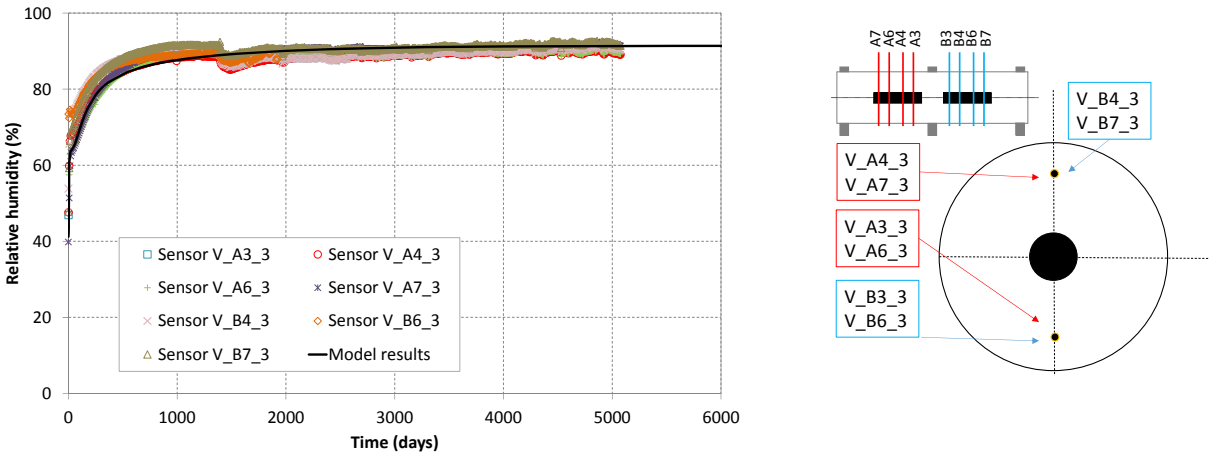

Figure 9.4. Computed (lines) and measured (symbols) relative humidity in the sensors located at 0.55 m from the heater for the FEBEX *mock-up* test.

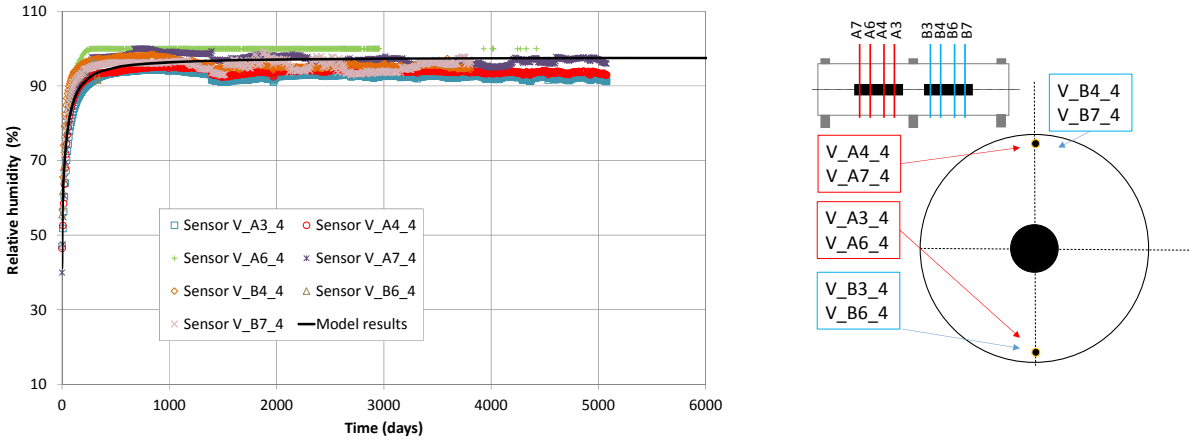

Figure 9.5. Computed (lines) and measured (symbols) relative humidity in the sensors located at 0.70 m from the heater for the FEBEX *mock-up* test.

9.3. THCM models of the FEBEX *in situ* test

9.3.1. Introduction

The previous THCM model of the FEBEX *in situ* tests has been updated and improved in this dissertation. The following activities were performed:

- Reviewing and analysing some aspects of the previous 1-D THCM model of the FEBEX *in situ* test such as: 1) Extending the 1-D axisymmetric THCM model to 2-D axisymmetric conditions; 2) Quantifying the sensitivity of the chemical predictions to the uncertainties in the retention curve of the bentonite, the vapor tortuosity, the dissolution

of smectite, and the changes in the boundary conditions caused by the cooling and the dismantling of the test; and 3) Studying the back diffusion of solutes from the bentonite into the granite.

- Updating the previous 1-D axisymmetric THCM model of the FEBEX *in situ* test by: 1) Improving the boundary condition at the heater-bentonite interface; 2) Refining the spatial discretization of the finite element mesh; and 3) Revising the dispersivities of the bentonite and the granite.
- Comparing the updated model with on line temperature, relative humidity, water content, and pore water pressure in the granitic rock data collected from 2002 to 2015, with gravimetric water content data measured after the dismantling of heater 1 in 2002, and with chemical data collected after the dismantling of heater 1.
- Performing pre-dismantling THCM model predictions of the geochemical conditions for the hot and cold sections after the dismantling of heater 2 in 2015.
- Updating the predictions of the tracer migration.
- Performing pre-dismantling predictions of the geochemical interactions of the bentonite barrier with the concrete plug.

9.3.2. Testing and updating of the THCM model of the FEBEX in situ test

Several sensitivity runs were performed with the previous THCM model. The results of the sensitivity runs show that the computed concentrations of dissolved species in a hot section in 2002 are sensitive to an increase in the parameter α of the van Genuchten retention curve of the bentonite. The increase in α leads to larger water evaporation rates and larger solute concentrations near the heater. The pH and the concentration of HCO_3^- are not sensitive to the change in α. The computed concentrations of most species in the cold section, however, lack sensitivity to the change in α.

The computed concentrations are not sensitive to smectite dissolution and analcime precipitation because the cumulative dissolution of smectite and precipitation of analcime in 2002 is very small. The computed concentrations in 2002 are not sensitive to the change in the boundary condition of the gas during the dismantling stage. On the other hand, the computed concentrations are sensitive to the cooling because the solubility of the minerals and the chemical parameters depend on temperature.

The computed concentrations of dissolved Ca^{2+}, K^+, Mg^{2+}, Na^+ and Cl^- near the heater in 2002 increase when the vapor tortuosity increases. However, the concentrations away from the heater decrease when the vapor tortuosity increases. The computed pH and the

concentrations of dissolved SO_4^{2-} and HCO_3^- are less sensitive to the changes in the vapor tortuosity.

Solute diffusion from the bentonite into the granite is very sensitive to the effective diffusion coefficients of the bentonite and the granite. The effective diffusion, D_e, in the granite used in the previous model was too small. The computed concentrations of Cl^-, SO_4^{2-}, Na^+ and Ca^{2+} in the granite with $D_e = 10^{-12}$ m^2/s (in the granite) and $D_e = 1.4 \cdot 10^{-10}$ m^2/s (in the bentonite) are consistent with the Cl^-, SO_4^{2-}, Na^+ and Ca^{2+} concentrations measured by Buil et al (2010) in a borehole parallel to FEBEX galleries.

The 1-D axisymmetric THCM model of the FEBEX *in situ* test has been extended to 2-D axisymmetric conditions. The temperatures computed with the 2-D model in a hot section are smaller than those calculated with the 1-D model. The temperatures computed with the 2-D model in a cold section are larger than those calculated with the 1-D model. The temperatures computed with the 1-D model fit the measured data better than the temperatures calculated with the 2-D model. The volumetric water contents computed with the 1-D model are larger than the water contents calculated with the 2-D model at all radial distances. The volumetric water contents computed with the 1-D model fit the measured data better than the volumetric water contents calculated with the 2-D model. The 1-D axisymmetric model outperforms the 2-D axisymmetric model because the model parameters used to perform the comparison of both models are the parameters calibrated with the 1-D axisymmetric model. A detailed calibration of the parameters of the 2-D axisymmetric model probably will lead to model results at least as good as or better than the results of the 1-D axisymmetric model.

The concentrations of Cl^- in 2002 computed with the 2-D model are large near the heaters 1 and 2. The largest concentrations are located at the edge of heater 2. The contour lines are approximately parallel to the axis of the gallery along heaters 1 and 2. In the edges of the heaters, however, the contour lines are not parallel to the gallery axis. The computed contour plots of Cl^- concentrations illustrate that the edge effects extend approximately over a distance of 0.5 to 1 m. The concentrations of Cl^- in 2015 show a significant decrease compared to the concentrations in 2002 around heater 2. Large concentrations of Cl^- still remain in the bentonite barrier between the dummy and heater 2 and between heater 2 and the end of the gallery.

The previous 1-D axisymmetric THCM model of the FEBEX *in situ* test reported by Zheng et al. (2011) has been updated by: 1) Improving the boundary condition at the heater-bentonite interface; 2) Refining the spatial discretization of the finite element mesh; and 3) Modifying the solute dispersivities of the bentonite and the granite. The revised

implementation of the boundary condition leads to more water evaporation than the previous model. The computed concentrations of Ca^{2+}, K^{+}, Mg^{2+}, Cl^{-} and Na^{+} near the heater with the updated model are significantly larger than the concentrations calculated with the previous model. The computed pH and the concentrations of SO_4^{2-} and HCO_3^{-} with the updated model are similar to those of the previous model.

The improvement in the boundary condition at the heater-bentonite interface leads to a significant decrease of the mass balance error. The mass balance errors in the model of the cold section are generally smaller than 10%. The mass balance errors of the updated model are deemed acceptable.

The computed concentrations of Ca^{2+}, K^{+}, Mg^{2+}, Na^{+} and HCO_3^{-} become smoother when the diffusion coefficients of the bentonite are increased by a factor of 10. The profiles of Cl^{-} and SO_4^{2-} are less sensitive to the change in the diffusion coefficient because the diffusion coefficients of these species are smaller than the diffusion coefficients of the rest of the species. The computed pH is not sensitive to the change in the diffusion coefficients.

The updated 1-D axisymmetric THCM model of the FEBEX *in situ* test has been tested with gravimetric water content and dry density measured data at the dismantling of heater 1 in 2002 and heater 2 in 2015 and on line temperature, relative humidity, water content and pore water pressure in the granitic rock data collected from 2002 to 2015. The comparison of the computed values with the measured data leads to the following conclusions:

- The numerical model reproduces the main trends of the measured temperature data. The computed temperatures near the bentonite-granite interface in hot sections are smaller than the measured temperatures during the first 2,000 days and larger than the measured temperatures after 2,000 days. The computed temperature in 2015 is 3ºC larger than the measured temperature at the bentonite-granite interface.
- The computed relative humidities reproduce the general trends of the measured relative humidity data.
- The computed time evolution of the water contents in a hot section reproduce the time evolution of the measured TDR water content data, except at r = 0.59 m. The best fit of computed values to measured data is achieved at r = 1.04 m, especially at the sensor on the right side of the tunnel.
- The computed pore water pressures at the granitic rock are smaller than the measured values due to the heterogeneities of the granitic rock, which are not taken into account in the model and the uncertainty in the prescribed pore water pressure at the external boundary.

- The predicted water contents in a hot section and a cold section at the times of dismantling of heater 1 (in 2002) and heater 2 (in 2015) are within the band of measured data and match the general trend of the measured data (see Figure 9.6).
- The predicted dry density in a cold and hot section times of dismantling of heater 1 (in 2002) and heater 2 (in 2015) are for the most part within the band of measured data. There are some discrepancies in the hot and cold sections in 2002. The computed dry density overestimates the measured dry density near the heater (0.7 m < r < 1 m). This discrepancy is not observed in 2015.

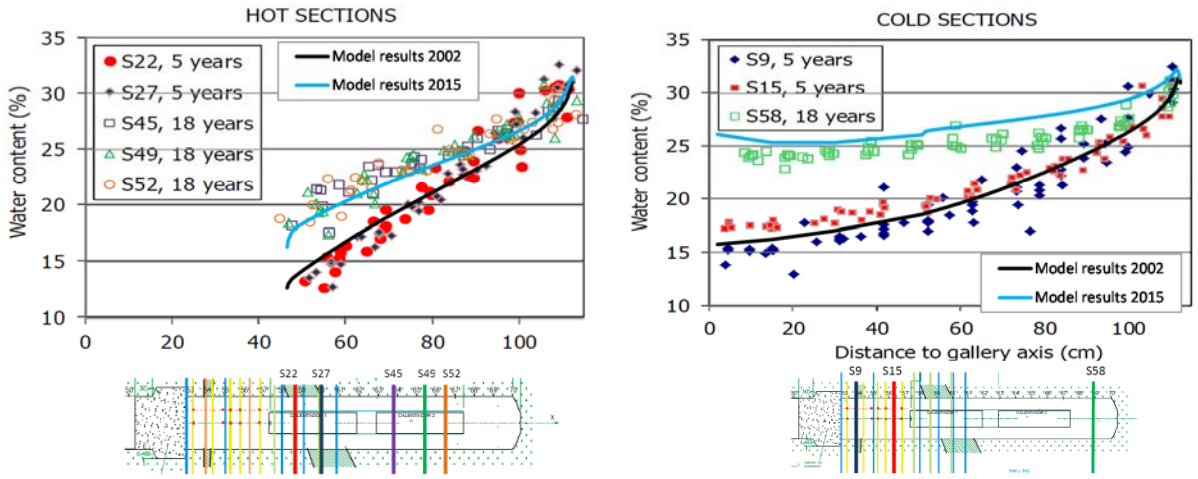

Figure 9.6. Comparison of the predicted gravimetric water content (lines) in a hot section (left) and a cold section (right) and the measured gravimetric water content data (symbols) in sections S22, S27, S45, S49, S52, S9, S15 and S58 at the times of dismantling of heater 1 (year 2002) and heater 2 (year 2015). The plots at the bottom show the location of the sections where water contents were measured.

9.3.3. Pre-dismantling THCM model predictions of the geochemical conditions of the FEBEX in situ test

Pre-dismantling THCM model predictions of the geochemical conditions for the hot and cold sections in June 2015 have been performed with the updated 1-D axisymmetric THCM model (see the details in Appendix 8). Prediction uncertainties have been quantified by sensitivity runs to the diffusion coefficients of the chemical species.

The predicted concentrations of Cl^- in a hot section in 2015 are largest near the heater due to the evaporation of the bentonite pore water and smallest at the granite-bentonite interface due to the hydration of the buffer with granite pore water, which has a concentration smaller than that of the bentonite. The predicted concentrations of Cl^- in 2015 are much smaller than the concentrations in 2002 (Figure 9.7). The predicted concentrations of dissolved cations (Ca^{2+}, Mg^{2+}, Na^+ and K^+) in a hot section are also large near the heater (Figure 9.7). Moreover,

the predicted concentration of SO_4^{2-} in a hot section in 2015 increases near the heater and decreases in the rest of the bentonite barrier. The computed HCO_3^- near the bentonite-granite interface in a hot section is large because the hydration of bentonite with granite water induces the dissolution of calcite at the bentonite-granite interface. The predicted pH in the bentonite near the heater in a hot section in 2015 is 7.5 and decreases slightly towards the granite interface.

The predicted concentration of Cl^- in a cold section in 2015 shows a diffusion profile with low concentration in the bentonite near the granite interface and a concentration of about 0.16 mol/L in the center of the bentonite barrier (Figure 9.8). The predicted concentrations of dissolved cations (Ca^{2+}, Mg^{2+}, Na^+, K^+ and SO_4^{2-}) show diffusion profiles similar to the profile of the concentration of Cl^- (Figure 9.8). The predicted concentration of HCO_3^- in the bentonite near the granite interface in 2015 is 10^{-2} mol/L and decreases to 10^{-3} mol/L at the center of the barrier. The predicted pH in the bentonite remains stable around 7.5.

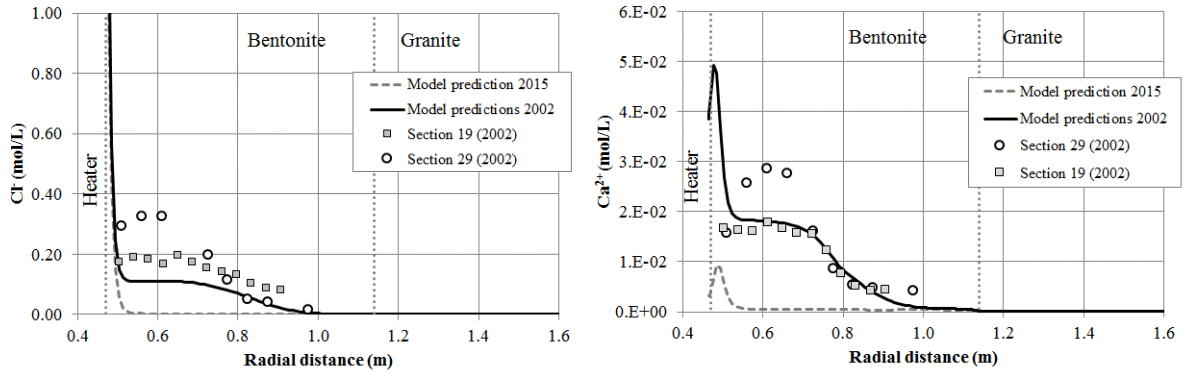

Figure 9.7. Pre-dismantling predictions of Cl^- and Ca^{2+} concentrations (lines) in 2002 and 2015 in a hot section. The graph also shows the inferred Cl^- concentrations in sections 19 and 29 in 2002 (symbols).

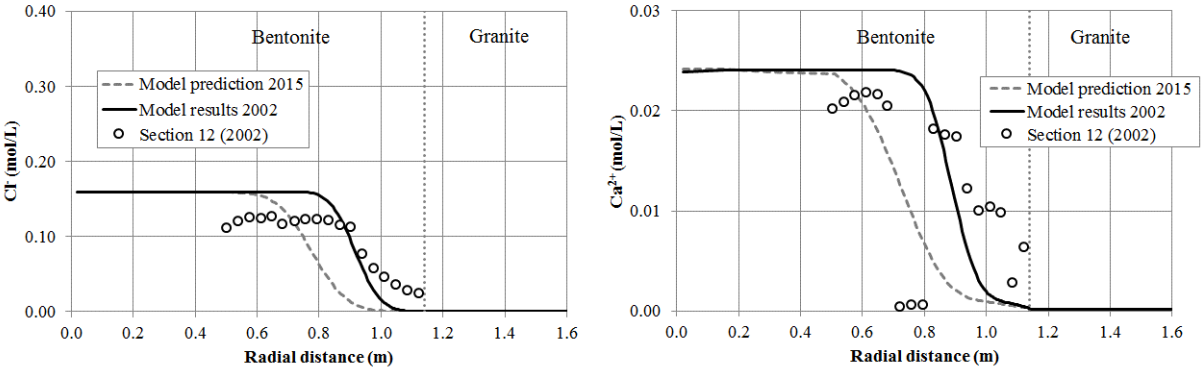

Figure 9.8. Pre-dismantling predictions of Cl^- and Ca^{2+}concentrations (lines) in 2002 and 2015 in a cold section. The graph also shows the inferred Cl^- concentrations in section 12 in 2002 (symbols).

The predicted concentrations in the hot sections are very sensitive to an increase of the diffusion coefficients by a factor of 10. In general, the profiles of the concentrations of most of the chemical species become smoother when the diffusion coefficient is increased. The concentrations decrease near the heater and increase in the rest of the bentonite barrier. The concentration of dissolved Ca^{2+} increases everywhere in the bentonite because calcite dissolution near the heater is enhanced when the diffusion coefficients of the bentonite are multiplied by 10. Such increase in the concentration is Ca^{2+} is accompanied by a decrease in the concentration of dissolved HCO_3^-.

The predicted radial profiles of the concentrations of Ca^{2+}, K^+, Mg^{2+}, Na^+ and HCO_3^- in the cold sections become smoother when the diffusion coefficients are increased. The profiles of Cl^- and SO_4^{2-} are also sensitive to the change in the diffusion coefficients. Their sensitivity, however, is much smaller than the sensitivity of other species because the diffusion coefficients of Cl^- and SO_4^{2-} are much smaller than the diffusion coefficients of the rest of the species. The predicted pH is slightly sensitive to the change in the diffusion coefficients.

9.3.4. Predictions of the tracers migration in the FEBEX in situ test

Updated predictions of the tracer migration have been performed for: 1) Iodide along several radii in sections 37, 50 and 51 (hot sections) by using a 1-D axisymmetric model; 2) Borate, europium, perrhenate and selenate at the inner blocks of section 46 (hot sections) by using 2-D models in vertical planes; and 3) Caesium and borate at the outer blocks of section 48 (hot sections) by using 2-D models in vertical planes. The details of the tracer predictions are presented in Appendix 9.

The predictions of the migration of the tracers have been computed with the updated version of the THCM model of the FEBEX *in situ* test. The predictions of tracer migration lead to the following conclusions:

- Large iodide concentrations are predicted near the heater 2. The iodide concentration in section 37 near the heater 1 decreased after the heater was switched off in 2002 due to the increase in water content caused by vapor condensation and bentonite hydration.
- The predicted perrhenate concentrations in 2015 show that this tracer has diffused entirely in the full section.
- The plumes of the point tracers located in the inner blocks are (Figure 9.9):
    - Almost circular with an approximate diameter of 8 cm for borate.
    - Semicircular with an approximate diameter of 20 cm for selenite.
    - Slightly anisotropic with an approximate length of 8 cm for europium.

- The plumes of the point tracers located in the outer blocks are (Figure 9.9):
    - Almost circular with an approximate diameter of 7 cm for cesium.
    - Almost circular with a diameter of 10 cm for borate.

The comparison of the predicted tracer concentrations with the measured values will provide the basis for the testing and partial validation of the current THCM models for compacted bentonites.

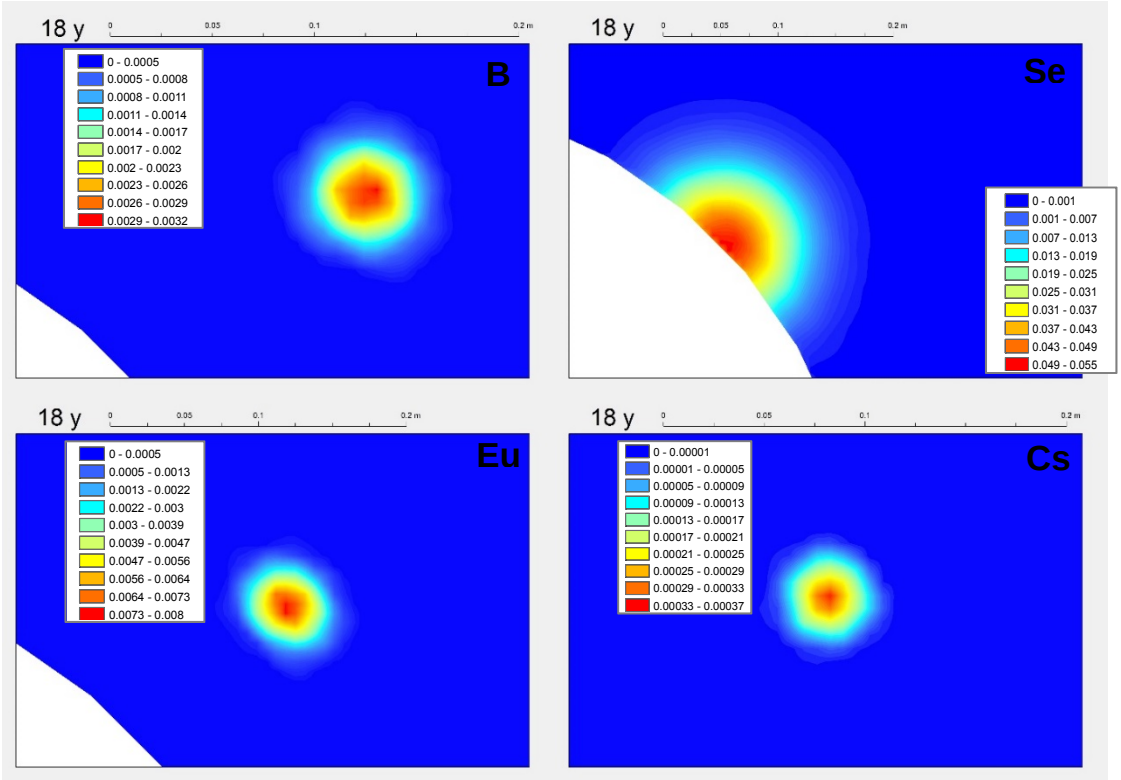

Figure 9.9. Computed concentrations of dissolved borate (top left), selenate (top right), europium (bottom left) and cesium (bottom right) (mol/L) at 18 years with the 2-D numerical model in a vertical plane normal to the axis of the gallery.

9.3.5. Predictions of the interactions of the bentonite with the concrete plug of the FEBEX in situ test

The geochemical interactions of the bentonite and the concrete plug have been modelled with a 1-D non-isothermal variably-saturated water flow and multicomponent reactive transport model along a horizontal line normal to the interface at a radial distance of 0.75 m from the axis of the gallery. The computed temperature in the bentonite in 2015 ranges from 24 ºC in the concrete to 34 ºC in the bentonite. These temperatures compare well with the temperatures measured along a borehole drilled through the concrete plug before switching off the heater 2.

Model predictions show that calcite dissolves in the bentonite and precipitates near the bentonite-concrete interface. The precipitation front propagates into the bentonite. Portlandite dissolves in the concrete interface. Ettringite precipitation is very small and nonuniform. The precipitation of this mineral phase is transient. It redissolves and is present in 2015 only in small amounts. Neither gypsum nor anhydrite precipitate. CSH1.8 dissolves in the concrete near the concrete-bentonite interface while CSH0.8 precipitation in the concrete is extremely small. Brucite precipitates in the bentonite near the interface. The front of brucite precipitation moves from the bentonite-concrete interface into the bentonite. Sepiolite shows a similar precipitation front. The model does not predict the precipitation of the Friedel salt. The porosity decreases slightly in the bentonite near the concrete-bentonite interface due to the precipitation of brucite, calcite and sepiolite. The porosity in the concrete, on the other hand, increases near the interface due mostly to the dissolution of portlandite. The changes in porosity only affect 2 cm in the bentonite and concrete interface in both sides of the interface (Figure 9.10b). The pH increases slightly in the concrete. The high pH front after 13 years penetrates a few cm into the bentonite (Figure 9.10a).

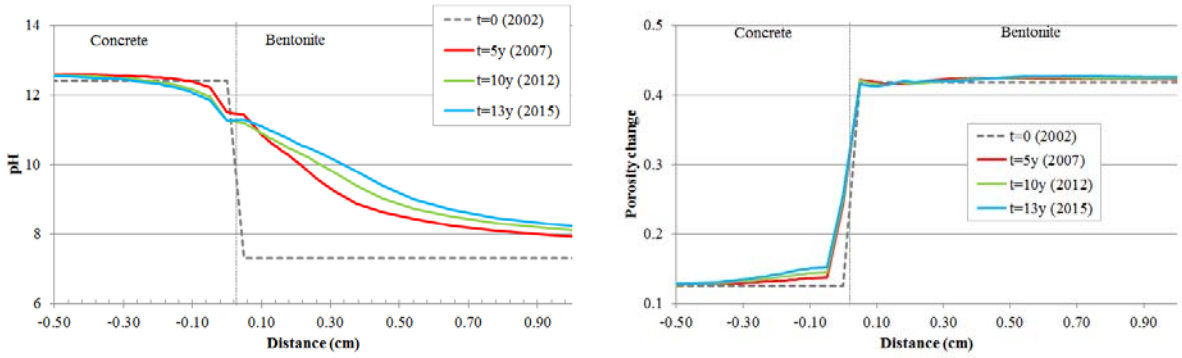

a) *b)*

Figure 9.10. Predicted pH (left) and changes in porosity caused by dissolution/precipitation reactions (right) in the bentonite and the concrete at selected times.

9.4. Conclusions

The THC model of the FEBEX *mock-up* test was tested with data collected from t = 3,000 days to t = 5,000 days. The computed water intake and the relative humidities at the external sensors reproduce the measured data. However, the computed relative humidity underestimates the measured data at the internal sensors after 1,500 days.

The previous 1-D axisymmetric model of the FEBEX *in situ* test has been extended to 2-D axisymmetric conditions. In general, the 1-D model results fit the temperature and water

content measured data better than the 2-D model. A detailed calibration of the parameters of the 2-D axisymmetric model will lead to model results at least as good as or better than the results of the 1-D axisymmetric model. The contour lines of the Cl^- concentration are approximately parallel to the axis of the gallery along heaters 1 and 2, but the edge effects extend approximately over a distance of 0.5 to 1 m.

The previous 1-D THCM model of the FEBEX *in situ* test has been updated by improving the boundary conditions, refining the mesh at the heater-bentonite interface and updating the solute dispersivities in the bentonite and granite. These improvements on the THCM 1-D model lead to an increase in the water evaporation near the heater and larger concentrations near the heater.

The updated 1-D axisymmetric model has been used to compare the model results with the thermal and hydraulic data from 2002 to 2015 and to perform the pre-dismantling geochemical predictions at 2015. The numerical results reproduce the main trends of the temperature, relative humidity, water content and dry density. The predicted concentrations in the hot sections show large concentrations near the heater and small concentrations at the bentonite-granite interface. The predicted concentrations in a hot section in 2015 are smaller than those computed in 2002. The predicted concentrations in a cold section in 2015 show a diffusion front.

Updated predictions of the tracer migration have been performed with the most updated version of the THCM model of the FEBEX *in situ* test. The predictions of tracer migration lead to the following conclusions:

- Large iodide concentrations are predicted near the heater 2. The iodide concentration in section 37 near the heater 1 decreased after the heater was switched off in 2002 due to the increase in water content caused by vapor condensation and bentonite hydration.
- The predicted perrhenate concentrations in 2015 show that this tracer has diffused entirely in the full section.
- The plume of borate in the inner blocks is almost circular with a diameter of 8 cm, the plume of selenite is semicircular with an approximate diameter of 20 cm and the plume of europium is anisotropic with an approximate length of 8 cm.
- The plume of cesium in the outer blocks is almost circular with an approximate diameter of 7 cm and is almost circular with a diameter of 10 cm for borate.

A detailed 1-D non-isothermal variably-saturated water flow and multicomponent reactive transport model normal to the bentonite-concrete interface has been performed to study the geochemical interactions of the bentonite and the concrete plug. Model predictions

show that calcite dissolves in the bentonite and precipitates near the bentonite-concrete interface. The precipitation front propagates into the bentonite. Portlandite dissolves in the concrete interface. Ettringite precipitation is very small and nonuniform. Neither gypsum nor anhydrite precipitate. CSH1.8 dissolves in the concrete near the concrete-bentonite interface while CSH0.8 precipitation in the concrete is extremely small. Brucite precipitates in the bentonite near the interface. The front of brucite precipitation moves from the bentonite-concrete interface into the bentonite. Sepiolite shows a similar precipitation front. The porosity decreases slightly in the bentonite near the concrete-bentonite interface due to the precipitation of brucite, calcite and sepiolite. The porosity in the concrete, on the other hand, increases near the interface due mostly to the dissolution of portlandite. The changes in porosity only affect 2 cm in the bentonite and concrete interface in both sides of the interface. The pH increases slightly in the concrete. The high pH front after 13 years penetrates a few cm into the bentonite.

Chapter 10. Reactive transport modelling of the long-term interactions of corrosion products and compacted bentonite in a HLW repository in granite

10.1. Introduction

Carbon steel and compacted bentonite have been proposed as candidate materials for the overpack and buffer, respectively, in the multi-barrier system of deep geological repositories for high-level radioactive waste (HLW). The corrosion of the carbon steel may induce buffer alterations which could result in changes in parameters such as porosity, permeability, sorption and swelling. The prediction of the long-term evolution of the engineered barrier in a repository should not be a blind extension of the models developed for experiments to different space and time scales. It requires a careful assessment of the key long-term processes and their couplings as well as an evaluation of the resulting uncertainty and its consequences. Contrary to thermal, hydrodynamic and mechanical transient processes which will last for several hundreds to 1,000 years, the geochemical reactions induced by canister corrosion will take place at all temporal scales.

This chapter presents a non-isothermal reactive transport model for the long-term (1 Ma) interactions of the corrosion products and compacted bentonite in a HLW repository in granite. The details can be found in Appendix 11.

10.2. Conceptual and numerical model

The geometry of the model corresponds with the Spanish reference concept of a high-level radioactive waste repository in granite (ENRESA, 2000). It consists on the disposal of spent fuel elements in cylindrical carbon steel canisters placed in horizontal disposal drifts. The disposal drifts, having 500 m in length and 2.4 m in diameter, are located at a depth of 500 m in a granite formation. The canisters are 4.54 m long, 0.10 m thick and have an external diameter of 0.90 m. They are surrounded by blocks of compacted bentonite.

A 1-D axisymmetric numerical model of the canister and the bentonite has been used to simulate the long-term interactions of the corrosion products and the bentonite (Figure 10.1). Water flow and solute transport through the granite was simulated with a constant water flux of 0.1 L/y parallel to the axis of the gallery at the bentonite-granite interface. A constant corrosion rate of 2 μm/year was assumed in the reference run.

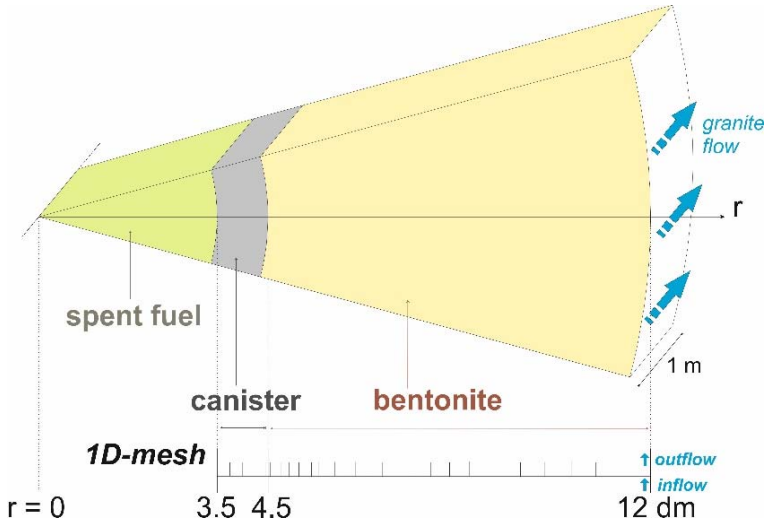

Figure 10.1. Scheme of the engineered barrier system and 1-D finite element grid of the axisymmetric model (Samper et al., 2016).

10.3. Model results

Canister corrosion causes an increase in the pH and the concentration of dissolved Fe^{2+} of the bentonite porewater. Iron precipitates as magnetite and siderite and sorbs via cation exchange and surface complexation on weak sites. The largest pH in the bentonite is almost 9.5 at $2 \cdot 10^5$ years. Several fronts are observed in the concentration of dissolved Fe^{2+}, pH and Eh which are related to sorption fronts. Magnetite is the main corrosion product and its precipitation reduces significantly the porosity of the bentonite barrier near the canister and could even clog the pores (Figure 10.2). The thickness of the bentonite zone affected by the decrease of porosity increases with time and is equal to 7 cm at t = 1 Ma.

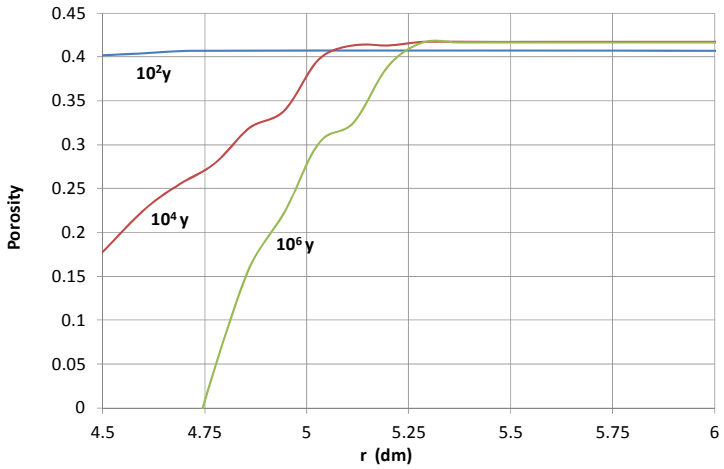

Figure 10.2. Radial distribution of the computed bentonite porosity which changes due to mineral dissolution/precipitation at selected times (Samper et al., 2016).

10.4. Sensitivity analysis

A detailed sensitivity analysis has been performed to changes in model parameters and conceptual model assumptions. The larger the corrosion rate, the larger the magnetite and siderite concentration near the canister-bentonite interface but the smaller their penetration into the bentonite. Therefore, the larger the corrosion rate, the faster the porosity reduction near the canister but the smaller the thickness of affected bentonite. This thickness ranges from < 5 cm for a corrosion rate of 5 μm/year to nearly 12 cm for 0.5 μm/year. The larger the effective diffusion, D_e, the larger the thickness of the bentonite where magnetite, siderite and calcite precipitate and the thicker the bentonite affected by pore clogging. This thickness varies from 4 to 10 cm in the considered range of the D_e. The bentonite thickness affected by the porosity reduction decreases when the ground water flow through the granite, Q, increases. Such thickness decreases from 7 cm to 3 cm when Q increases by a factor of 10. The changes in the bentonite cation exchange selectivities do not affect the computed pH, Eh and the concentrations of other dissolved and precipitated species. The computed magnetite concentration near the canister-bentonite interface is sensitive to changes in the initial chemical composition of the bentonite porewater. The thickness of altered bentonite is doubled when the dependence of the corrosion rate on the chemical conditions is considered. The thermal transient and the effect of temperature on the corrosion rate do not have a very significant influence on the geochemical evolution of the bentonite barrier. The thickness of altered bentonite decreases when kinetic magnetite precipitation is considered. Such thickness decreases 3 cm when smectite dissolution and analcime precipitation are taken into account.

However, it is similar to that of the reference run when cronstedtite is considered besides smectite dissolution and analcime precipitation.

10.5. Conclusions

A non-isothermal reactive transport model of the long-term interactions of the corrosion products and compacted bentonite in a HLW repository in granite has been presented.

Canister corrosion causes an increase in the pH and the concentration of dissolved Fe^{2+} of the bentonite pore water. The largest pH in the bentonite is almost 9.5 at $2 \cdot 10^5$ years. Magnetite is the main corrosion product and its precipitation reduces significantly the porosity of the bentonite barrier near the canister and could even clog the pores. The thickness of the bentonite affected by the decrease of porosity increases with time and is equal to 7 cm at t = 1 Ma. This thickness is doubled when the dependence of the corrosion rate on the chemical conditions is considered and reduces 3 cm when smectite dissolution and analcime precipitation are taken into account. Model results are not sensitive to the thermal transient and the effect of temperature on the corrosion rate.

The conclusions of the simulations are consistent for the most part with those reported by others for bentonite barriers. However, there are differences in the geochemical systems and the hypotheses used by Savage et al. (2010a).

Chapter 11. Long-term non-isothermal reactive transport model of compacted bentonite, concrete and corrosion products in a HLW repository in clay

11.1. Introduction

Carbon steel and compacted bentonite have been proposed as candidate materials for the overpack and buffer, respectively, in the multi-barrier system of deep geological repositories for high-level radioactive waste (HLW). A concrete liner is required in tunnels excavated in clay host rock. The addition of a concrete liner takes place as a support layer in clay formations. Concrete and cement are used for mechanical support in shotcrete, tunnel seals and plugs.

The corrosion of the carbon steel and the concrete degradation may induce bentonite alterations which could result in changes in parameters such as porosity, permeability, sorption and swelling. The interaction of cementitious materials with the clay host rock produces a hyper-alkaline fluid ($10 < pH < 13.5$) which can interact with the initially unsaturated bentonite surrounding the carbon steel canister (Yang et al., 2008). The physical and chemical properties of the bentonite and the clay host rock could be affected by this hyper-alkaline fluid. This interaction could produce high pH in the bentonite and in the clay, cause mineral dissolution and precipitation of secondary minerals, and reduce the porosities of the bentonite buffer and the host rock.

This chapter presents a non-isothermal reactive transport model to quantify the long-term interactions of the corrosion products, concrete degradation, clay and bentonite in a HLW repository in clay. The details of the model can be found in Appendix 12.

11.2. Conceptual and numerical model

The model corresponds to a radioactive waste repository in clay according to the Spanish Reference Concept (ENRESA, 2004). Cylindrical carbon steel canisters with 0.9 m diameter are emplaced in horizontal galleries and embedded into a 0.75 m thick bentonite buffer. A 0.3 m thick concrete sustainment is located between the bentonite buffer and the clay formation.

The non-isothermal multicomponent reactive transport model aims at studying the long-term geochemical interactions of compacted bentonite with the concrete liner and the corrosion products in a HLW repository in a clay formation for 1 Ma. This non-isothermal reactive transport extends the scope of the model of Yang et al. (2008) by accounting simultaneously for canister corrosion and concrete degradation and incorporating additionally: 1) Surface complexation on three types of sorption sites; 2) Iron sorption by surface complexation; 3) Kinetic smectite dissolution; and 4) Precipitation of secondary clay minerals.

A 1-D axisymmetric numerical model has been used to simulate the long-term geochemical interactions of compacted bentonite with concrete and corrosion products in a HLW repository in a clay formation with a total length of 25 m (Figure 11.1). The model accounts for the canister, the bentonite, the concrete and the clay host rock. A constant corrosion rate of 2 μm/year was assumed.

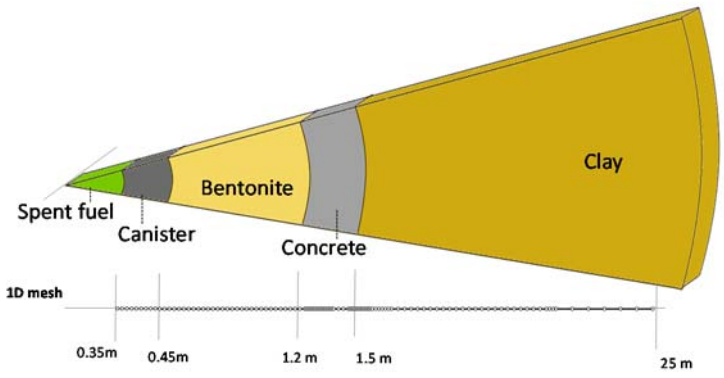

Figure 11.1. 1-D finite element grid which accounts for the canister, the bentonite barrier, the concrete liner and the clay formation (Mon et al., 2017).

11.3. Model results

Model results show that magnetite is the main corrosion similar to the model results of the long-term model in granite (see Appendix 11). Its precipitation reduces the bentonite porosity near the canister. Concrete degradation leads to the precipitation of secondary minerals and the reduction of the porosity of the bentonite and the clay formation at their interfaces with the concrete liner. The decrease of the porosities is especially important for $t > 10^4$ years. The zones affected by pore clogging at the canister-bentonite, and concrete-clay interfaces at 1 Ma are equal to 1, and 3.3 cm thick, respectively (see Figure 11.2). The pH in the bentonite after 1 Ma is uniform and equal to 9.42. At that time, the hyperalkaline front (pH > 8.5) migrates 2.5 cm into the clay formation.

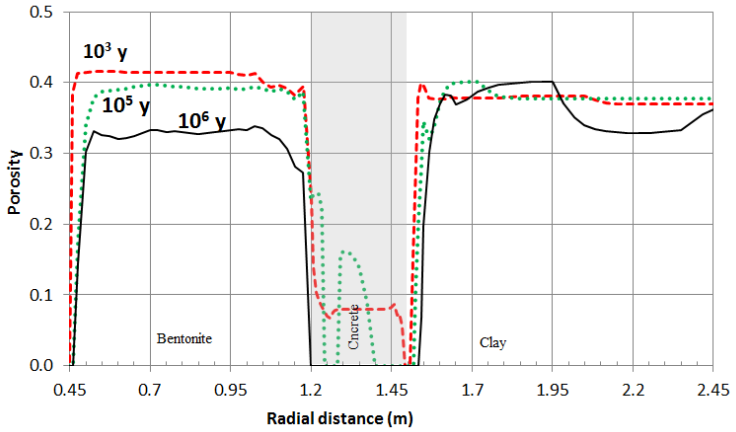

Figure 11.2. Radial distribution of the computed porosity which changes due to mineral dissolution/precipitation at selected times.

11.4. Sensitivity analysis

Sensitivity runs were performed to analyse the uncertainties in cation exchange selectivities and evaluate the relevance of surface complexation reactions, kinetic smectite dissolution, and Mg-saponite precipitation. Only the concentrations of the exchanged Ca^{2+}, Mg^{2+}, Na^{+} and K^{+} are sensitive to changes in the selectivity coefficients. The computed pH at t = 1 Ma in the sensitivity run without surface complexation reactions is the same as that of the base run.

Accounting for smectite dissolution leads to: 1) Slight changes in the computed pH in the bentonite at t = 1 Ma; 2) A reduction in the breakthrough of the pH front into the clay formation from 35 to 15 cm; 3) An increase in brucite precipitation in the bentonite near the

concrete interface and in the concrete; and 4) A decrease of gypsum precipitation. The run with Mg-saponite precipitation in the bentonite leads to slightly larger pH, slightly smaller magnetite precipitation and smaller smectite dissolution at t = 1 Ma.

11.5. Conclusions

A non-isothermal reactive transport model of the interactions of the compacted bentonite with the corrosion products of a carbon-steel canister and the concrete liner in a HLW in clay has been presented

Canister corrosion and concrete degradation cause an increase in the pH. The largest pH in the bentonite is 9.4 at 10^6 years. Magnetite is the main corrosion product and its precipitation reduces significantly the porosity of the bentonite barrier near the canister and could even clog the pores. In addition, the concrete degradation in the repository in clay leads to the precipitation of secondary minerals and the reduction of the porosity of the bentonite and the clay formation at their interfaces with the concrete liner. The decrease of the porosity is especially important for $t > 10^4$ years. The thickness of the zones affected by pore clogging at the canister-bentonite, and concrete-clay interfaces at 1Ma are equal to 1, and 3.3 cm, respectively.

The results show similarities with the results of the models reported by others for engineered barrier systems at similar chemical conditions, including: 1) Pore clogging at the canister-bentonite and concrete-clay interfaces; 2) Narrow alteration zones; and 3) Limited smectite dissolution after 1 Ma.

Chapter 12. Conclusions and future work

12.1. Improvements in the THCM model and the THCM code

The numerical simulations performed in this dissertation have been performed with the coupled THCM code INVERSE-FADES-CORE. The code has been updated and reviewed to debug programming errors, improve the input and output files and facilitate its use.

Reactive gas transport has been implemented in INVERSE-FADES-CORE V2 by including additional mass balance equations for the reactive gaseous species in the gaseous phase. The implementation of the reactive gas transport has been verified by comparing the numerical results of INVERSE-FADES-CORE V2 with the results computed with TOUGHREACT (Xu et al., 2008) with four test cases.

In addition, INVERSE-FADES-CORE V2 has been benchmarked with other codes for the following two benchmarking problems: 1) Modeling the chemical interactions of the concrete liner with the compacted bentonite of the engineered barrier and the host clay rock; and 2) Modelling the carbonation of concrete in unsaturated conditions during the operational period of a repository.

12.2. Integrated analysis of thermal, hydrodynamic and chemical data of compacted FEBEX bentonite

Green-Ampt analytical solutions have been derived and used to compare radial and parallel flow through the bentonite. The comparison shows that the analytical solutions are markedly different. Such analysis shows that the best fit to compare radial and parallel flow is obtained by optimizing the parameters, especially the volume and the hydration surface. This should be taken into account when translating the results obtained in the tests, where the conditions are parallel, to radial flow conditions.

The integrated analysis of the cumulative water intake data shows an overall consistency. The largest differences occur at early times due to the differences in the

experimental conditions, which decrease with time. Hydration data from most of the tests converge for dimensionless time larger than 0.04.

Water content data of the *mock-up* test are larger than those of the CT cells. The slope of the water content data are similar for the CG cell, and the *in situ* and *mock-up* tests for dimensionless times larger than 0.04.

The slope of the dimensionless temperature is about 0.8 in most of the tests. The integrated analysis of Cl^- shows that the general behavior is similar in most tests, except for the CT23 cell data. The pH data are consistent except for the CT cell.

The general THCM processes in the CT and CG cells, the *mock-up* and the *in situ* tests are similar. The general behavior of the cumulative water intake, water content, temperature and chemical concentration data are also similar in these tests. However, some differences have been found in the integrated analysis of the data which are caused by differences in the size, geometry and initial and boundary conditions in the tests.

The integrated analysis of measured THC data has shown that the data with different space-time scales from lab cell and column tests and the *mock-up* and *in situ* tests cannot be scaled up. The conclusions obtained from this integrated analysis are similar to those reported by Villar el at. (2012).

The dimensional analysis of hydrodynamic, thermal and chemical data assume that the density, the porosity and the hydraulic conductivity of the bentonite are constant. However, these parameters change during the tests (Villar et al., 2008b). The integrated analysis could be improved by: 1) Extending the Green-Ampt solution to account for water distribution, 2) Developing analytical solutions for temperature and concentration, and 3) Performing the integrated analysis of chemical data for reactive species.

The dimensional analysis has been useful to identify the role of experimental conditions, but it failed to provide a framework to integrate all the experimental data. Such integration is most likely to be achieved by means of coupled THCM numerical models. Coupled THCM numerical models constructed with data from lab tests and the *mock-up* and the *in situ* tests can be used for long-term predictions.

12.3. Coupled THCM models of laboratory test

A coupled THCM model of the heating and hydration tests performed on 60 cm long cells has been presented. The model has been performed in two stages. Model results in the testing stage were compared to measured data. The comparison of the model results and the measured data shows the following discrepancies: 1) The computed porosity is smaller than the measured data; 2) The computed water content and saturation degree are larger than the measured data near the heater; 3) The computed temperatures are larger than the measured data in the sensors; 4) The computed water intake overestimates the measurements; 5) The computed concentrations for the CG7.6 test are smaller than the concentrations of the geochemical model of Fernández and Villar (2010); and 6) The concentration of the exchanged Ca^{2+} and Mg^{2+} do not fit the data. The following improvements were performed in the calibration stage: 1) Adjusting the vapor tortuosity; 2) Considering lateral heat dissipation at the sensors; 3) Adjusting the selectivity coefficients; and 4) Updating the material properties at the boundary elements. The revised THCM model reproduces the observed temperatures, saturation degrees, porosities. Moreover, model results fit the measured concentrations of the Cl^- and measured exchanged cations data for the CG0.5, CG1, CG2 tests. The computed concentrations of Cl^-, Na^+, Ca^{2+}, Mg^{2+}, K^+, HCO_3^-, SO_4^{2-} and pH reproduce the general trends of the results reported by Fernández and Villar (2010) for the CG7.6 test.

The corrosion tests carried out by CIEMAT have been modelled with coupled THCM models. The corrosion experiments include: 1) The small corrosion cells with a length of 25 mm and a duration of 180 days; and 2) The medium-size corrosion cells (10 cm long) with a duration of 1593 days. The thermo-hydrodynamic model results fit the general trends of the measured data in the bentonite in both corrosion tests. There are some discrepancies in the computed time evolution of the temperature and relative humidity of the medium-size cells which could be attributed to problems in the water injection system during the tests and vapor leakage through the sensors.

The model results for the small corrosion cells indicate that: 1) Magnetite and $Fe(OH)_2(s)$ are the main corrosion products which compete for Fe^{2+} precipitation; 2) The corrosion products penetrate a few mm into the bentonite; 3) The numerical results fit the measured iron weight data; 4) Fe^{2+} sorbes by surface complexation; and 5) Fe^{2+} exchange is less relevant than Fe^{2+} sorption by surface complexation. Model results of the medium-size cells show that magnetite precipitates in the Fe powder. The experimental observations indicate that there is no magnetite penetration in the bentonite. Some magnetite precipitation was observed at the interface, which is consistent with the small amount of magnetite

precipitation computed at the interface. The precipitation of magnetite at chemical equilibrium is larger than that computed with a kinetically-controlled precipitation. $Fe(OH)_2(s)$ does not precipitate when magnetite precipitates at equilibrium and when the corrosion rate is decreased.

A coupled THCM model of the bentonite and the concrete test in the HB4 cell has been performed. The model reproduces the measured the temperature, the relative humidity, the water content and the porosity data. However, the model overestimates the relative humidity measured at the sensor near the heater. Model results show that advection is relevant during the first months of the test. Then, solute diffusion is the main transport process. The main mineralogical alterations are predicted to occur at the hydration boundary, the concrete near the bentonite interface, and the bentonite near the concrete interface. Calcite and Mg phases precipitate at the hydration boundary due to the large concentrations of bicarbonate and magnesium in the hydration water. The largest amount of calcite and brucite precipitation take place at the bentonite and concrete near the interface. Sepiolite also precipitates in the concrete near the bentonite interface. The model predicts the dissolution of portlandite in the concrete and CSH1.8 and a small C0.8SH precipitation. Ettringite precipitates in the concrete near the hydration boundary and dissolves in the rest of the concrete. The porosity changes due to mineral precipitation/dissolution, especially at the hydration boundary and in the bentonite and concrete near the interface. The porosity reduces 51% in the concrete at the bentonite interface when brucite precipitate. The pH front (pH > 8.5) diffuses into the bentonite 1 cm at the end of the test. Model results capture the main trends of the mineralogical observations. The model, however, does not reproduce ettringite and CSH precipitation. The predicted precipitation for these phases is smaller than the observed values.

A coupled THCM model of the mortar-bentonite interactions of the double interface tests has been presented. The model reproduce the measured water intake, water content and the dry density at the end of the test. The mode predicts the portlandite dissolution in the mortar and calcite, brucite, CSH1.2 and CSH1.6 precipitation in the mortar and in the bentonite near the interface. Anhydrite precipitates in the mortar, but it is transformed into gypsum after the cooling phase. The model predicts a small precipitation of ettringite and quartz and no cristobalite dissolution. The porosity decreasing is maximum (1.5%) in the bentonite in a 0.2 mm thick zone near the mortar interface due to calcite and brucite precipitation. The pH front (pH>8) penetrates into bentonite 10 mm at the end of the test. For the most part, the numerical model captures the main trends of the observed mineral dissolution/precipitation patterns. However, there are some discrepancies, especially for ettringite precipitation in the mortar which is not computed with the model, and brucite precipitation in the bentonite which was not

observed in the laboratory. Some of these discrepancies could be due to the limitations of the model which does not account for CASH phases because there are no thermodynamic data for such CASH phases. The results of the sensitivity run to the initial composition of the exchange complex show that: 1) Cation exchange reactions in the test containing natural FEBEX bentonite are enhanced compared to the test of pre-treated FEBEX bentonite; 2) The concentrations of dissolved of Mg^{2+} and Na^{+} in the test containing natural FEBEX bentonite are larger than those of the test with pre-treated FEBEX bentonite while the concentrations of dissolved of Ca^{2+} and K^{+} in the test with the natural FEBEX bentonite are smaller than in the test with pre-treated bentonite; and 3) Brucite and gypsum dissolution/precipitation is slightly sensitive to the change in the composition of the exchange complex.

12.4. THCM models the FEBEX *mock-up* and *in situ* tests

The THC model of the FEBEX *mock-up* test was tested with data collected from t = 3,000 days to t = 5,000 days. The computed water intake and the relative humidities at the external sensors reproduce the measured data. However, the computed relative humidity underestimates the measured data at the internal sensors after 1,500 days.

The previous 1-D axisymmetric model of the FEBEX *in situ* test has been extended to 2-D axisymmetric conditions. In general, the 1-D model results fit the temperature and water content measured data better than the 2-D model. A detailed calibration of the parameters of the 2-D axisymmetric model will lead to model results at least as good as or better than the results of the 1-D axisymmetric model. The contour lines of the Cl^{-} concentration are approximately parallel to the axis of the gallery along heaters 1 and 2, but the edge effects extend approximately over a distance of 0.5 to 1 m.

The previous 1-D THCM model of the FEBEX *in situ* test has been updated by improving the boundary conditions, refining the mesh at the heater-bentonite interface and updating the solute dispersivities in the bentonite and granite. These improvements on the THCM 1-D model lead to an increase in the water evaporation near the heater and larger concentrations near the heater.

The updated 1-D axisymmetric model has been used to compare the model results with the thermal and hydraulic data from 2002 to 2015 and to perform the pre-dismantling geochemical predictions at 2015. The numerical results reproduce the main trends of the temperature, relative humidity, water content and dry density. The predicted concentrations in the hot sections show large concentrations near the heater and small concentrations at the

bentonite-granite interface. The predicted concentrations in a hot section in 2015 are smaller than those computed in 2002. The predicted concentrations in a cold section in 2015 show a diffusion front.

Updated predictions of the tracer migration have been performed with the most updated version of the THCM model of the FEBEX *in situ* test. The predictions of tracer migration lead to the following conclusions:

- Large iodide concentrations are predicted near the heater 2. The iodide concentration in section 37 near the heater 1 decreased after the heater was switched off in 2002 due to the increase in water content caused by vapor condensation and bentonite hydration.
- The predicted perrhenate concentrations in 2015 show that this tracer has diffused entirely in the full section.
- The plume of borate in the inner blocks is almost circular with a diameter of 8 cm, the plume of selenite is semicircular with an approximate diameter of 20 cm and the plume of europium is anisotropic with an approximate length of 8 cm.
- The plume of cesium in the outer blocks is almost circular with an approximate diameter of 7 cm and is almost circular with a diameter of 10 cm for borate.

A detailed 1-D non-isothermal variably-saturated water flow and multicomponent reactive transport model normal to the bentonite-concrete interface has been performed to study the geochemical interactions of the bentonite and the concrete plug. Model predictions show that calcite dissolves in the bentonite and precipitates near the bentonite-concrete interface. The precipitation front propagates into the bentonite. Portlandite dissolves in the concrete interface. Ettringite precipitation is very small and nonuniform. Neither gypsum nor anhydrite precipitate. CSH1.8 dissolves in the concrete near the concrete-bentonite interface while CSH0.8 precipitation in the concrete is extremely small. Brucite precipitates in the bentonite near the interface. The front of brucite precipitation moves from the bentonite-concrete interface into the bentonite. Sepiolite shows a similar precipitation front. The porosity decreases slightly in the bentonite near the concrete-bentonite interface due to the precipitation of brucite, calcite and sepiolite. The porosity in the concrete, on the other hand, increases near the interface due mostly to the dissolution of portlandite. The changes in porosity only affect 2 cm in the bentonite and concrete interface in both sides of the interface. The pH increases slightly in the concrete. The high pH front penetrates a few cm into the bentonite after 13 years.

12.5. Long-term reactive transport models of the geochemical interactions of the compacted bentonite with concrete and corrosion products in HLW repositories

Reactive transport models of the interactions of the bentonite with other components of the engineered and geological barriers have been performed for HLW repositories in granite and clay.

12.5.1. Reactive transport modelling of the long-term interactions of corrosion products and compacted bentonite in a HLW repository in granite

Canister corrosion causes an increase in the pH and the concentration of dissolved Fe^{2+} of the bentonite pore water. The largest pH in the bentonite is almost 9.5 at $2 \cdot 10^5$ years. Magnetite is the main corrosion product and its precipitation reduces significantly the porosity of the bentonite barrier near the canister and could even clog the pores. The thickness of the bentonite affected by the decrease of porosity increases with time and is equal to 7 cm at t = 1 Ma. This thickness is doubled when the dependence of the corrosion rate on the chemical conditions is considered and reduces 3 cm when smectite dissolution and analcime precipitation are taken into account. Model results are not sensitive to the thermal transient and the effect of temperature on the corrosion rate. The conclusions of the simulations are consistent for the most part with those reported by others for bentonite barriers. However, there are differences in the geochemical systems and the hypotheses used by Savage et al. (2010a).

12.5.2. Long-term non-isothermal reactive transport model of compacted bentonite, concrete and corrosion products in a HLW repository in clay

Canister corrosion and concrete degradation cause an increase in the pH. The largest pH in the bentonite is 9.4 at 10^6 years. Magnetite is the main corrosion product and its precipitation reduces significantly the porosity of the bentonite barrier near the canister and could even clog the pores. In addition, the concrete degradation in the repository in clay leads to the precipitation of secondary minerals and the reduction of the porosity of the bentonite and the clay formation at their interfaces with the concrete liner. The decrease of the porosity is especially important for $t > 10^4$ years. The thickness of the zones affected by pore clogging at the canister-bentonite, and concrete-clay interfaces at 1Ma are equal to 1, and 3.3 cm, respectively. The results show similarities with the results of the models reported by others for engineered barrier systems at similar chemical conditions, including: 1) Pore clogging at the

canister-bentonite and concrete-clay interfaces; 2) Narrow alteration zones; and 3) Limited smectite dissolution after 1 Ma.

12.6. Recommendation for future work

Future studies to improve the integrated analysis include:

- Extending the Green-Ampt solution to account for water distribution.
- Developing analytical solutions for temperature and concentration.
- Performing the integrated analysis of chemical data for reactive species.

The THCM models of the laboratory tests could be improved by:

- Calibrating the THCM model with hydrochemical data. This will require the numerical inverse analysis of the aqueous extract data.
- Taking into account the CO_2(g) degassing The implementation in INVERSE-FADES-CORE V2 of the gas reactive transport equation could be tested with the THCM model of the CG tests.
- Performing a detailed analysis of the discretization errors by refining the finite element mesh in areas with large concentration gradients to reduce the mass balance errors.
- Evaluating the sensitivity of the model results to kinetic parameters.
- Improving the THCM model of the interactions of mortar and bentonite by account for Cl^- sorption in the mortar.

The THCM models of the FEBEX *in situ* test could be improved by:

- Calibrating the model parameters and boundary conditions of 2-D axisymmetric model such as the thermal conductivity, the hydraulic conductivity, the retention curve, the vapor tortuosity and the longitudinal dispersivity of the bentonite and the thermal and hydraulic boundary conditions in the granitic rock.
- Accounting for the inner-block solute diffusion during the time elapsed since block extraction and water sampling for chemical analyses.
- Modelling Cs sorption with a reactive transport model.
- Testing the model results of the interactions of bentonite and the concrete plug with the measured data which have been published just after completing this dissertation (Alonso et al., 2017 and Fernández et al, 2017).

Model predictions of the long-term geochemical evolution of the bentonite barrier could be improved by:

- Considering adsorbed, interlayer and free water.
- Allowing for different effective diffusion coefficients for each chemical species.
- Allowing for the canister void space to have properties other than those of the bentonite and simulating canister corrosion in a more realistic manner by adopting a dynamic corrosion front.
- Taking into account kinetic magnetite precipitation.
- Accounting for other secondary minerals such as Fe-phylosilicates, Fe-rich smectites and zeolites.
- Accounting for the feedback on porosity and other transport and chemical parameters caused by mineral dissolution/precipitation and allowing for the dynamic update of the reactive surface areas of the minerals.

Chapter 13. References

Alonso, M.C., García, J. L., Cuevas, J., Turrero, M.J., Fernández, R., Torres, E., Ruiz, A.I., 2017. Interaction processes at the concrete-bentonite interface after 13 years of FEBEX-Plug operation. Part I: Concrete alteration, Physics and Chemistry of the Earth, Parts A/B/C (In Press)

Bauer, A. and Berger, G., 1998. Kaolinite and smectite dissolution rate in high molar KOH solutions at 35° and 80 °C. Appl. Geochem. 13, 905–916.

Berner, U., Kulik, D. A. and Kosakowski, G., 2013. Geochemical impact of a low-pH cement liner on the near field of a repository for spent fuel and high-level radioactive waste. Physics and Chemistry of the Earth 64, 46-56.

Bildstein, O., Trotignon, L., Perronnet, M. and Jullien, M., 2006. Modelling iron-clay interactions in deep geological disposal. Phys. Chem. Earth 31, 618–625.

Bradbury, M.H. and Baeyens, B., 1997. A mechanistic description of Ni and Zn sorption on Na-montmorillonite. Part II: modelling. J. Contam. Hydrol. 27, 223–248.

Buil, B, Gómez, P., Peña J., Garralón, A., Turrero, M.J., Escribano, A., Sánchez, L. and Durán, J.M., 2010, Modelling of bentonite–granite solutes transfer from an in situ full-scale experiment to simulate a deep geological repository (Grimsel Test Site, Switzerland), Applied Geochemistry 25:1797–1804.

Cox, B.L. Pruess, K., 1990. Numerical experiments on convective heat transfer in water-satured porous media at near-critical conditions. Transport in porous media, 5, 299-323.

Cuevas, J., Villar M., Fernández, A., Gómez, P. and Martín, P., 1997. Pore waters extracted from compacted bentonite subjected to simultaneous heating and hydration. Applied Geochemistry, 12, 473–481.

Cuevas, J., Turrero, M.J., Torres, E., Fernández, R., Ruiz, A.I. and Escribano, A., 2013. Deliverable D2.3-3-2 of PEBS Project. Laboratory tests at the interfaces. Results of Small Cells with mortar-bentonite-magnetite. CIEMAT.

Cuevas, J., Ruíz, A.I., Fernández, R., Torres, E., Escribano, A., Regadío, M., Turrero, M. J., 2016. Lime mortar-compacted bentonite-magnetite interfaces: An experimental study focused on the understanding of the EBS long-term performance for high-level nuclear waste isolation DGR concept. Applied Clay Science 124-125, 79-93.

Dai, Z. and Samper, J., 2004. Inverse problem of multicomponent reactive chemical transport in porous media: formulation and applications. Water Resour Res 40, W07407.

De Windt, L., Pellegrini, D. and Van der Lee, J., 2004. Coupled modeling of cement/claystone interactions and radionuclide migration. J. Contam. Hydrol. 68, 165-182.

De Windt, L. and Torres, E., 2009. Modélisation d'expériences en cellule reproduisant les conditions THC d'une alvéole de déchets HAVL. Rapport Technique R201009LDEWI. Accord spécifique IRSN/ARMINES.

De Vries, D.A., 1963. Thermal properties of soils. In: Van Wijk, W.R. (Ed.), Physics of Plant Environment. North-Holland Publishing Company, Amsterdam, pp. 210–235.

ENRESA, 2000. FEBEX Project. Full-scale engineered barriers experiment for a deep geological repository for high level radioactive waste in crystalline host rock. Final Report. Publicación Técnica ENRESA 1/2000, Madrid, 354 pp.

ENRESA, 2004. Evaluación del comportamiento y de la seguridad de un almacén geológico profundo de residuos radiactivos en arcilla. PT 49-1PP-M-A1-01.

ENRESA, 2005, Phenomenological description. Reference Concept (Spent Fuel-Carbon Steel Canister-Bentonite-Granite). NF-PRO Integrated Project. Deliverable D5.1.1. Part 1. Final version.

ENRESA, 2006a. Full-Scale Engineered Barriers Experiment: Updated Final Report. ENRESA Tech. Publ. PT 05-02/2006, 589 pp.

ENRESA, 2006b. FEBEX: Final report on thermo-hydro-mechanical modelling. ENRESA Techn. Publ. PT 05-2/2006, 163 pp.

ENRESA, 2006c. FEBEX: Final THG modelling report. ENRESA Technical Publication. PT 05-3/2006, 155 pp.

Fernández, A.M., Cuevas, J., Rivas, P. and Martín, P.L., 1999. THG tests in termohydraulic cells. Technical Report 70-IMA-L-0-41, CIEMAT, Madrid.

Fernández, A., Cuevas, J. and Mäder, U.K., 2009a. Modelling concrete interaction with a bentonite barrier. Eur. J. Mineral 21, 177-191.

Fernández, R., Mäder, U.K., Rodriguez, M., Vigil de la Villa, R. and Cuevas, J., 2009b. Alteration of compacted bentonite by diffusion of highly alkaline solutions. European Journal of Mineralogy 21, 725–735.

Fernández A. M. and Villar M.V., 2010. Geochemical behavior of bentonite barrier in the laboratory after up to 8 years of heating and hydrating. *Applied Geochemistry,* 25, 809-824

Fernández, R., Torres, E., Ruiz, A. I., Cuevas, J., Alonso, M. C., García, J. L., Rodríguez, E., Turrero, M. J., 2017. Interaction processes at the concrete-bentonite interface after 13 years of FEBEX-Plug operation. Part II: Bentonite contact. Physics and Chemistry of the Earth, Parts A/B/C (In Press)

Fredlund, D.G. and Rahardjo, H., 1993. Soil Mechanics for Unsaturated Soils.Wiley-IEEE. 517 pp.

Fritz, B. and Madé, B., 1991. Geochemical modelling of bentonite-alkaline solutions interactions in the near-field of a repository for spent nuclear fuel. SKB Technical Report 91-05. Swedish Nuclear Fuel and Waste Management Company, Stockholm, Sweden.

Gaucher, E. C. and Blanc P., 2006. Cement/clay interactions – A review: Experiments, natural analogues, and modeling. Waste Management Volume 26, Issue 7, 776–788.

Gens, A., Sánchez, M., Guimarães, L., Alonso, E. E., Lloret, A., Olivella, S., Villar, M. V. and Huertas F., 2009. A full-scale in situ heating test for high-level nuclear waste disposal: observations, analysis and interpretation. Géotechnique, 59(4): 377-399.

Guimarães, L.D., Gens, A. and Olivella, S., 2007. Coupled thermo-hydro-mechanical and chemical analysis of expansive clay subjected to heating and hydration. Transp. Porous Med. 66 (3), 341–372.

Juncosa, R., 2001. Modelos de flujo multifásico no isotermo y de transporte reactivo multicomponente en medios porosos. ENRESA, Publicación Técnica, Ph. D Dissertation, Universidad Politécnica de Madrid. 287 pp.

Huertas, F., Farias, J., Griffault, L., Leguey, S., Cuevas, J., Ramírez, S., Vigil de la Villa, R., Cobeña, J., Andrade, C., Alonso, M.C., Hidalgo, A., Parneix, J.C., Rassineux, F., Bouchet, A., Meunier, A., Decarreau A., Petit, S., Vieillard P., 2000. Effects of cement on clay barrier performance: (Ecoclay Project).

Johnson, L., Gaus, I., Wieczorek, K., Mayor, J.-C., Sellin, P., Villar, M.V., Samper, J., Cuevas, J.A., Gens, M., Velasco, M., Turrero, M.J., Montenegro, L., Martin, P.L. and Armand, G., 2014. Integration of the Short-term Evolution of the Engineered Barrier System (EBS) with the Long-term Safety Perspective. PEBS Deliverable D4.1.

Keijzer, T.J.S., Kleingeld, P.J. and Loch, J.P.G., 1999. Chemical osmosis in compacted clayey material and the prediction of water transport. Eng. Geol. 53, 151–159.

Keijzer, T.J.S. and Loch, J.P.G., 2001. Chemical osmosis in compacted dredging sludge. Soil Sci. Soc. Am. J. 65, 1045–1055.

Kolditz, O., Bauer, S., Bike, L., Böttcher, N., Delfs, J. O., Fischer, T., Görke, U. J., Kalache, T., Kosakowski, G., McDermott, C. I., Park, C. H., Radu, F., Rink, K., Shao, H., Shao, H. B., Sun, F., Sun, Y. Y., Singh, A. K., Taron, J., Walther, M., Wang, W., Watanabe, N., Wu, Y., Xie, M., Xu, W. and Zehner, B., 2012. OpenGeoSys: an open-source initiative for numerical simulation of thermo-hydro-mechanical/chemical (THM/C) processes in porous media. Environ Earth Science 67:589–599.

Kosakowski, G. and Berner, U., 2013. The evolution of clay rock/cement interfaces in a cementitious repository for low- and intermediate level radioactive waste. Physics and Chemistry of the Earth 64, 65-86.

Lalan, P., Dauzères, A., De Windt, L., Bartier, D., Sammaljärvi, J., Barnichon, J.D., Techer, I., Detilleux, V., 2016. Impact of a 70 °C temperature on an ordinary Portland cement paste/claystone interface: An in situ experiment. Cement and Concrete Research 83, 164-178.

Lehikoinen, J., 2009. Bentonite-cement interaction -– Preliminary results from model calculations. Posiva Working Report WR 2009-37. Posiva Oy, Olkiluoto, Finland.

Lichtner, P.C., 1996. Continuum formulation of multicomponent–multiphase reactive transport. In: Lichtner, P.C., Steefel, C.I., Oelkers, E.H. (Eds.), Reviews in Mineralogy. Reactive Transport in Porous Media. Mineralogical Society of America, Washington, DC.

Lloret, A. and Alonso, E.E., 1995. State surfaces for partially saturated soils. In: Proceedings of the International Conference on Soils Mechanics and Foundation Engineering, Balkema, pp. 557–562.

Lothenbach, B., Bernard and E., Mäder, U., 2017. Zeolite formation in the presence of cement hydrates and albite. Physics and Chemistry of the Earth.

Lu, C., Samper, J., Fritz, B., Clement, A. and Montenegro, L., 2011. Interactions of corrosion products and bentonite: An extended multicomponent reactive transport model. Physics and Chemistry of the Earth 36, 1661–1668, doi: 10.1016/j.pce.2011.07.013.

Martín, P.L., Barcala, J.M., 2005. Large scale buffer material test: mock-up experiment at CIEMAT. Eng. Geol. 81, 298–316.

Martín, P.L., Barcala, J.M., and Huertas, F., 2006. Large-scale and long-term coupled thermo-hydro-mechanic experiements with bentonite: the FEBEX mock up test. J. Iberian Geol. 32 (2), 259-282.

Marty, N.C.M., Tournassat, C., Burnol, A., Giffaut, E. and Gaucher, E. C., 2009. Influence of reaction kinetics and mesh refinement on the numerical modelling of concrete/clay interactions. Journal of Hydrology 364, 58-72.

Marty, N.C.M, Fritz, B., Clément, A. and Michau, N., 2010a. Modelling the long term alteration of the engineered bentonite barrier in an underground radioactive waste repository. Applied Clay Science 47, 82-90.

Marty, N., Claret, F., Gaboreau, S., Cochepin, B., Munier, I., Michau, N., Gaucher, E. C. and Burnol, A., 2010b. Dual alteration of bentonite by iron corrosion and concrete interaction under high temperature conditions. In Clays in Natural and Engineered Barriers for Radioactive Waste Confinement, Nantes, France, pp. 473–474.

Melkior, T., Mourzagh, D., Yahiaoui, S., Thoby, D., Alberto, J.C., Brouard, C., Michau, N., 2004. Diffusion of an alkaline fluid through clayey barriers and its effect on the diffusion properties of some chemical species. Applied Clay Science, Volume 26, 99–107.

Mon, A., Samper, J., Montenegro, L., Naves, A., Fernández, J., 2017. Reactive transport model of compacted bentonite, concrete and corrosion products in a HLW repository in clay. Journal of Contaminant Hydrology 197, 1-16.

Montes-H, G., Marty, N., Fritz, B., Clement, A. and Michau, N., 2005. Modelling of long-term diffusion-reaction in a bentonite barrier for radioactive waste confinement. Appl. Clay Sci. 30, 181–198.

Navarro, V., 1997. Modelo de comportamiento mecánico e hidráulico de suelos nosaturados en condiciones no isotermas. Ph.D. Dissertation, Universidad Politécnica de Cataluña, 329 pp.

Navarro, V. and Alonso, E.E., 2000. Modelling swelling soils for disposal barriers. Compt. Geotech. 27,19-43.

Ngo, V. V., Delalande, M., Clément A., Michau, N. and Fritz, B., 2014. Coupled transport reaction modelling of the long-term interaction between iron, bentonite and Callovo-Oxfordian claystone in radioactive waste confinement systems. Applied Clay Science, 101, 430-443.

Nguyen, T.S., Selvadurai, A.P.S. and Armand, G., 2005. Modelling the FEBEX THM experiment using a state surface approach. Int. J. Rock Mech. Min. Sci. 42 (5–6), 639–651.

Olivella, S., Gens, A., Carrera, J. and Alonso, E.E., 1996. Numerical formulation for a simulator (CODE_BRIGHT) for the coupled analysis of saline media. Eng. Comput. 13 (7), 87–112.

Parkhust, D. L., and Appelo, C. A. J., 1999. User's guide to PHREEQC (version 2) – a computer program for speciation, batch-reaction, one-dimensional transport, and inverse geochemical calculations. US, Geol. Surv. Water-Resour. Invest. Rep., 99-4259.

Pollock, D.W., 1986. Simulation of fluid flow and energy transport processes associated with high-level radioactive waste disposal in unsaturated alluvium. Water Resour. Res. 22 (5), 765–775.

Saaltink, M.W., Batlle, F., Ayora, C., Carrera, J. and Olivella, S., 2004. RETRASO, a code for modelling reactive transport in saturated and unsaturated porous media. Geol. Acta 2 (3), 235–251.

Samper, J., Yang, C. and Montenegro, L., 2003. CORE2D version 4: a code for non-isothermal water flow and reactive solute transport. User's Manual. University of La Coruña, Spain.

Samper, J., Lu, C. and Montenegro, L., 2008. Coupled hydrogeochemical calculations of the interactions of corrosion products and bentonite. Physics and Chemistry of the Earth 33, S306–S316, doi:10.1016/j.pce.2008.10.009.

Samper, J., Naves, A., Montenegro, L. and Mon., A., 2016. Reactive transport modelling of the long-term interactions of corrosion products and compacted bentonite in a HLW repository in granite: Uncertainties and relevance for performance assessment, Applied Geochemistry. Vol 67, 42-51.

Savage, D., Bateman, K., Hill, P., Hughes, C., Milodowski, A., Pearce, J., Rae, E. and Rochelle, C., 1992. Rate and mechanism of the reaction of silicates with cement pore fluids. Appl. Clay Sci. 7, 33-45.

Savage, D., Noy, D. J. and Mihara, M., 2002. Modelling the interaction of bentonite with hyperalkaline fluids. Applied Geochemistry 17, 207-223.

Savage, D., Watson, C., Benbow, S. and Wilson, J., 2010a. Modelling iron/bentonite interactions. Applied Clay Science 47, 91-98.

Savage, D., Benbow, S., Watson, C., Takase, H., Ono, K., Oda, C. and Honda, A., 2010b. Natural systems evidence for the alteration of clay under alkaline conditions: an example from Searles Lake, California. Applied Clay Science 47, 72–81.

Savage, D., Arthur, R., Watson, C. and Wilson, J., 2010c. An evaluation of models of bentonite pore water evolution. SSM Technical Report 2010:12. Swedish Radiation Safety Authority, Stockholm, Sweden.

Savage, D., 2011. A review of analogues of alkaline alteration with regard to long-term barrier performance. Mineral. Mag. 75, 2401–2418.

Savage, D., Soler, J.M., Yamaguchi, K., Walker, C., Honda, A., Inagaki, M., Watson, C., Wilson, J., Benbow, S., Gaus, I. and Rueedi, J., 2011. A comparative study of the modelling of cement hydration and cement-rock laboratory experiments. Applied Geochemistry 26, 11381152.

Savage, D., 2012. Prospects for coupled modelling. STUK-TR 13. Radiation and Nuclear Safety Authority.

Shao, H., Kosakowski, G., Berner, U., Kulik, D.A., Mäder, U. and Kolditz, O., 2013. Reactive transport modeling of the clogging process at Maqarin natural analogue site. Physics and Chemistry of the Earth 64, 21-31.

Soler, J.M., 2001. The effect of coupled transport phenomena in the Opalinus clay and implications for radionuclide transport. J. Contam. Hydrol. 53, 63–84.

Soler, J.M., Paris, B., Pfingsten, W. and Mäder, U., 2004. Flow and reactive transport modeling in the framework of GTS-HPF. Water–Rock Interaction XI. Balkema, Rotterdam, The Netherlands, pp. 983–987.

Steefel, C.I., 2001. GIMRT, Version 1.2: software for modelling multicomponent, multidimensional reactive transport. Users guide. Technical report UCRL-MA-143182, Lawrence Livermore National Laboratory, Livermore, California.

Steefel, C.I. and Lichtner, P.C., 1998. Multicomponent reactive transport in discrete fractures II. Infiltration of hyperalkaline groundwater at Maqarin, Jordan, a natural analogue site. J. Hydrol. 209, 200-224.

Tang, A.M., Cui, Y.J. and Le, T.T., 2008. A study on the thermal conductivity of compacted bentonites. Appl. Clay Sci. 41 (3–4), 181–189.

Tinseau, E., Bartier, D., Hassouta, L., Devol-Brown, I. and Stammose, D., 2006. Mineralogical characterization of the Tournemire argillite after in situ reaction with concretes. Waste Manag. 26, 789-800.

Torres, E., Turrero, M. J., Peña, J., Martín, P.L., Escribano, A., Alonso, U., Villar, M.V., 2008. Deliverable 2.3.2 of component 2 NF-PRO project. Interaction iron-compacted bentonite: corrosion products and changes in the properties of the bentonite, CIEMAT.

Torres, E., Turrero, M.J. and Escribano, A., 2013. Synthesis of corrosion phenomena at the iron/bentonite interface under unsaturated condictions. Technical Note CIEMAT/DMA/2G210/02/2013. PEBS Project.

Turrero, M. J., Villar, M. V., Torres, E., Escribano, A., Cuevas, J., Fernández, R., Ruiz, A. I., Vigil de la Villa, R., del Soto, I., 2011. Deliverable 2.3-3-1 of PEBS Project. Laboratory tests at the interfaces, Final results of the dismantling of the tests FB3 and HB4, 2011. CIEMAT.

Ueda, H., Hyodo, H., Takase, H., Savage, D., Benbow, S. and Noda, M., 2007. Evaluation of the kinetics of cement-bentonite interaction in a HLW repository using the reactive solute transport simulator. In 15th International Conference on Nuclear Engineering, Nagoya, Japan, pp. ICONE15-10566.

Villar, M.V, Fernández, A.M., Martín, P.L., Barcala, J.M., Gómez-Espina, R. and Rivas, P., 2008a. Effect of heating/hydration on compacted bentonite: test in 60 cm long cells. Colección Documentos CIEMAT.

Villar, M.V., Sánchez, M., Gens, A., 2008b. Behaviour of a bentonite barrier in the laboratory: experimental results up to 8 years and numerical simulation. Physics and Chemistry of the Earth, Vol. 33, Supplement 1, pp. S476-S485.

Villar M.V., Martín P. L., Bárcena I., García-Sinériz J. L., Gómes-Espina R. and Lloret A., 2012. Long-term experimental evidences of saturation of bentonite under repository conditions. *Engineering Geology,* 149-150, 57-69.

Watson, C., Benbow, S. and Savage, D., 2007. Modelling the interaction of low pH cements and bentonite. Issues affecting the geochemical evolution of repositories for radioactive waste. SKI Report 2007:30. Swedish Nuclear Power Inspectorate, Stockholm, Sweden.

Watson, C., Hane, K., Savage, D., Benbow, S., Cuevas, J. and Fernández, R., 2009a. Reaction and diffusion of cementitious water in bentonite: results of 'blind' modelling. Applied Clay Science 45, 54–69.

Watson, C., Hane, K., Savage, D., Benbow, S., Cuevas, J., Fernández, R., Norris and S., Amme, M., 2009b. Modelling diffusion and reaction of cementitious water in bentonite. In The Scientific Basis for Nuclear Waste Management XXXIII, 413–420. Burakov and A.S. Aloy, Eds.

Watson, C., Savage, D., Wilson, J., Benbow, S., Walker, C. and Norris, S., 2013. The Tournemire industrial analogue: reactive transport modelling of a cement-clay interface. Clay Minerals 48, 167-184.

Watson, C., Wilson, J., Savage, D., Benbow, S. and Norris, S., 2016. Modelling reactions between alkaline fluids and fractured rock: The Maqarin natural analogue. Applied Clay Science 121-122, 46–56.

Wersin, P., Birgersson, M., Olsson, S., Karnland, O. and Snellman, M., 2007. Impact of corrosion-derived iron on the bentonite buffer within the KBS-3H disposal concept – The Olkiluoto site as case study. Posiva Report 2007/11. Posiva Oy, Olkiluoto, Finland.

Wollery, T.J., 1992. EQ3/3. A software package for geochemical modeling of aqueous system: package overview and installation guide version 7.0. UCRL-MA-110662-PT-I, Lawrence Livermore National Laboratory, Livermore, California.

Xu, T., Samper, J., Ayora, C., Manzano and M., Custodio, E., 1999. Modeling of non-isothermal multi-component reactive transport in field scale porous media flow systems. J. Hydrol. 214 (1–4), 144–164.

Xu, T. and Pruess, K., 2001. Modeling multiphase non-isothermal fluid flow and reactive geochemical transport in variably saturated fractured rocks: 1. Methodology. Am. J. Sci. 301, 16–33.

Xu, T., Senger, R. and Finsterle, S., 2008. Corrosion-induced gas generation in a nuclear waste repository: Reactive geochemistry and multiphase flow effects Applied Geochemistry 23 3423–3433.

Yamaguchi, T., Sakamoto, Y., Akai, M., Takazawa, M., Iida, Y., Tanaka, T. and Nakayama, S., 2007. Experimental and modeling study on long-term alteration of compacted bentonite with alkaline groundwater. Physics and Chemistry of the Earth 32, 298-310.

Yang, C., Samper, J. and Montenegro, L., 2008. A coupled non-isothermal reactive trans-port model for long-term geochemical evolution of a HLW repository in clay. Environmental Geology 53, 1627–1638, doi: 10.1007/s00254-007-0770-2.

Yu-Shu, W. and Pruess, K., 1999. Integral solution for transient fluid flow through a porous medium pressure-dependent permeability. International Journal of Rock Mechanics and Mining Sciences, 37, 51-61.

Yu-Shu, W., Liu, H.H. and Bodvarsson, G.S., 2004. A triple-continuum approach for modeling flow and transport process in fractured rocks. Journal of Contaminant Hydrology, 73, 145-179.

Zheng, L. and Samper, J., 2004. Formulation of the inverse problem of non-isothermal multiphase flow and reactive transport in porous media. Comput. Meth. Water Resour. XV, 1317–1327.

Zheng, L. and Samper, J., 2005. A dual continuum coupled multiphase flow model with mixed second order water transfer term for structured soils. Jornadas de la Zona no Saturada 2005, VII, 301-306.

Zheng, 2006. Coupled thermo-hydro-mechanical-geochemical models for structurated deformable porous media. Ph.D. Dissertation, Universidade de A Coruña.

Zheng, L. and Samper, J., 2008. Coupled THMC model of FEBEX mock-up test. Physics and Chemistry of the Earth 33, S486–S498, doi:10.1016/j.pce.2008.10.023.

Zheng, L., Samper, J., Montenegro, L. and Mayor, J.C., 2008. Flow and reactive transport model of a ventilation experiment in Opallinus clay, Physics and Chemistry of the Earth, Vol. 33, S486–S498. doi:10.1016/j.pce.2008.05.012.

Zheng, L., Samper, J., Montenegro, L. and Fernández, A.M., 2010. A coupled THMC model of a heating and hydration laboratory experiment in unsaturated compacted FEBEX bentonite. Journal of Hydrology 386, 80-94, doi: 10.1016/j.jhydrol.2010.03.009.

Zheng, L., Samper, J. and Montenegro, L., 2011. A coupled THC model of the FEBEX in situ test with bentonite swelling and chemical and thermal osmosis. Journal of Contaminant Hydrology 126, 45-60.